UNIVERSITY OF CALIFORNIA
RIVERSIDE

Remote-Activated Electrical Stimulation via Piezoelectric Scaffold System for Functional Nerve Regeneration

A Dissertation submitted in partial satisfaction
of the requirements of for the degree of

Doctor of Philosophy

in

Bioengineering

by

Karen Gail Low

December 2017

Dissertation Committee:
Dr. Jin Nam, Chairperson
Dr. Hyle B. Park
Dr. Nosang V. Myung

The Dissertation of Karen Gail Low is approved:

_____

_____

_____

Committee Chairperson

University of California, Riverside

ACKNOWLEDGEMENTS

First and foremost, I would like to express my deepest appreciation to my PhD advisor and mentor, Dr. Jin Nam. I came from a background with no research experience, therefore his guidance, motivation, and ambition for me to succeed helped developed me into the researcher I am today. And most of all, I am forever grateful for his patience with all my blood, sweat and tears that went into this 5 years. He once said, “it takes pressure to make a diamond.” His words of wisdom will continue to guide me through my career. I would also like to thank my collaborator, Dr. Nosang V. Myung. He gave me the opportunity to explore a field that was completely outside of my comfort zone of biology. His advice and constructive criticism will resonant with me to my future career. Additionally, I would like to thank my collaborator, Dr. B. Hyle Park. His expansive knowledge on neuroscience helped build the foundation of this doctoral work.

Next, I would like to thank my lab colleagues Dr. Maricela Maldonado, Dr. Christopher Horner, and Dr. Gerardo Ico. They put up with all my nonsense and kept me grounded during these past 5 years. Additionally, I would like to thank my undergraduate students who contributed vastly to my research, Daniel Nitinthorn and especially David Garcia-Viramontes. They worked tirelessly with me to insure the completion of my projects. I am forever thankful to my graduate and undergraduate students who made this journey possible. I would like to express gratitude to all the Bioengineering faculty, staff, and colleagues for their support.

Appendix A has been previously published in Nanotechnology. Appendix B has been previously published in Sensors and Actuators. Appendix C has been previously published in Stem Cell Reports.

DEDICATION

This dissertation is dedicated to my parents, Leslie and Phronis Low, and my brother, Logan Low. Throughout the 5 years, they always showed their support and unconditional love through all the good and difficult times. They were always understanding when I wasn't present for many events because I was so far, but they showed their appreciation and care no matter what. I would also like to thank the Rugge family for their support. They were my family away from home and kept me sane during these times.

ABSTRACT OF THE DISSERTATION

Remote-Activated Electrical Stimulation via Piezoelectric Scaffold System for Functional Nerve Regeneration

by

Karen Gail Low

Doctor of Philosophy, Graduate Program in Bioengineering
University of California, Riverside, December 2017
Dr. Jin Nam, Chairperson

A lack of therapeutic technologies that enable electrically stimulating nervous tissues in a facile and clinically relevant manner has partly hindered the advancement in treating nerve injuries for full functional recovery. Currently, the gold standard for nerve repair is autologous nerve grafting. However, this method has several disadvantages, such as necessity for multiple surgeries, creation of functionally impaired region where graft was taken from, disproportion of graft to nerve tissue in size and structure, and most substantially, high risk of neuroma formation. Therefore, there is an increasing need for the development of alternative strategies to enhance nerve regeneration. To address these limitations, the development of a piezoelectric neuroconduit that can self-generate optimized levels of electrical stimulation can be utilized to wrap a damaged nerve and remotely activated by acoustically-driven piezoelectricity. Unlike biochemical-embedded conduit in which the release of neurotrophic factors is limited by loading or electro-conductive conduit in which only passive electrical stimulation by autologous cells is possible without intrusive electrodes, the piezoelectric conduit provides unlimited

opportunity to properly stimulate the neuronal cells *in vivo*. In this regard, a piezoelectric scaffold was developed using electrospinning technology and its piezoelectric performance was optimized by controlling the fiber diameter and scaffold thickness. Various types of neural cells including PC12 cells, Schwann cells, and neural stem cells (NSCs), were subjected to mechanical/electrical stimulation to examine their behavioral changes. When PC12 cells, a model system for neurons, were subjected to multi-day application of mechanical/electrical stimulation, enhancements in neurite formation and elongation were observed. Alternatively, mechanical/electrical stimulation induced Schwan cells, the glial cell of the peripheral nervous system, to differentiate into its myelinating phenotype and induced the enhanced production of the neurotrophic protein, nerve growth factor. Aside from enhancing the functionality of neuronal and glial cells, mechanical/electrical stimulation also induced the differentiation of NSCs towards the functional cell types of the central nervous system, neurons, oligodendrocytes, and astrocytes. Therefore, this project develops a novel method for enhancing nerve regeneration by modulating neuron and glial cell functionality for the repair of nerve injuries.

Table of Contents

List of Figures

Chapter 1. Introduction and background

Chapter 2. Development of a piezoelectric cell culture system for neuroengineering studies

Chapter 4. Mechanical/electrical stimulation enhances glial cell functionality

Appendix A. Polyaniline/poly(ε-caprolactone) composite electrospun nanofiber-based gas sensors: optimization of sensing properties by dopants and doping concentration

Appendix B. Composition-dependent sensing mechanism of electrospun conductive polymer composite nanofibers

List of Tables

CHAPTER 1. INTRODUCTION AND BACKGROUND

Abstract

Severe injuries to the peripheral and central nervous system present a significant clinical problem with limited or lack of treatment for fully functional recovery. When the nerve is damaged by injuries/diseases, such as peripheral nerve transection, spinal cord injury, and diabetic neuropathy, a cascade of cellular events occur to the affected cells and neighboring cells, extracellular matrix of the injury site, and the tissue. Although the peripheral nervous system is more capable of nerve regeneration than the central nervous system, appropriate clinical solutions for nerve damage with large gaps have yet to be found. Recently, various nerve tissue engineering strategies, such as nerve guidance conduits, hydrogels, cell-based therapies, and electrical stimulation, have been explored to enhance nerve regeneration by promoting a permissive environment or inhibiting factors that prevent regrowth from occurring.

1.1 Anatomy of a nerve

The nervous system is composed of the central and peripheral nervous systems. The central nervous system (CNS) consists of the brain and spinal cord, and is responsible for integrating information and coordinating activity from the entire body. In contrast, the peripheral nervous system (PNS) refers to the nerves outside of the CNS, processing bio-directional electrical signals of the motor and sensory neurons. There are two types of neural cells found in both nervous systems: neurons and glial cells. Neurons transmit information to other nerve cells, muscles, or gland cells. Most neurons possess long axons that extend from the cell body that are either myelinated or unmyelinated.

Glial cells are axillary cells that are responsible for maintaining the function of nerves. Schwann cells in the PNS and oligodendrocytes in the CNS are the glial cells that encapsulate the axon with myelin and provide neurotrophic factors. Myelin increases conduction velocity of the electrical signal along the axon by limiting ionic transfer to the nodes of Ranvier, resulting a faster action potential propagation. Astrocytes, another glial cell of the CNS, anchor neurons to their blood supply to help regulate its surroundings by removing excess ions and neurotransmitters. In addition to these cells immediately neighboring the axon, many layers of connective tissue surround the axon. The layer closest to the myelinated axon is the endoneurium, which helps contains the nutrient fluid. The perinerium surrounds bundles of endoneurium-covered axons to form fascicles. Lastly, the epinerium is the outermost connective tissue layer of the nerve. The epifascicular epinerium fills in the spaces between the fascicles, while the epineural

epinerium completely surrounds the nerve trunk. Blood vessels are dispersed throughout the nerve to provide the axons with nutrients. A bundle of axons is called a nerve in the PNS and tract in the CNS (**Figure 1.1**).

1.2. Nerve pathophysiology

Nerve injuries are classified into five categories, ordered by the degree of damage on the overall structure of the nerve (**Table 1**) [1]. The mildest form of injury, Grade I or neuropraxia, is defined as damage to the myelin sheath without any damage to the axons or the connective tissue layers. Grade II through IV, or axonotmesis, involve damage to the myelin sheath as well as the axon itself. The surrounding connective tissue layers remain intact. The grade of injury increases with the amount of damage to the endoneurium, perinerium, and epinerium. The most severe form of nerve injury, Grade V or neurotmesis, is when the nerve is completely transected. The capability of nerve regeneration critically dpends on the degree of nerve damage.

1.2.1. Peripheral nervous system

The PNS has a much greater capacity for nerve self-regeneration than the central nervous system (**Figure 1.3**). When a traumatic injury to the axon of a PNS neuron occurs, either compressed or transected, initially, a retrograde signal is sent to the nucleus by importin, an early injury responsive protein. Importins form a complex with dynein, a cytoskeletal motor protein responsible for driving retrograde axonal transport, on the

axon and sends a cocktail of transcription factors associated with regeneration, such as c-Jun, Oct6, Sox11, and p53, to determine the fate of the injured neuron [2].

When these signaling cascades are initiated, the distal end of the injured axon undergoes molecular changes to create an environment for axon regeneration. The process, known as Wallerian degeneration, that begins in the axon on the distal end of the injured nerve completely degenerates the axon by removing and recycling axonal and myelin-derived components towards the target tissue. Existing Schwann cells clear the axonal and myelin debris, leaving behind an empty endoneurial tube. Macrophages are recruited to the injury site, releasing growth factors to induce the proliferation of Schwann cells and fibroblasts. The proliferating Schwann cells line the inner surface of the empty endoneurial tube, which form the bands of Bungner, to direct the regenerating axon through the distal nerve stump towards the target tissue. On the proximal end of the injury site, the axon degenerates up to the adjacent node of Ranvier, where subsequent axon regrowth begins. These series of events are critical to create a supportive environment for successful axon regeneration.

Once the debris is cleared from the distal nerve stump, a cascade of cellular events occur to regenerate the axon from the adjacent node of Ranvier of the proximal nerve stump into the distal segment. About 50-100 nodal sprouts develop from the node of Ranvier into a growth cone. Neurotrophic factors from the target tissue and denervated motor and sensory receptors signal the growth cone to elongate. From the growth cone, many axon extensions elongate until they connect with a receptor. If a receptor or the

endoneurial tube is not reached, the growth cone continues to elongate in a disorganized manner forming a neuroma. The more severe the injury is, the more disorder occurs, therefore less effective axon regeneration. Therefore, there is a need for tissue engineering strategies to aid in the elongation process by environmental, cellular, and biochemical factors.

1.2.2. Central nervous system

When the brain or spinal cord is injured, complex cellular and molecular interactions occur in attempt to repair the damaged tissue (**Figure 1.4**). Unlike the PNS neurons, CNS neurons have not been shown to possess the innate ability to regenerate the axon of a damaged nerve. It was shown that the CNS lacks the permissive environment for proper axonal regeneration [3]. However, several studies found that CNS axons are capable of small amounts of regeneration, short distance neurite growth within the lesion site under certain conditions [4-6]. The main factors responsible for intrinsically limiting CNS axon regeneration have been believed to be inhibitors found within myelin and the formation of glial scars.

Myelin-associated inhibitors (MIAs) are secreted by oligodendryocytes. Three types of MIAs have been identified, Nogo, myelin-associated glycoprotein (MAG), and oligodendrocyte myelin glycoprotein (OMG) [7]. Nogo, found on the surface of oligodendrocytes and the innermost surface of the myelin membrane in contact with the axon, induces the collapse of the axon growth cone. On the other hand, MAG, found in

the periaxonal membrane which is in contact with axonal receptors, inhibits neurite elongation of mature neurons. Lastly, OMG, found next to the Node of Ranvier, inhibits neurite elongation as well as induces growth cone collapse.

Glial scars are formed by astrocytes when the CNS is injured. The scar creates a physical barrier to prevent axon regeneration from occurring. Also, the molecular composition of the glial scar and the synthesis of inhibitory molecules, such as certain chondroitin sulfate proteoglycans (CSPGs) and cytotactin/tenascin (CT), contribute to regeneration failure [8, 9]. The upregulation of CSPGs near glial scars has been associated with the creation of non-permissive neurite growth environment in the CNS [10]. Therefore, strategies to reduce inhibitory factors and promote permissive factors will help overcome the limitation of nerve regeneration of the CNS.

1.3. Functional restoration of nerve

1.3.1. Peripheral nervous system

Despite advancement of surgical technologies, *complete* functional recovery following nerve damages is rarely achieved due to the poor or absent inherent neural regenerative capabilities of the peripheral nervous system. Damages can be caused by traumatic injuries, infectious diseases, degeneration, autoimmune disorders, and tumors. The functional success of surgical nerve repair following a nerve injury is determined by the degree of injury, the type of repair performed on the damage nerve, delay before surgical intervention, and patient's age. Understanding how these factors affect the result

of nerve regeneration can be beneficial for designing and optimizing tools to enhance recovery for both PNS and CNS. For regeneration to occur, it is a prerequisite for the proximal end of the axons must be able to regrow, the distal site of the injury must be able to support regrowth, and for the target tissue to accept new axons. Different biomaterial and cellular approaches have been attempted to achieve such requirements to enhance nerve regeneration.

1.3.1.1 Nerve grafts

In the case of nerve gaps greater than 30 mm, the current gold standard to repair transected nerves is autologous nerve grafting. This method provides the structural support to guide axon regeneration, preventing the formation of neuromas [11]. Because it is surgically removed from the patient's own body, the autograft, most commonly taken from the sural nerve of the calf region, acts as an immunogenically inert scaffold, providing viable Schwann cells and appropriate neurotrophic factors for axon regeneration [12]. However, this technique possesses many limitations, including the necessity of multiple surgeries, the induction of functionally impaired region where graft was taken from, and disproportion of graft to nerve tissue in size and structure. Furthermore, the patient is at high risk of a neuroma formation in the transplanted area. Alternative clinical options include cadaver allografts [13-15], veins and arteries as grafts [16], and natural/synthetic conduits, but each of these possess their own disadvantages . When using allografts, patients risk a systemic immunoresponse and is not suitable for

nerve gaps greater than 30 mm [17]; vein and artery grafts also cannot bridge nerve gaps greater than 30 mm [18]; and lastly, current clinically-approved natural and synthetic conduits are have not been able to fully repair transected nerves with nerve gaps greater than 30 mm to regain full functionality [19]. To address these limitations, tissue engineering strategies seek to develop nerve guidance conduits to address these limitations.

1.3.1.2. Nerve guidance conduits

When selecting a biomaterial for developing a neuroconduit, the physicochemical, biomechanical, and biological properties must be considered. The material should possess the proper permeability and porosity for nutrition and ion transport. The mechanical properties, such as stiffness and elasticity, should match the native tissue for better integration with surrounding tissue. Lastly, it should be biocompatible and possess the proper surface chemistry.

Natural conduits

Natural biomaterials for neuroconduits are typically either (1) autologous non-neural tissues and decellularized allogenic/xenogenic neural/non-neural tissues or (2) naturally-derived polymers including ECM proteins (collagen, laminin, hyaluraonan) and polysaccharides (agarose, chitosan). Avance® offers commercially available human decellularized nerve allografts. Studies showed that Avance® improved nerve functional

recovery of sensory, motor, and mixed nerves with nerve gaps up to 30 mm [20, 21]. However, the use of the allografts requires additional administration of immunosuppressants for 18 months as well as it is limited in the gap length. Naturally-derived polymeric neuroconduits are immunologically inert. There are several of these neuroconduits that have been FDA approved and are commercially available to use in the clinical setting. NeuroGen®, a commercially available conduit made of collagen type I, showed improved sensory scores for a variety of nerves, but was limited to nerve gaps of an average 13 mm [21]. The common limitation of the wide variety of tested materials is that none have shown reliable success for nerve gaps greater than 30 mm.

Synthetic conduits

Silicone neuroconduits were the first to demonstrate the feasibility of synthetic materials for nerve repair by bridging nerve defects up to 15 mm [22]. However, due to its immunogenic non-permeable properties, the implanted conduit induced permanent fibrotic tissue formation ultimately leading to nerve compression. This led to the development of absorbable synthetic conduits. Biodegradable synthetic biomaterials, including polyglycolic acid (PGA) and poly(D,L-lactide-co-ε-caprolactone) (PCL), have been investigated as a scaffolding material for nerve regeneration. PGA, an FDA-approved biomaterial, has been shown have 86% meaningful recovery of nerve defects less than 30 mm [23]. However, PGA rapidly degrades to lactic acid in 90 days, possibly before the completion of nerve regeneration [24]. PCL, another FDA-approved biomaterial, produces

less acidic degradation byproducts [25]. However, it has reported only a 25% meaningful recovery of nerve defects up to 20 mm [26]. Neurotube ®, made of PGA, and Neurolac®, made of poly(D,L-lactide-co-ε-caprolactone) are neuroconduits that are FDA-approved and commercially available.

The issue with large nerve gaps is limited by the rate of axonal elongation. Native Schwann cells eventually advance ahead of the regenerating axons, no longer providing a sufficient environment for axon growth [27]. Another issue with large nerve gaps is that the disorganization of axon extensions from the growth cone continues to increase as the length of the nerve gap increases [28, 29]. To enhance the outcome of peripheral nerve regeneration through the use of neuroconduits alone, efforts have focused on the incorporation of biochemical cues, such as supportive cells, growth factors and electrical input in order to provide a supportive environment for successful axon regeneration.

1.3.1.3. Cell-based therapy

A method to accelerate axon regeneration and bridging large nerve gaps is the addition of supportive cells to nerve injury site. The cell types currently researched include primary cells, such as Schwann cells and olfactory ensheathing cells (OECs), and stem cells, such as embryonic stem cells (ESCs), induced pluripotent stem cells (iPSCs), neural stem cells (NSCs), and mesenchymal stem cells (MSCs). Cell-based therapy has the potential to create a supportive environment by secretion of axon-promoting factors from these cells for peripheral nerve regeneration.

Schwann cells play an important role in peripheral nerve regeneration, therefore they have been an ideal candidate as transplantable supportive cells. They produce many neurotrophic factors, such as nerve growth factor (NGF), brain-derived neurotrophic factor (BDNF), and plate-derived growth factor (PDGF), to promote the regeneration and enhance the survival of damaged axons [30-33]. Experimentally, transplanted Schwann cells seeded in neuroconduits have been shown to enhance axon regeneration *in vivo* [34-36].

Another source of glia cells, OECs, can synthesize neurotrophic factors. Under normal conditions, OECs can be found in both PNS and CNS. They can provide the neurotrophic support to regenerate nerves and contribute to the myelination process [37-39]. However, to obtain Schwann cells or OECs, a functional nerve must be sacrificed and both have limited expansion capabilities. Therefore, stem cells provide an alternative cell source with promising potential for the development of cell-based therapy for nerve regeneration.

ESCs and iPSCs have the potential to differentiate into derivatives of all three embryonic germ layers. They can provide an unlimited source of cells with long-term proliferation capacity and superior differentiation potential. ESCs have demonstrated the ability to differentiate into neural crest cells [40], which then can further transform into neurons [41] and Schwann cells [42] amongst other mesodermal and ectodermal lineage phenotypes [43, 44]. However, ESCs can induce an immune response, have the potential of teratoma formation, and ethical issues of ESCs harvested during the blastocyst stage

of embryos. iPSCs derived from somatic cells present an alternative cell source for patient-specific therapy, eliminating limitations of ESCs. Established protocols have been developed for iPSC differentiation towards neural lineages [45-47]. However, similar to ESCs, efficient differentiation to end-type cell phenotypes remain challenging, limiting their clinical translatability.

NSCs, derived from the brain, can directly differentiate towards neuronal and glial phenotypes and have been studied for both peripheral and central nerve regeneration [48]. A study determined the efficacy and mechanism of NSCs on sciatic nerve injury in rats [49]. A silicon conduit filled with NSCs bridged a 10 mm nerve gap and observed that NSCs increased the expression of neurotrophic factors, NGF and HGF, of the sciatic nerve. Therefore, it was evident that NSCs have the potential to foster a supportive environment for nerve regeneration. In another study, NSCs implanted into a transected tibial nerve were able to restore function in a denervated rat muscle [50]. Within the transected area, NSC differentiated into neuron-like cells with positive expression of βIII tubulin and glial-like cells with positive expression of GFAP. Native Schwann cells secreted various neurotrophic factors that aided in the differentiation and survival of NSCs.

In contrast to ESCs and NSCs, MSCs derived from bone marrow and adipose tissue provide an easy access and autologous source to stem cells for transplantation therapies. Bone-marrow derived MSCs (BMSCs) and adipose-derived MSCs (ADSCs) can differentiate into neurons, astrocytes, and Schwann cell-like cells [51-53]. Both BMSCs and ADSCs have shown enhanced axon regeneration and myelination capability when transplanted in cell-

seeded scaffolds [54-56]. When directly comparing the performance between BMSCs and ADSCs, there were no significant differences in performance. Low morbidity of harvest site, easy accessibility and wide availability, and superior stem cell characteristics have made ADSCs the preferred option for pre-clinical studies.

1.3.2. Central nervous system

As compared to the PNS, the CNS has a much more limited capacity to self-regeneration. Therefore traumatic injuries and diseases are very debilitating to the patient, often leading to loss of motor, sensory, and cognitive functions, especially for injuries occurring in the C4 or C5 of the cervical spinal cord [57]. The inability of neurons to regenerate after an injury is due to the inhibitive microenvironment created by the presence of inhibitory factors and lack of axon-growth promoting factors [58]. Currently there are no cures for injuries in the CNS, there are only a few treatment options to delay the progression of CNS diseases. Two main strategies for CNS treatment include: neuroprotection and neuroregeneration. Neuroprotection refers to the inhibition of the death of CNS neural cells. Neuroregeneration refers to the regeneration of severed axons and sprouting of existing axons to reinnervate denervated target muscle/organ.

1.3.2.1. Pharmacological treatments

It is critical to immediately begin treatment at the onset of a traumatic injury to prevent complete neurological death. Specifically for spinal cord injury, after the patient

is immobilized to prevent further neural damage, methylprednisolone, a glucocorticoid, can be administered within 8 hours of injury to reduce damage to nerve cells and decrease inflammation [59]. Currently, methylprednisolone is the only approved pharmacotherapy for spinal cord injury, but it has not shown clinically significant effects. Therefore, neural tissue engineering strategies have aimed to address this severely limited area of treatment.

1.3.2.2. Cell-based therapy

Cell-based therapies aim to promote the survival of damaged neural cells or manipulate the local area to more conducive for regeneration by providing neurotrophic factors. MSCs and NSCs are the most investigated for treatment strategies to either regenerate damaged native tissue by replacing damaged cells and directly integrating into the tissue or secreting neurotrophic factors to promote neural regeneration or protection [60-65]. However, the clinical efficacy of cell transplantation strategies have been limited due to uncontrolled differentiation, poor cell survivability, and poor integration with the host tissue.

MSCs have been utilized as a short-term immunosuppressant to preserve threatened neurons and glial cells after injury. They have been shown to stimulate recovery from acute symptoms aggravated by inflammation [66, 67]. However, transplanted MSCs have low survival rate in the adult human CNS [68].

Adult NSCs are capable of differentiating into the three types of neural cell types found in the CNS, neurons, oligodendrocytes, and astrocytes. They have been investigated in combination with growth factors and immunosuppression to treat spinal cord injury [61]. NSCs displayed enhanced survival and differentiation into myelinating oligodendrocytes [69]. More recently, investigators have challenged the negative reputation of astrocytes in CNS regeneration.

1.3.2.3. Injectable hydrogel

Hydrogels mimic the physical, mechanical, and chemical properties of native extracellular matrix to promote cell adhesion, self-renewal, and differentiation [70]. Combining biomolecules and neural cell strategies with hydrogel can further promote cell-material interactions. Studies have shown that NSCs are prone to neuronal differentiation on softer hydrogels, while glial differentiation is induced on stiffer scaffolds [71, 72]. Tseng et al. developed an injectable chitosan-based hydrogel and demonstrated the ability of neurosphere-like NSC aggregates to proliferate than differentiate towards neuronal-linages [73]. Next, they injected the NSC aggregate loaded hydrogel into zebrafish with neural system disorder and monitored the functional recovery. The zebrafish injected with NSC-hydrogel demonstrated the 81% functional recovery, as oppose to 38% recovery with just the hydrogel alone. Although these results show the promising potential of cell-based and hydrogel-based therapies, they are limited by their uncontrollable gelation kinetics, which may result in needle clogging during

hydrogel delivery. Also, due to their slow gelation process, the embedded cell or drug may lose its function due to degradation or diffusion from the target area. Its applicability in humans with structurally distinctive mammalian nerve system is still questionable.

1.3.2.4. Neuroprosthetics

Individuals with C4 or C5 damage in the spinal cord suffer from tetraplegia, the functional loss of upper and lower extremities. Damage occurring at the C5 range results in limitation or completely loss of finger functionality; where as C4 damage also includes limited or loss of function of the hands and elbow movement [74]. Individuals lose their ability to accomplish basic daily tasks and their independence. Since currently there is no treatment to regenerate damaged axons in the spinal cord to regain full functional recovery, neuroprostheses based on functional electrical stimulation can compensate the loss of functional upper extremities. By electrically stimulating the downstream nerves in the forearms, individuals are given the ability to reach, grasp, and pinch with their hands.

Commercially available grasp neuroprostheses have been offered to patients at very early stage of rehabilitation [75]. Multiple surface electrodes are placed on the surface of the skin above muscles responsible for hand movement. A forearm sleeve securely wraps the electrodes and a metal splint is integrated into the sleeve to stabilize the wrist. The electrodes will deliver short electrical current impulses to formally excitable tissue. If a minimum charge density surpasses a threshold, the electrical pulses induce physiological action potentials on nerves, causing contractions of innervated, yet

paralyzed muscles of the hands and the forearms. However, the grasp prostheses possess several disadvantages, such as reproducibility of desired grasping movements. There is significant variation of the grasp patterns in dependence of the wrist rotation angle. Individuals have also complained about complications of placement of electrodes at home, varying muscle function if not placed correctly. Therefore, on-going research is still seeking strategies to restoring full functionality by complete repair of CNS nerves.

1.4. Electrical stimulation

Due to the innate electrical properties of the nervous system, the potential of utilizing electrical stimulation to enhance nerve regeneration and functional recovery has been widely investigated. Electrical stimulation has been shown to facilitate the processes of axonal regeneration by enhancing the secretion of neurotrophic factors from glial cells promoting neurite outgrowth [76, 77]. Several *in vivo* studies demonstrated the efficacy of electrical stimulation promoting nerve outgrowth in rat models of nerve injury, resulting in earlier muscle reinnervation and functional recovery. When electrical stimulation was applied at the time of nerve repair, this resulted in an increased number of sensory neurons that expressed BDNF and its trkB receptor, subsequently accelerating nerve regeneration [78]. When electrical stimulation was applied for 14 days to damaged motor neurons, evident by motor reinnervation occurred at 21 days rather than at approximately 42 days and all the motor neurons had regenerated their axons into the

motor nerve branch within 21 days instead of 56-70 days observed in the sham control [79].

The first human clinical trial showed a promising potential of therapeutic electrical stimulation, where improved post-surgical outcomes were achieved by localized low frequency of electrical stimulation on patients with carpal tunnel syndrome [80]. Despite these positive outcomes, the application of electrical stimulation in the clinical setting is limited by several factors; most significantly, its invasive nature requires the implantation of electrodes protruding through the skin. Furthermore, the electrode approach can activate only neuron(s) in direct contact with or close proximity to the electrodes, resulting in a small localized effective area.

1.5. Piezoelectric materials

Piezoelectric materials can self-generate electric fields under dynamic mechanical strain. Under the direct piezoelectric effect, the materials induce an electric charge separation due to the re-orientation of dipole domains in response to mechanical deformation (tension or compression), providing a means to produce electric potentials without a separate electrical source [81]. Due to its flexibility and biocompatibility, piezoelectric polymers have been used for biomedical applications over its piezoceramic counterparts. There have been several attempts to utilize piezoelectric properties for nerve regeneration [82, 83]. Especially, poly(vinylidene fluoride) (PVDF) and its copolymer poly(vinylidene fluoride-trifluoroethylene) (PVDF-TrFE), have been extensively studied for

such applications due to their excellent biocompatibility and relatively high piezoelectricity [84, 85].

PVDF may exist in four crystalline phases, α, β, γ, and δ phases, depending on the molecular chain conformations as trans or gauche linkages (**Figure 1.4**). It is non-polar in the α crystal phase, while it is polar in the β and γ crystal phases. In order to induce its piezoelectric properties by traditional synthesis methods, the polymer is mechanically stretched to 300% strain followed by poling to induce a net dipole of trans linkage, transforming into the highly polar β crystal phase [86]. Once it is poled, PVDF becomes a ferroelectric polymer, exhibiting both piezoelectric and pyroelectric properties. On the other hand, PVDF-TrFE is directly crystallized into the polar β crystal phase, because TrFE acts as a phase stabilizer. Its degree of crystallinity, thus piezoelectric performance can be further enhanced by thermal treatment.

The first use of PVDF and PVDF-TrFE as a nerve guidance conduit was demonstrated in a rat model. The poled PVDF conduit was implanted into the sciatic nerve of a rat with a 4 mm gap. 4 weeks after implantation, there were a significantly higher amount of myelinated axons than the control group [87]. They also implanted the piezoelectric PVDF-TrFE conduit into a rat sciatic nerve with a 10 mm gap and observed bridging of myelinated axons in 4 weeks, demonstrating the capability of PVDF-TrFE as a nerve guidance conduit for nerve regeneration [88].

More recently, a group of researchers exploited the enhanced piezoelectricity of PVDF-TrFE scaffolds synthesized by electrospinning to accelerate neurite outgrowth of

dorsal root ganglion neurons [89] or promote neural differentiation of human neural stem/progenitor cells *in vitro* [90]. In spite of favorable results, these studies were likely unable to utilize the true potential of piezoelectricity as it requires dynamic straining of the materials to generate electric potentials. They attributed the enhancement of cellular behaviors to piezoelectric responses of the PVDF scaffold by cell exerting forces, but considering minimal straining possible by the cells, the effects were probably due to intrinsic surface charges of the material (**Figure 1.5**).

1.6. Electrospinning

The development of fibrous scaffolds processed by the electrospinning technique has received much attention for neural tissue engineering applications to facilitate the regrowth of damaged nerves [91]. The technique can produce a non-woven or aligned network of fibers that mimic native extracellular matrix (**Figure 1.6**). An engineered scaffold can be loaded with cells and growth factors to promote functional restoration. The surface and mechanical properties of the scaffold, similar to the environmental cues in the extracellular matrix, can stimulate cell self-renewal and differentiation [92, 93]. It also possesses the same architecture as native extracellular matrix, which high surface to volume ratio, allowing more contact between the cells and the scaffold. A wide range of polymers can be used to manipulate the physical and biological properties of the scaffold, from biodegradability, mechanical properties, and surface wettability.

The electrospinning process consists of a high voltage power source, syringe and needle, syringe pump, and a grounded collector. A polymer dissolved in a solvent is loaded into a syringe with a needle and placed on a syringe pump. The polymer solution is ejected at a controlled flow rate by the syringe pump. A high voltage charges the polymer solution and when the electrostatic force overcomes the surface tension of the polymer solution at the tip of the needle, a Taylor cone is formed, elongating the polymer solution into a jet. The charged jet is deposited on to a grounded collector due to the electric field between the needle tip and targeted collector. Randomly-oriented fibers can be collected on a static flat collector, while aligned fibers are typically collected on a high speed rotating mandrel, which allows the fibers to collect in the direction of rotation.

The polymer solution properties (viscosity, conductivity and surface tension), electrospinning parameters (electric field, solution flow rate, and collector type), and environmental conditions (temperature and relative humidity) are the main governing parameters to precisely control the fiber diameter and orientation [94]. It was found that the factor that has the greatest impact on fiber diameter is solution properties, more specifically the solution viscosity, while electro-conductivity and dielectric properties of the solution significantly affect individual fiber morphology.

Structural characteristics of electrospun scaffolds, such as fiber diameter and alignment have been shown to modulate cellular behaviors, especially neural cell types. NSCs have been shown to exhibit the greatest differentiation potential towards neurons on aligned microfibers than that of random and nano-sized electrospun fibers, due to

having a larger platform to extend its neurites in one direction [91]. An aligned electrospun platform also enhanced Schwann cell maturation [95]. These results demonstrate the potential of aligned electrospun scaffolds to prime cells for neural applications.

1.7. Conclusion

A lack of technologies that enable electrically stimulating nervous tissues in a facile and clinically relevant manner has partly hindered the advancement in treating nerve injuries for full functional recovery. In this regard, we aim to develop a mechanical/electrical stimulation system and its utilization in a previously unexplored manner, with which optimized levels of electrical stimulation can be applied to damaged tissue by remotely activating the conduit wrapping around injured nerves via acoustically-driven piezoelectricity. Unlike biochemical-embedded conduit in which the release of neurotrophic factors is limited by loading or electro-conductive conduit in which only passive electrical stimulation by autologous cells is possible without intrusive electrodes, the piezoelectric conduit provides unlimited opportunity to properly stimulate the neuronal cells *in vivo*. Therefore, this project will develop a novel method of peripheral and central nerve treatment that will allow functional recovery of nerve injuries with a previously untreatable large gap in a shorter duration (**Figure 1.7**).

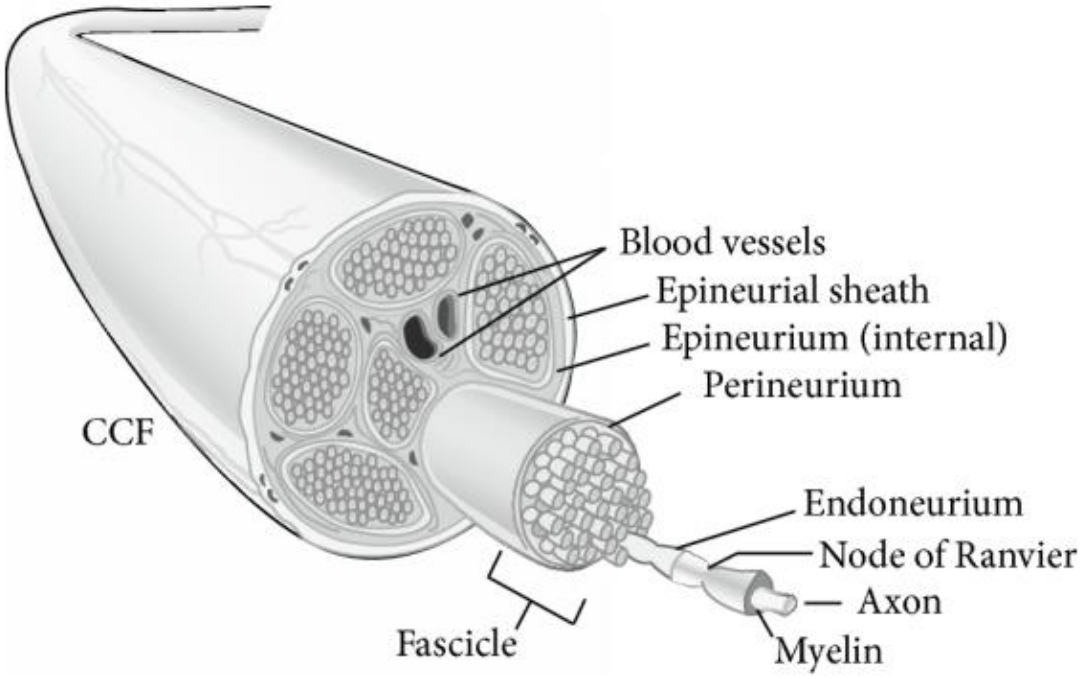

Figure 1.1. Microanatomy of nerve bundle. A nerve bundle is a multi-structured tissue comprised of a bundle of myelinated or unmyelinated axons that are wrapped in connective tissue and blood vessels. [96]

Seddon's classification	Sunderland's classification	Tissues injured
Neurapraxia	Grade I	Myelin
Axonotmesis	Grade II	Myelin, axon
Axonotmesis	Grade III	Myelin, axon, endoneurium
Axonotmesis	Grade IV	Myelin, axon, endoneurium, perineurium
Neurotmesis	Grade V	Myelin, axon, endoneurium, perineurium, epineurium

Table 1.1. Classification of nerve injuries

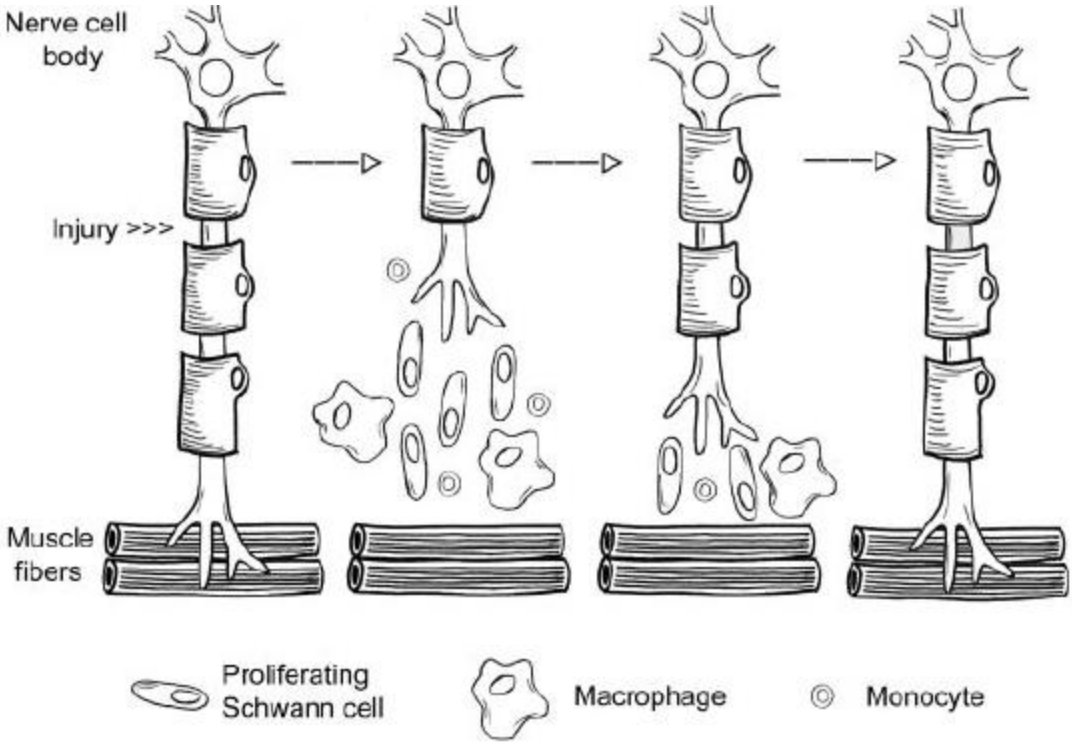

Figure 1.2. Process following nerve injury in the peripheral nervous system. When a peripheral nerve is injured, compressed or transected, Wallerian degeneration begins to remove old nerve from injury site to target muscle/organ leaving behind a connective tissue tube. Once the old nerve is degenerated, peripheral nerve regeneration begins to a certain capacity. [97]

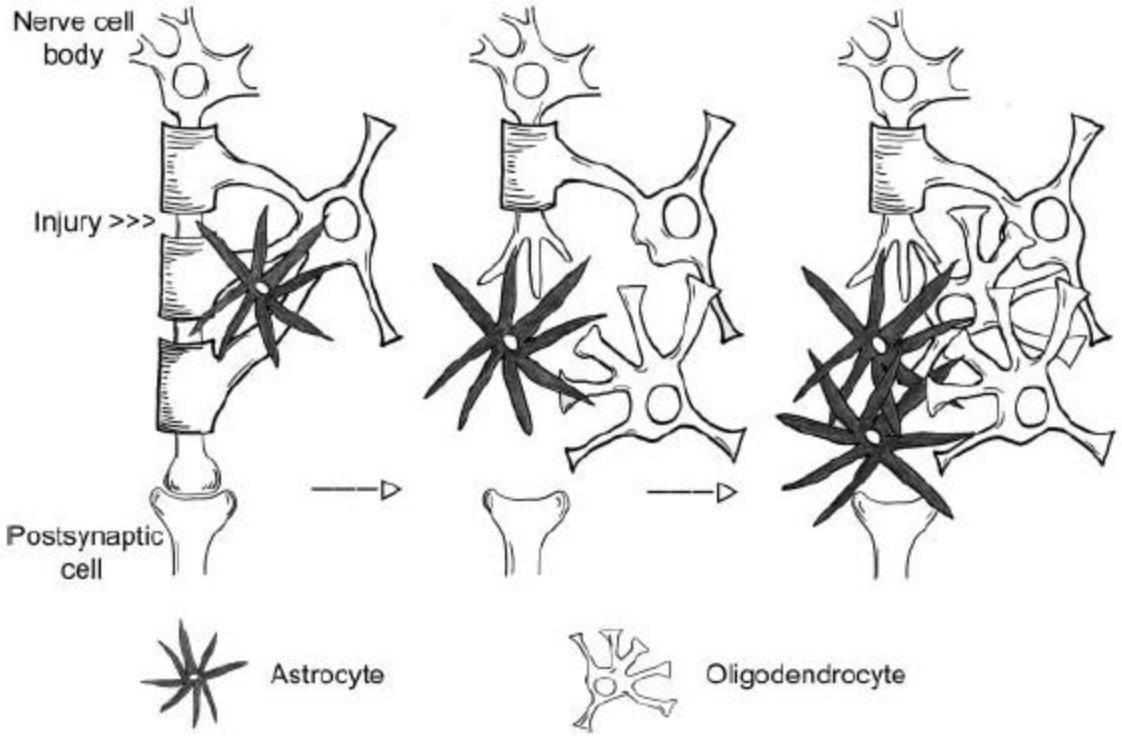

Figure 1.3. Process following nerve injury in the central nervous system. Natively, the central nervous system has a limited capacity of nerve regeneration. When a central nerve is injured, glial cells infiltrate the injury site to begin repair, forming scar tissue. [97]

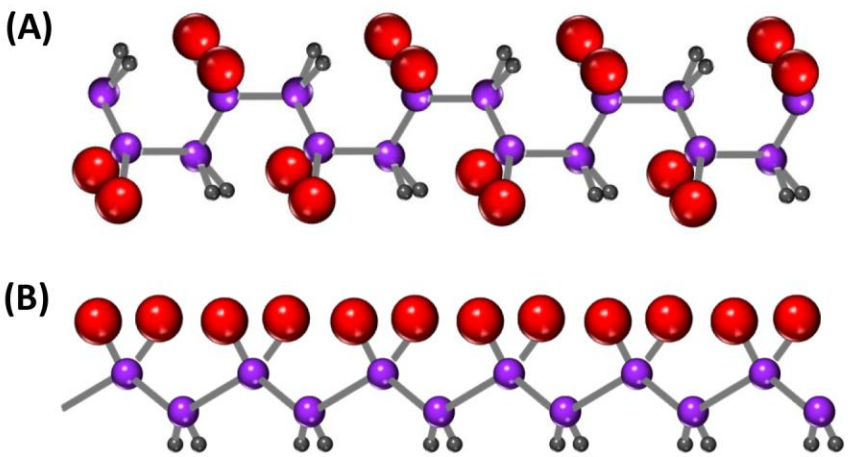

Figure 1.4. Molecular structures of piezoelectric poly(vinylidene fluoride) (PVDF) and their effects on piezoelectricity. PVDF can exist in the (A) non-piezoelectric α crystal phase and (B) piezoelectric β crystal phase.

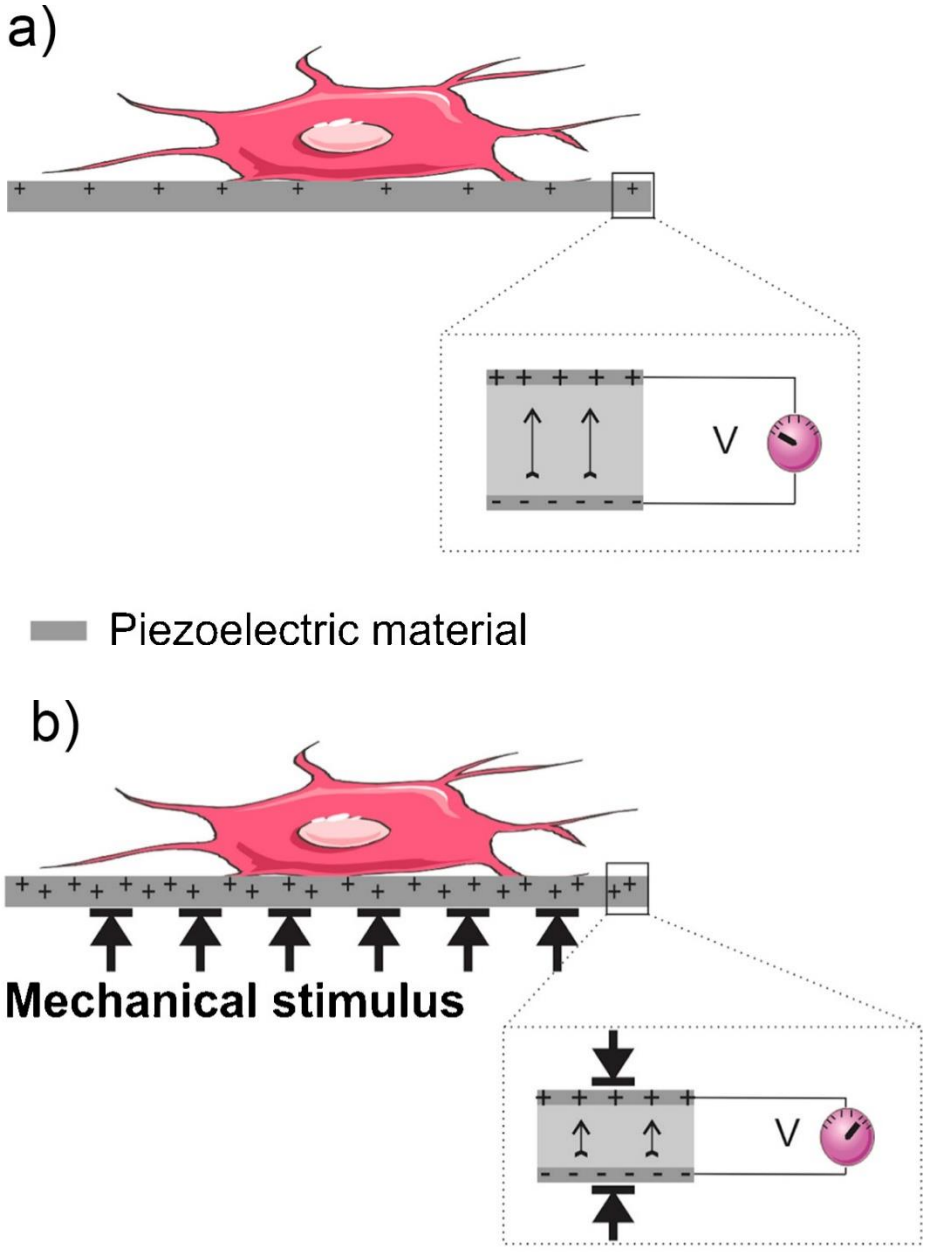

Figure 1.5. Mechanical/electrical stimulation modulates cellular behavior. (a) The static state with native surface charges and (b) activated state under mechanical stress generates surface electric charges that can directly affect adherent cells. [98]

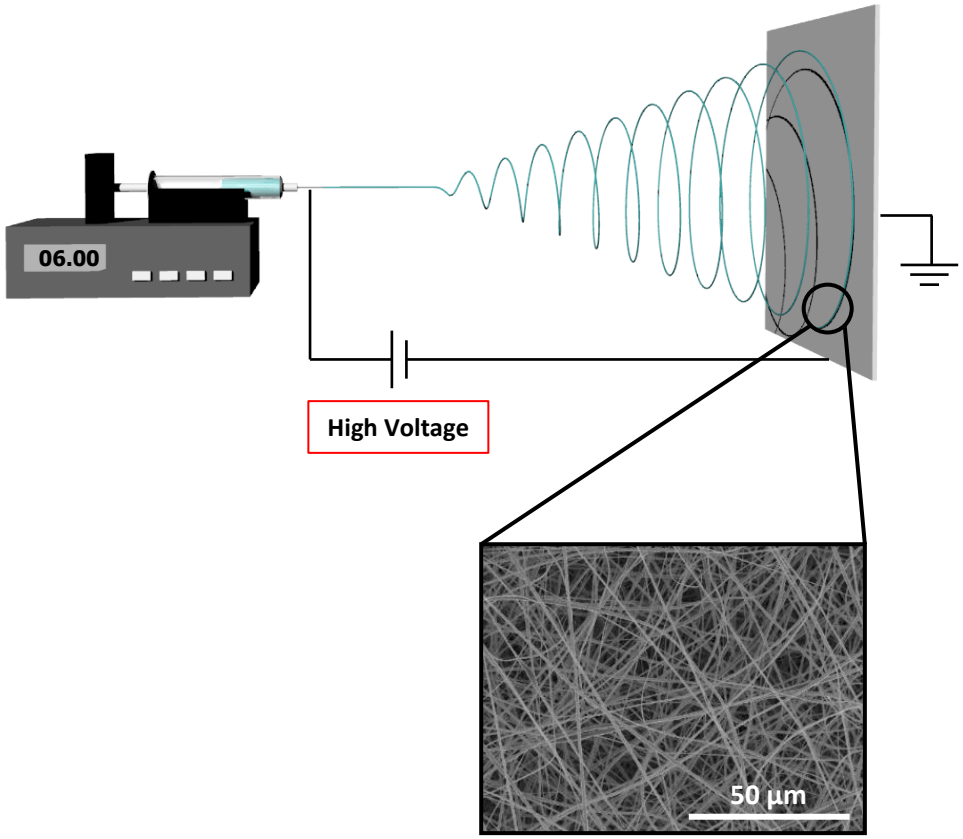

Figure 1.6. Electrospinning produces native extracellular matrix (ECM)-like structures. An electric field elongates a polymeric solution to synthesize fibrous structures with enhanced piezoelectric properties that resemble native ECM.

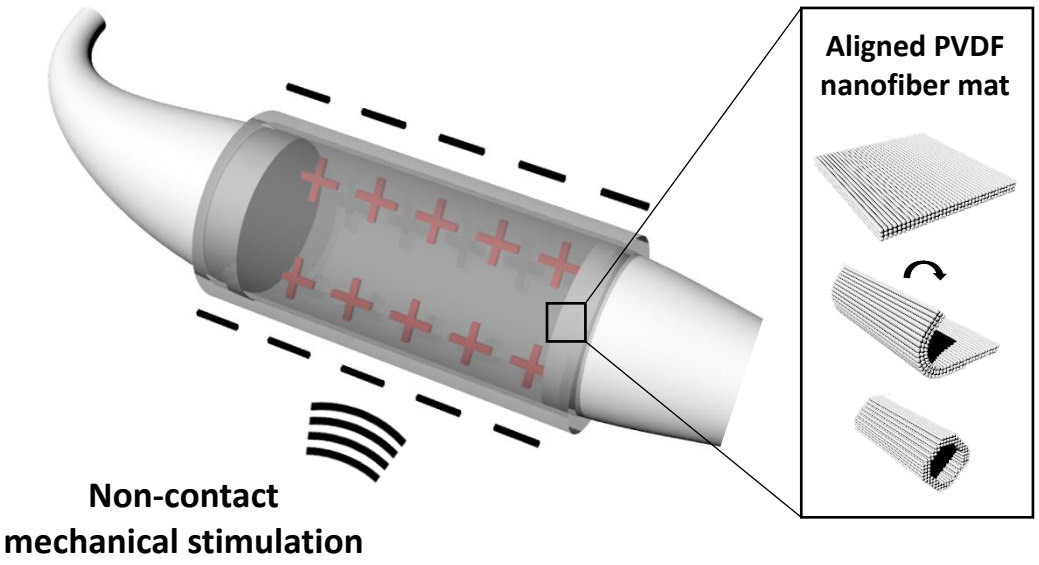

Figure 1.7. A schematic of a piezoelectric neuroconduit composed of electrospun aligned PVDF-TrFE. The implanted neuroconduit can be activated by externally applied mechanical stimulation to produce electric fields for enhancing and promoting nerve regeneration in the PNS and CNS.

References

1. Sunderland, S. and F. Walshe, *Nerves and nerve injuries.* 1968.

2. Patodia, S. and G. Raivich, *Role of Transcription Factors in Peripheral Nerve Regeneration.* Frontiers in Molecular Neuroscience, 2012. **5**: p. 8.

3. Ramon y Cafal, S., *Degeneration and Regeneration of the Nervous System, RM May, ed. and transl.* Hafner, New York, 1928.

4. Davies, S.J., et al., *Regeneration of adult axons in white matter tracts of the central nervous system.* Nature, 1997. **390**(6661): p. 680.

5. David, S. and A.J. Aguayo, *Axonal elongation into peripheral nervous system "bridges" after central nervous system injury in adult rats.* Science, 1981. **214**(4523): p. 931-933.

6. Richardson, P., U. McGuinness, and A. Aguayo, *Axons from CNS neurones regenerate into PNS grafts.* Nature, 1980. **284**(5753): p. 264-265.

7. Cadelli, D., C. Bandtlow, and M. Schwab, *Oligodendrocyte-and myelin-associated inhibitors of neurite outgrowth: their involvement in the lack of CNS regeneration.* Experimental neurology, 1992. **115**(1): p. 189-192.

8. Fitch, M.T. and J. Silver, *CNS injury, glial scars, and inflammation: Inhibitory extracellular matrices and regeneration failure.* Experimental neurology, 2008. **209**(2): p. 294-301.

9. Fawcett, J.W. and R.A. Asher, *The glial scar and central nervous system repair.* Brain research bulletin, 1999. **49**(6): p. 377-391.

10. Sofroniew, M.V., *Molecular dissection of reactive astrogliosis and glial scar formation.* Trends in neurosciences, 2009. **32**(12): p. 638-647.

11. Millesi, H., *Bridging defects: autologous nerve grafts.* How to improve the results of peripheral nerve surgery, 2007: p. 37-38.

12. Dahlin, L. and G. Lundborg, *Use of tubes in peripheral nerve repair.* Neurosurgery Clinics of North America, 2001. **12**(2): p. 341-352.

13. Grand, A.G., et al., *Axonal regeneration after cold preservation of nerve allografts and immunosuppression with tacrolimus in mice.* Journal of neurosurgery, 2002. **96**(5): p. 924-932.

14. Mackinnon, S.E., et al., *Clinical outcome following nerve allograft transplantation.* Plastic and reconstructive surgery, 2001. **107**(6): p. 1419-1429.

15. Kim, B.S., J.J. Yoo, and A. Atala, *Peripheral nerve regeneration using acellular nerve grafts.* Journal of biomedical materials research Part A, 2004. **68**(2): p. 201-209.

16. Battiston, B., et al., *Nerve repair by means of tubulization: literature review and personal clinical experience comparing biological and synthetic conduits for sensory nerve repair.* Microsurgery, 2005. **25**(4): p. 258-267.

17. Udina, E., E. Verdú, and X. Navarro, *Effects of the immunophilin ligand FK506 on nerve regeneration in collagen guides seeded with Schwann cells in rats.* Neuroscience letters, 2004. **357**(2): p. 99-102.

18. Karabekmez, F.E., A. Duymaz, and S.L. Moran, *Early clinical outcomes with the use of decellularized nerve allograft for repair of sensory defects within the hand*, 2009, SAGE Publications Sage CA: Los Angeles, CA.

19. Kehoe, S., X.F. Zhang, and D. Boyd, *FDA approved guidance conduits and wraps for peripheral nerve injury: A review of materials and efficacy.* Injury, 2012. **43**(5): p. 553-572.

20. Neubauer, D., J.B. Graham, and D. Muir, *Chondroitinase treatment increases the effective length of acellular nerve grafts.* Experimental neurology, 2007. **207**(1): p. 163-170.

21. Whitlock, E.L., et al., *Processed allografts and type I collagen conduits for repair of peripheral nerve gaps.* Muscle & Nerve, 2009. **39**(6): p. 787-799.

22. Merle, M., et al., *Complications from silicon-polymer intubulation of nerves.* Microsurgery, 1989. **10**(2): p. 130-133.

23. Mackinnon, S.E. and A.L. Dellon, *Clinical nerve reconstruction with a bioabsorbable polyglycolic acid tube.* Plastic and reconstructive surgery, 1990. **85**(3): p. 419-424.

24. de Tayrac, R., et al., *Long-lasting bioresorbable poly (lactic acid)(PLA94) mesh: a new approach for soft tissue reinforcement based on an experimental pilot study.* International Urogynecology Journal, 2007. **18**(9): p. 1007-1014.

25. Sun, H., et al., *The in vivo degradation, absorption and excretion of PCL-based implant.* Biomaterials, 2006. **27**(9): p. 1735-1740.

26. Chiriac, S., et al., *Experience of using the bioresorbable copolyester poly (DL-lactide-ε-caprolactone) nerve conduit guide Neurolac™ for nerve repair in peripheral nerve defects: report on a series of 28 lesions.* Journal of Hand Surgery (European Volume), 2012. **37**(4): p. 342-349.

27. Son, Y.-J., J.T. Trachtenberg, and W.J. Thompson, *Schwann cells induce and guide sprouting and reinnervation of neuromuscular junctions.* Trends in neurosciences, 1996. **19**(7): p. 280-285.

28. Menorca, R.M., T.S. Fussell, and J.C. Elfar, *Peripheral nerve trauma: mechanisms of injury and recovery.* Hand clinics, 2013. **29**(3): p. 317.

29. Ertürk, A., et al., *Disorganized microtubules underlie the formation of retraction bulbs and the failure of axonal regeneration.* Journal of Neuroscience, 2007. **27**(34): p. 9169-9180.

30. Frostick, S.P., Q. Yin, and G.J. Kemp, *Schwann cells, neurotrophic factors, and peripheral nerve regeneration.* Microsurgery, 1998. **18**(7): p. 397-405.

31. Menei, P., et al., *Schwann cells genetically modified to secrete human BDNF promote enhanced axonal regrowth across transected adult rat spinal cord.* European Journal of Neuroscience, 1998. **10**(2): p. 607-621.

32. Assouline, J.G., et al., *Rat astrocytes and Schwann cells in culture synthesize nerve growth factor-like neurite-promoting factors.* Developmental Brain Research, 1987. **31**(1): p. 103-118.

33. Jessen, K., et al., *The Schwann cell precursor and its fate: a study of cell death and differentiation during gliogenesis in rat embryonic nerves.* Neuron, 1994. **12**(3): p. 509-527.

34. Hadlock, T., et al., *A polymer foam conduit seeded with Schwann cells promotes guided peripheral nerve regeneration.* Tissue engineering, 2000. **6**(2): p. 119-127.

35. Keilhoff, G., et al., *In vivo predegeneration of peripheral nerves: an effective technique to obtain activated Schwann cells for nerve conduits.* Journal of neuroscience methods, 1999. **89**(1): p. 17-24.

36. Evans, G.R., et al., *Bioactive poly (L-lactic acid) conduits seeded with Schwann cells for peripheral nerve regeneration.* Biomaterials, 2002. **23**(3): p. 841-848.

37. Li, Y., P.M. Field, and G. Raisman, *Repair of adult rat corticospinal tract by transplants of olfactory ensheathing cells.* Science, 1997. **277**(5334): p. 2000-2002.

38. Li, Y., P.M. Field, and G. Raisman, *Regeneration of adult rat corticospinal axons induced by transplanted olfactory ensheathing cells.* Journal of Neuroscience, 1998. **18**(24): p. 10514-10524.

39. Dombrowski, M.A., et al., *Myelination and nodal formation of regenerated peripheral nerve fibers following transplantation of acutely prepared olfactory ensheathing cells.* Brain research, 2006. **1125**(1): p. 1-8.

40. Lee, G., et al., *Isolation and directed differentiation of neural crest stem cells derived from human embryonic stem cells.* Nature biotechnology, 2007. **25**(12): p. 1468.

41. Okabe, S., et al., *Development of neuronal precursor cells and functional postmitotic neurons from embryonic stem cells in vitro.* Mechanisms of development, 1996. **59**(1): p. 89-102.

42. Joseph, N.M., et al., *Neural crest stem cells undergo multilineage differentiation in developing peripheral nerves to generate endoneurial fibroblasts in addition to Schwann cells.* Development, 2004. **131**(22): p. 5599-5612.

43. Tada, S., et al., *Characterization of mesendoderm: a diverging point of the definitive endoderm and mesoderm in embryonic stem cell differentiation culture.* Development, 2005. **132**(19): p. 4363-4374.

44. D'Amour, K.A., et al., *Efficient differentiation of human embryonic stem cells to definitive endoderm.* Nature biotechnology, 2005. **23**(12): p. 1534.

45. Karumbayaram, S., et al., *Directed Differentiation of Human-Induced Pluripotent Stem Cells Generates Active Motor Neurons.* Stem cells, 2009. **27**(4): p. 806-811.

46. Dimos, J.T., et al., *Induced pluripotent stem cells generated from patients with ALS can be differentiated into motor neurons.* Science, 2008. **321**(5893): p. 1218-1221.

47. Hu, B.-Y., et al., *Neural differentiation of human induced pluripotent stem cells follows developmental principles but with variable potency.* Proceedings of the National Academy of Sciences, 2010. **107**(9): p. 4335-4340.

48. Clarke, D.L., et al., *Generalized potential of adult neural stem cells.* Science, 2000. **288**(5471): p. 1660-1663.

49. Xu, L., et al., *Neural stem cells enhance nerve regeneration after sciatic nerve injury in rats.* Molecular neurobiology, 2012. **46**(2): p. 265-274.

50. Lin, S., et al., *Optimal time-point for neural stem cell transplantation to delay denervated skeletal muscle atrophy.* Muscle & Nerve, 2013. **47**(2): p. 194-201.

51. Ahmadi, N., et al., *Stability of neural differentiation in human adipose derived stem cells by two induction protocols.* Tissue and Cell, 2012. **44**(2): p. 87-94.

52. Ning, H., et al., *Neuron-like differentiation of adipose tissue-derived stromal cells and vascular smooth muscle cells.* Differentiation, 2006. **74**(9-10): p. 510-518.

53. Zhang, H.-T., et al., *Neural differentiation ability of mesenchymal stromal cells from bone marrow and adipose tissue: a comparative study.* Cytotherapy, 2012. **14**(10): p. 1203-1214.

54. Wang, J., et al., *Bone marrow mesenchymal stem cells promote cell proliferation and neurotrophic function of Schwann cells in vitro and in vivo.* Brain research, 2009. **1262**: p. 7-15.

55. Wang, Y., et al., *Recellularized nerve allografts with differentiated mesenchymal stem cells promote peripheral nerve regeneration.* Neuroscience letters, 2012. **514**(1): p. 96-101.

56. Sun, F., et al., *Combined use of decellularized allogeneic artery conduits with autologous transdifferentiated adipose-derived stem cells for facial nerve regeneration in rats.* Biomaterials, 2011. **32**(32): p. 8118-8128.

57. Michael, J., J.S. Krause, and D.P. Lammertse, *Recent trends in mortality and causes of death among persons with spinal cord injury.* Archives of physical medicine and rehabilitation, 1999. **80**(11): p. 1411-1419.

58. Dumont, R.J., et al., *Acute spinal cord injury, part I: pathophysiologic mechanisms.* Clinical neuropharmacology, 2001. **24**(5): p. 254-264.

59. Bracken, M.B., et al., *Administration of methylprednisolone for 24 or 48 hours or tirilazad mesylate for 48 hours in the treatment of acute spinal cord injury: results of the Third National Acute Spinal Cord Injury Randomized Controlled Trial.* Jama, 1997. **277**(20): p. 1597-1604.

60. Teng, Y.D., et al., *Functional recovery following traumatic spinal cord injury mediated by a unique polymer scaffold seeded with neural stem cells.* Proceedings of the National Academy of Sciences, 2002. **99**(5): p. 3024-3029.

61. Abematsu, M., et al., *Neurons derived from transplanted neural stem cells restore disrupted neuronal circuitry in a mouse model of spinal cord injury.* The Journal of clinical investigation, 2010. **120**(9): p. 3255.

62. Hofstetter, C., et al., *Marrow stromal cells form guiding strands in the injured spinal cord and promote recovery.* Proceedings of the National Academy of Sciences, 2002. **99**(4): p. 2199-2204.

63. Chopp, M., et al., *Spinal cord injury in rat: treatment with bone marrow stromal cell transplantation.* Neuroreport, 2000. **11**(13): p. 3001-3005.

64. Lu, P., et al., *Neural stem cells constitutively secrete neurotrophic factors and promote extensive host axonal growth after spinal cord injury.* Experimental neurology, 2003. **181**(2): p. 115-129.

65. Ankeny, D.P., D.M. McTigue, and L.B. Jakeman, *Bone marrow transplants provide tissue protection and directional guidance for axons after contusive spinal cord injury in rats.* Experimental neurology, 2004. **190**(1): p. 17-31.

66. Zeng, X., et al., *Bone marrow mesenchymal stem cells in a three-dimensional gelatin sponge scaffold attenuate inflammation, promote angiogenesis, and reduce cavity formation in experimental spinal cord injury.* Cell Transplantation, 2011. **20**(11-12): p. 1881-1899.

67. Nakajima, H., et al., *Transplantation of mesenchymal stem cells promotes an alternative pathway of macrophage activation and functional recovery after spinal cord injury.* Journal of neurotrauma, 2012. **29**(8): p. 1614-1625.

68. Parr, A.M., C.H. Tator, and A. Keating, *Bone marrow-derived mesenchymal stromal cells for the repair of central nervous system injury.* Bone marrow transplantation, 2007. **40**(7): p. 609.

69. Hammang, J., D. Archer, and I. Duncan, *Myelination following transplantation of EGF-responsive neural stem cells into a myelin-deficient environment.* Experimental neurology, 1997. **147**(1): p. 84-95.

70. Banerjee, A., et al., *The influence of hydrogel modulus on the proliferation and differentiation of encapsulated neural stem cells.* Biomaterials, 2009. **30**(27): p. 4695-4699.

71. Teixeira, A.I., et al., *The promotion of neuronal maturation on soft substrates.* Biomaterials, 2009. **30**(27): p. 4567-4572.

72. Leipzig, N.D. and M.S. Shoichet, *The effect of substrate stiffness on adult neural stem cell behavior.* Biomaterials, 2009. **30**(36): p. 6867-6878.

73. Tseng, T.C., et al., *An injectable, self-healing hydrogel to repair the central nervous system.* Advanced materials, 2015. **27**(23): p. 3518-3524.

74. White, N.-H. and N.-H. Black, *Spinal cord injury (SCI) facts and figures at a glance.* 2016.

75. Rupp, R., et al., *Functional rehabilitation of the paralyzed upper extremity after spinal cord injury by noninvasive hybrid neuroprostheses.* Proceedings of the IEEE, 2015. **103**(6): p. 954-968.

76. Kanzaki, S., et al., *Glial cell line-derived neurotrophic factor and chronic electrical stimulation prevent VIII cranial nerve degeneration following denervation.* Journal of Comparative Neurology, 2002. **454**(3): p. 350-360.

77. Al-Majed, A.A., et al., *Brief electrical stimulation promotes the speed and accuracy of motor axonal regeneration.* Journal of Neuroscience, 2000. **20**(7): p. 2602-2608.

78. Geremia, N.M., et al., *Electrical stimulation promotes sensory neuron regeneration and growth-associated gene expression.* Experimental neurology, 2007. **205**(2): p. 347-359.

79. Brushart, T., *Motor axons preferentially reinnervate motor pathways.* Journal of Neuroscience, 1993. **13**(6): p. 2730-2738.

80. Gordon, T., et al., *Brief post-surgical electrical stimulation accelerates axon regeneration and muscle reinnervation without affecting the functional measures in carpal tunnel syndrome patients.* Experimental neurology, 2010. **223**(1): p. 192-202.

81. Vijaya, M., *Piezoelectric materials and devices: applications in engineering and medical sciences*2012: CRC Press.

82. Fine, E.G., et al., *Improved nerve regeneration through piezoelectric vinylidenefluoride-trifluoroethylene copolymer guidance channels.* Biomaterials, 1991. **12**(8): p. 775-780.

83. Aebischer, P., et al., *Piezoelectric guidance channels enhance regeneration in the mouse sciatic nerve after axotomy.* Brain research, 1987. **436**(1): p. 165-168.

84. Teixeira, L., et al., *In vitro biocompatibility of poly (vinylidene fluoride–trifluoroethylene)/barium titanate composite using cultures of human periodontal ligament fibroblasts and keratinocytes.* Acta biomaterialia, 2010. **6**(3): p. 979-989.

85. Beloti, M.M., et al., *In vitro biocompatibility of a novel membrane of the composite poly (vinylidene-trifluoroethylene)/barium titanate.* Journal of biomedical materials research Part A, 2006. **79**(2): p. 282-288.

86. Gregorio, R. and E. Ueno, *Effect of crystalline phase, orientation and temperature on the dielectric properties of poly (vinylidene fluoride)(PVDF).* Journal of Materials Science, 1999. **34**(18): p. 4489-4500.

87. Delaviz, H., et al., *Repair of peripheral nerve defects using a polyvinylidene fluoride channel containing nerve growth factor and collagen gel in adult rats.* Cell Journal (Yakhteh), 2011. **13**(3): p. 137.

88. Delaviz, H., et al., *Ultrastructural Changes in Spinal Motoneurons and Locomotor Functional Study after Sciatic Nerve Repair in Conduit Tube.* Iranian journal of basic medical sciences, 2012. **15**(4): p. 990.

89. Lee, Y.-S., G. Collins, and T.L. Arinzeh, *Neurite extension of primary neurons on electrospun piezoelectric scaffolds.* Acta biomaterialia, 2011. **7**(11): p. 3877-3886.

90. Lee, Y.-S. and T.L. Arinzeh, *The influence of piezoelectric scaffolds on neural differentiation of human neural stem/progenitor cells.* Tissue Engineering Part A, 2012. **18**(19-20): p. 2063-2072.

91. Yang, F., et al., *Electrospinning of nano/micro scale poly (L-lactic acid) aligned fibers and their potential in neural tissue engineering.* Biomaterials, 2005. **26**(15): p. 2603-2610.

92. Maldonado, M., et al., *The effects of electrospun substrate-mediated cell colony morphology on the self-renewal of human induced pluripotent stem cells.* Biomaterials, 2015. **50**: p. 10-19.

93. Maldonado, M., et al., *Enhanced Lineage-Specific Differentiation Efficiency of Human Induced Pluripotent Stem Cells by Engineering Colony Dimensionality Using Electrospun Scaffolds.* Advanced healthcare materials, 2016. **5**(12): p. 1408-1412.

94. Beachley, V. and X. Wen, *Effect of electrospinning parameters on the nanofiber diameter and length.* Materials Science and Engineering: C, 2009. **29**(3): p. 663-668.

95. Chew, S.Y., et al., *The effect of the alignment of electrospun fibrous scaffolds on Schwann cell maturation.* Biomaterials, 2008. **29**(6): p. 653-661.

96. Siemionow, M. and G. Brzezicki, *Current techniques and concepts in peripheral nerve repair.* International review of neurobiology, 2009. **87**: p. 141-172.

97. Ba, M. and F. Bonhoeffer, *Perspectives on axonal regeneration in the mammalian CNS.* Trends in neurosciences, 1994. **17**(11): p. 473-479.

98. Ribeiro, C., et al., *Piezoelectric polymers as biomaterials for tissue engineering applications.* Colloids and Surfaces B: Biointerfaces, 2015. **136**: p. 46-55.

CHAPTER 2. DEVELOPMENT OF A PIEZOELECTRIC CELL CULTURE SYSTEM FOR NEUROENGINEERING STUDIES

Abstract

Due to the innate electrical behavior of nerve tissue, the use of electrical stimulation to enhance nerve regeneration is widely investigated. The activation of neural cells by electrical stimulation has been demonstrated to play a significant role in enhancing functional recovery of degenerated neurons. However, the application of electrical stimulation for axon regrowth has been limited in the clinical setting due to the invasiveness of electrodes and limited effective area. In the present study, we designed and developed a cell culture system to deliver electrical stimulation to neural cells in vitro, by non-contact activation of a piezoelectric-responsive polyvinylidene fluoride trifluoroethylene (PVDF-TrFE) to demonstrate the feasibility of using piezoelectric materials for nerve regeneration. The electrospinning technique was utilized to synthesize aligned nanofibrous structures to control the nanostructure of the PVDF-TrFE. We demonstrate the capability the piezoelectric cell culture system to precisely control the electric potential generation of the PVDF-TrFE by modulating the fiber diameter and scaffold thickness while the system provides a means to sterilely culture cells. This cell culture system can be utilized for various neuroengineering studies to examine the effects of mechanical/electrical stimulation on nerve regeneration.

2.1. Introduction

Nerve damage due to traumatic injuries or degenerative diseases, such as diabetic neuropathy or neurofibromatosis, is not only potentially fatal, but also have a debilitating effect on the quality of life. Despite surgical intervention, full functional recovery is rarely achieved. The deficiency of complete axon regeneration is not due to the lack of cellular capability, rather the unfavorable growth environment within the damage tissue preventing axon regeneration. To overcome this, tissue engineering strategies have focused on altering the cellular, molecular, and physical environment to promote proper nerve regeneration. Researchers have incorporated various types of stem cells, including induced pluripotent stem cells (iPSCs) [1, 2], neural stem cells (NSCs) [3, 4], and mesenchymal stem cells (MSCs) [5, 6] into implantable neuroconduits to enhance axonal regeneration. In addition to these cellular strategies, nerve growth factor (NGF), a neurotrophic protein, has been incorporated to further stimulate nerve regeneration [7-9]. However, such biochemical factors have a short half-life and fast diffusion rate, limiting its use *in vivo* for axonal regeneration that requires long-term stimulation.

As a biophysical cue, electrical stimulation has been shown to have the ability to initiate an action potential of a damaged neuron to enhance the axon regeneration process [7-9]. When a neuron is exposed to electrical current, i.e., by ion movement across the cell membrane, it creates a gradient of extracellular electrical potential. If the electrical potential is above a threshold, it induces the depolarization of the axon membrane, generating an action potential. Exogenous electrical stimulation has been

also shown to initiate such signaling processes, which induce anabolic activities of neural cells, collectively promoting nerve regeneration. In this regard, conductive materials have been commonly used as an electrical substrate suitable for the electrical stimulation of neural cells [7-9]. However, their invasive implantations of electrodes to activate the conductive materials make its translational usage limited.

To address this issue, piezoelectric materials have drawn attention as a potential generating material activated by mechanical stimulation. Especially, polyvinylidene fluoride (PVDF), a piezoelectric polymer, provides an opportunity to develop nerve conduits due to its high piezoelectricity, biocompatibility, and mechanical compliance. Indeed, several studies have shown enhanced nerve regeneration by the utilization of the PVDF *in vitro*, such as neurite elongation dorsal root ganglion [10], and *in vivo*, such as partial functional recovery when a PVDF conduit was implant [11].

Electrospinning is a facile technique to synthesize nanofibers of almost any polymers, including PVDF, producing a structure that closely resembles the native extracellular matrix (ECM) of tissues [12, 13]. Modification of the electrospinning process easily controls the physical properties of the scaffold, such as fiber diameter and alignment, which affect the piezoelectricity of PVDF and modulate cellular behaviors [10, 14]. The fiber diameter of electrospun PVDF regulates the uniformity and alignment of piezoelectric domains, determining piezoelectric constants [15]. Such changes in substrate morphology also affect cellular behaviors. When comparing neurite growth of neural cell types on randomly-oriented and aligned fiber mats, the cells displayed

enhanced neurite elongation on the aligned morphology, likely due to the native elongated structure of neurons[10] .

In this regard, a system composed of a chamber with an insertable piezoelectric cell culture scaffold and a vertical translation stage, was develop to apply non-contact electrical stimulation to adherent cells to examine cellular behaviors for neural applications. Aligned piezoelectric fibers made of polyvinylidene fluoride trifluoroethylene (PVDF-TrFE) were synthesized by electrospinning and their morphological and piezoelectric properties were characterized. The effects of PVDF-TrFE fiber diameter and scaffold thickness on electric potential generation were investigated to determine an optimum condition for cellular studies.

2.2. Materials and Methods

2.2.1. Synthesis and morphological characterization of nanofibrous PVDF-TrFE scaffolds

PVDF-TrFE (Solvay, Belgium) was dissolved at various concentrations in different solvent systems to produce a range of different electrospun fiber diameters, similar to our previous report (ref). A 16 wt.% PVDF-TrFE (70:30 mol%) was dissolved in a 60/40 volume ratio of *N*,*N*-dimethylformamide (DMF) (Sigma Aldrich, St. Louis, MO) to methyl ethyl ketone (MEK) (Sigma Aldrich) solvent system. 11.5 wt.% and 7 wt.% PVDF-TrFE were dissolved in a 60/40 volume ratio of DMF to acetone solvent system, with the addition of 1 wt.% pyridinium formate (PF) buffer (Sigma Aldrich). The solutions were magnetically stirred at 1200 rpm for 3 hr at room temperature. The PVDF-TrFE solutions were

individually electrospun using a high speed grounded mandrel rotating at 47.9 m/s to produce aligned fibers (**Figure 2.1**). To further enhance the piezoelectric properties of PVDF-TrFE, the electrospun fiber mats were subjected to annealing at 90 °C for 24 hr.

The fiber morphology, diameter and alignment were characterized using scanning electron microscopy (SEM, Vega3, Tescan, Pleasanton, CA). The fibers were sputter-coated with gold to visualize under SEM. Using the ImageJ software, at least 100 individual fibers were assessed to determine the average fiber diameter and alignment. The thickness of the fiber mat was controlled by adjusting the deposition time.

2.2.2. Cell culture chamber design

A cell culture system was designed to apply non-contact mechanical/electrical stimulation to the nanofibrous PVDF-TrFE scaffolds while sterilely culture cells adherent to the scaffolds (**Figure 2.2A**). The device was designed to fit into a standard 6-well tissue culture plate. The top and bottom casings were 3D printed with acrylonitrile butadiene styrene (ABS) to sustain a silicone o-ring on both sides. When assembled, the PVDF scaffold is securely held by the silicone o-rings. Stainless steel screws were utilized to hold the two casings together. The hollow center provides a space to host a PVDF-TrFE scaffold having the dimensions of 15 mm x 5 mm with cell culture media.

2.2.3. Potential generation measurement

To determine the potential generation of the PVDF-TrFE nanofibers, acellular nanofibrous scaffolds assembled in the cell culture system were subjected to non-contact mechanical stimulation (**Figure 2.2B**). PVDF-TrFE scaffolds were cut to the dimensions of 45 mm by 5 mm. The excess length allows the scaffold to protrude outside of the chamber for alligator clamp attachment to an oscilloscope. Gold electrodes with the dimension 40 mm by 4 mm were sputtered on both sides of the scaffolds. A hydrophobic polymer, poly(styrene-b-isobutylene-b-stryrene) (SIBS) was applied to the gold sputtered scaffolds in the location where it would be compressed by the silicone o-rings, to prevent damage to the fiber structures and solution leak. The scaffold was then assembled into the cell culture system and 3 mL of DI water was added to the center of the chamber. The chamber was placed on a vertical translation stage, actuated by a subwoofer speaker (**Figure 2.2C**). The speaker was controlled by a function generator operated by LabView to stimulate the PVDF-TrFE scaffold inside the device at 3 Hz with various magnitudes. The strains experienced by the scaffolds under various magnitudes of actuation were calculated from the captured images of scaffolds under stimulation. The resulting voltage generation was recorded by an oscilloscope. The peak to peak output voltage was determined for 200, 500, and 800 nm fiber diameter at various scaffold thicknesses.

2.3. Results

2.3.1. Synthesis of piezoelectric PVDF-TrFE nanofibers

Figure 2.3 shows the microstructure of electrospun fibers synthesized by various concentrations of PVDF-TrFE examined by SEM. Due to the high angular velocity of the rotating mandrel, the fibers are aligned with a relatively uniform size having a typical cylindrical morphology. A quantitative analysis of the fibers indicates the tightly controlled average fiber diameter for the three conditions (**Figure 2.4A-C**). The average fiber diameter from 7% PVDF-TrFE dissolved in DMF/Acetone with PF buffer is 205 ± 28 nm; 11.5% PVDF-TrFE dissolved in DMF/Acetone with PF buffer is 498 ± 57 nm; and 16% PVDF-TrFE dissolved in DMF/MEK is 802 ± 16 nm. Fiber diameters will be referred as 800, 500, and 200 nm from here on. The fiber alignment was also assessed by measuring tilt angles of individual fibers from an arbitrary neutral axis, showing above 90% within 20° deviation in all conditions (**Figure 2.4D-F**). A comprehensive table including the solution mixture, electrospinning parameters, and fiber morphological analyses can be found in **Table 2.1**. The thickness of the fiber mat was controlled by adjusting the electrospinning duration. The deposition rates for 200, 500, 800 nm fiber diameter scaffolds were approximately 11.5, 46.3, and 103.0 μm/hr, respectively (**Figure 2.5**).

2.3.2. Quantification of potential generation from PVDF-TrFE nanofibers

When the PVDF-TrFE scaffolds are subjected to mechanical stimulation within the piezoelectric cell culture system, a charge separation occurs with an opposing polarity on

each side (**Figure 2.2B**). This charge separation was recorded as a positive to negative voltage peak by an oscilloscope. The peak-to-peak voltage was recorded at various strains to determine a relationship between strain and output voltage. As expected, when the applied strain increased, the peak-to-peak voltage increased (**Figures 2.6, 2.7, and 2.8**). For a fiber mat with the fiber diameter of 200 nm and a fiber mat thickness of 54 μm, at the highest strain of 0.037%, the scaffold produced 437 ± 78 mV_{p-p} and at the lowest strain of 0.027%, it produced 38 ± 34 mV_{p-p}. At the same fiber mat thickness, a scaffold with the fiber diameter of 500 nm produced 234 ± 27 mV_{p-p} at 0.035% strain and 34 ± 12 mV_{p-p} at 0.024% strain; a scaffold with the fiber diameter of 800 nm produced 191 ± 13 mV_{p-p} at 0.033% strain and 27 ± 17 mV_{p-p} at 0.023% strain. Finally, the output voltage was recorded at various thicknesses. **Figure 2.9** shows the relationship between applied strain to the PVDF-TrFE scaffold and its output voltage production at 200, 500, and 800 nm fiber diameter at various thicknesses.

2.4. Discussion

Due to the innate electro-responsive characteristics of neural cells, electrical stimulation has been widely studied to enhance neural cell behavior *in vitro* [16-19] and *in vivo* [20-23]. Typically, this method was approached by implantation of external electrodes alone for a large stimulation area or combined with electro-conductive material for direct and localized electrical stimulation. In this regard, piezoelectric materials provide an opportunity to subject a precisely localized neural tissue area to

electrical stimulation without invasive electrodes via non-contact mechanical perturbation. For example, PVDF-TrFE, a piezoelectric polymer, becomes a charged capacitor under mechanical strain to induce electric charge separation between to the two parallel surfaces.

Electrospinning provides a facile means of synthesizing nanofibrous scaffolds by controlling polymer solution properties, electrospinning parameters, and environmental conditions. It can also induce the formation of β crystal phase of PVDF-TrFE, the crystal structure making it piezoelectric [15]. During electrospinning, a high voltage source is applied to the polymeric solution to elongate into a very fine jet, making the polymer chains orientate along the fiber length. The molecular conformation for the β crystal phase has the longest chain length amongst the possible five crystal phases. Therefore, the intensive stretching by the electrospinning processes facilitates the conversion of PVDF into β crystal phase, while the solvent evaporation helps retain β crystal phase conformation in the solid fiber. β crystal phase has a direct relationship to voltage output, therefore, the greater the β crystal phase content, the greater the voltage output.

In order to mechanically stimulate the implanted piezoelectric material in a non-contact manner *in vivo*, extracorporeal shockwave therapy (ESWT) is an ideal candidate. ESWT is a widely utilized method to regenerate damaged tissue by externally applying focused acoustic energy on the skin surface of an injured area and has been an effective therapeutic tool in the field of regenerative medicine. It generates a sonic pulse of mechanical energy driving rapid changes in pressure in a 3-dimensional space. It is

characterized by a positive peak within 10 ns, followed by a negative peak up to -10 MPa, with a total life cycle 10 μs [24]. It has been measured to impact tissues of bones, muscle, etc. ESWT has also been used to enhance nerve regeneration in rats [25, 26]. When applied with an energy flux rate of 0.1 mJ/mm^2 at 3 Hz, an increase in myelination, increased expression of the neurotrophic factor, neurtrophin-3, and improved functional recovery were observed [27]. In this regard, we developed a method to apply non-contact mechanical perturbation to the PVDF-TrFE scaffold to mimic the energy of ESWT by using a subwoofer speaker that oscillates at a controlled frequency and power.

To measure the potential generation of the electrospun PVDF-TrFE scaffold, a cantilever set up with two fixed points, adopted from Ico et al. [28], was developed to measure this surface electric charge separation, or voltage output, during mechanical oscillation at a fixed frequency and amplitude. Because water is transmitting environmental noise to the gold, the gold-sputtered electrodes on both sides of the PVDF-TrFE scaffolds were insulated with a flexible hydrophobic polymer, poly(styrene-b-isobutylene-b-stryrene) (SIBS), to prevent water infiltration. SIBS has been used as an encapsulating coating for biomedical applications that require devices to operate in a liquid environment.

To emulate the applied energy of the shockwave system, a subwoofer speaker controlled by a custom LabView problem was utilized to subject the PVDF-TrFE scaffolds to mechanical actuation within the assembled cell culture device. An oscilloscope recorded its potential generation from electric charge separation. A positive to negative

potential peak was recorded. This profile occurs when the subwoofer drives down first, the PVDF-TrFE concaves upwards and produces a negative voltage signal. When the subwoofer returns back to the neutral state, the scaffold bends back to the neutral position, causing the signal to reverse and approach back to zero. As the speaker oscillates passed the neutral axis to its maximum point, the scaffold continues to bend and concave downwards due to the driving force of the media within the chamber, the potential continues towards its maximum positive potential. Finally, when the speaker returns back to the neutral state, the scaffold also returns back to the neutral position, thus the potential is zero again. There is a residual potential peaks due to continuous water movement within the chamber following a speaker oscillation.

The effect of various fiber diameters and thicknesses of electrospun PVDF-TrFE scaffolds were measured for potential generation under a range of strains. When measuring the effects of fiber diameter on potential generation, as expected, as the fiber diameter increases, the voltage output decreases. Fiber diameter is significantly affected by polymer concentration. It becomes more difficult to elongate and stretch a polymer solution with higher polymer concentration due to the high viscosity and stronger macromolecular chain entanglement [29]. Therefore, the β crystal phase content decreases with increasing fiber diameter, ultimately, leading to lower voltage production.

On the other hand, as the fiber mat thickness increased, an increase in voltage output was observed. Due to the capacitive nature of a PVDF nanofiber mat, as the fiber mat thickness increased, there is a greater charge separation, hence a greater output

voltage. However, increasing the mat thickness could also decreased the amount the scaffold could strain, negatively affecting the performance of the piezoelectric scaffold.

Previous studies have shown that cell alignment for greater neurite outgrowth of neural cell types requires a certain minimum fiber size [12, 30]. Neural cell types preferentially grows on larger fiber sizes, which would compromise the performance of the piezoelectric scaffold. Electrospun fiber morphology and scaffold thickness will collectively influence charge separation on the piezoelectric scaffold surface while the fiber diameter is the predominant factor affecting cellular alignment. Therefore, the scaffolding system needs to be optimized to balance the potential generation of PVDF-TrFE electrospun scaffolds with topographical cue to guide cellular alignment.

2.5. Conclusion

In this study, we demonstrated the ability to generate potentials from PVDF-TrFE scaffolds by non-contact mechanical stimulation using the developed cell culture system. We were able to precisely control the potential generation by controlling the fiber diameter and scaffold thickness via the electrospinning technique. This piezoelectric cell culture system will allow us to generate electrical potentials by non-contact mechanical activation to stimulate neural cells for modulating their behaviors.

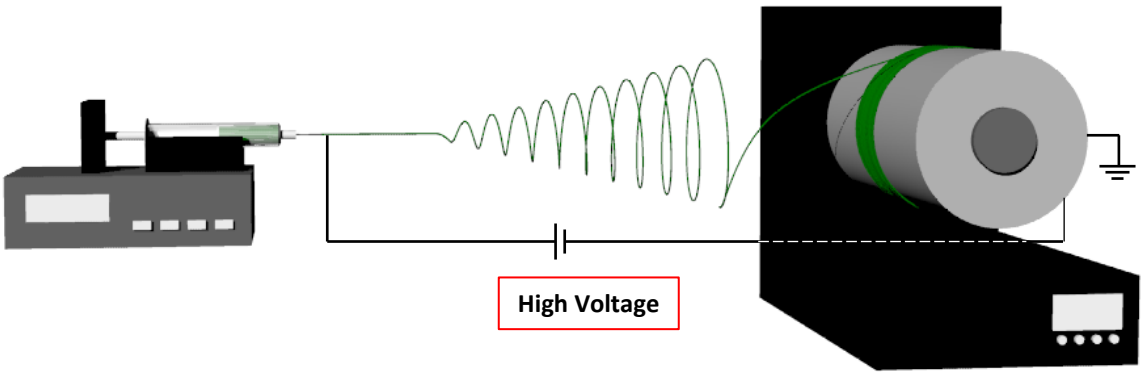

Figure 2.1. Electrospinning using a rotating mandrel. An electric field elongates a polymeric solution onto a high speed rotating mandrel to synthesize an aligned fibrous structure that is ideal for culturing neural cell types.

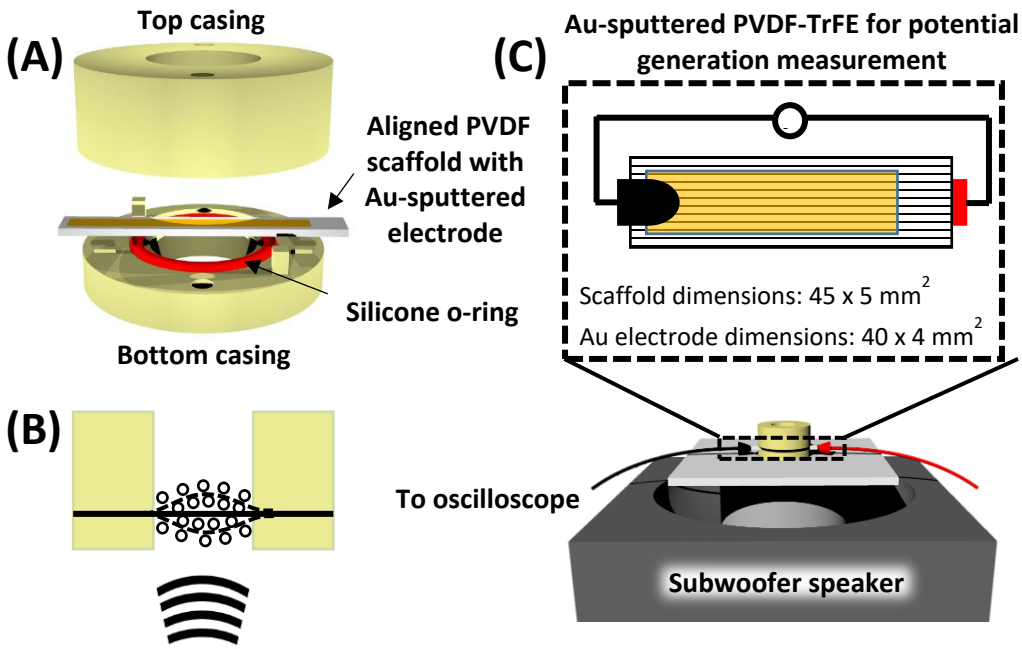

Figure 2.2. Piezoelectric cell culture system. (A) A schematic of the expanded cell culture system. (B) Mechanism for driving PVDF-TrFE nanofibers to produce an electric potential. (C) A schematic of a subwoofer speaker set up for activating PVDF-TrFE scaffolds and measuring the potential generation.

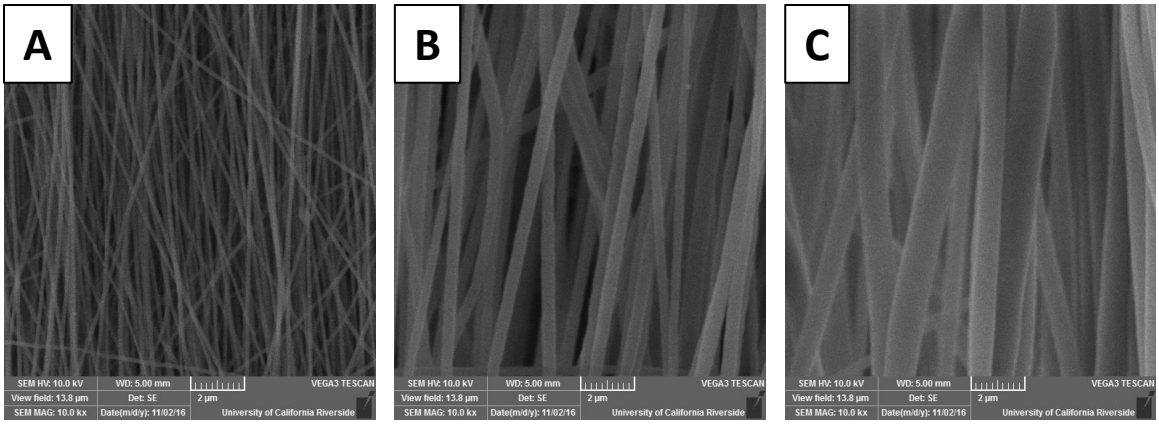

Figure 2.3. Morphological characterization of electrospun PVDF-TrFE aligned nanofibers with various fiber diameters. Representative SEM micrographs of PVDF-TrFE aligned nanofibers from (A) 7% PVDF-TrFE dissolved in DMF/Acetone with PF buffer, (B) 11.5% PVDF-TrFE dissolved in DMF/Acetone with PF buffer, and (C) 16% PVDF-TrFE dissolved in DMF/MEK.

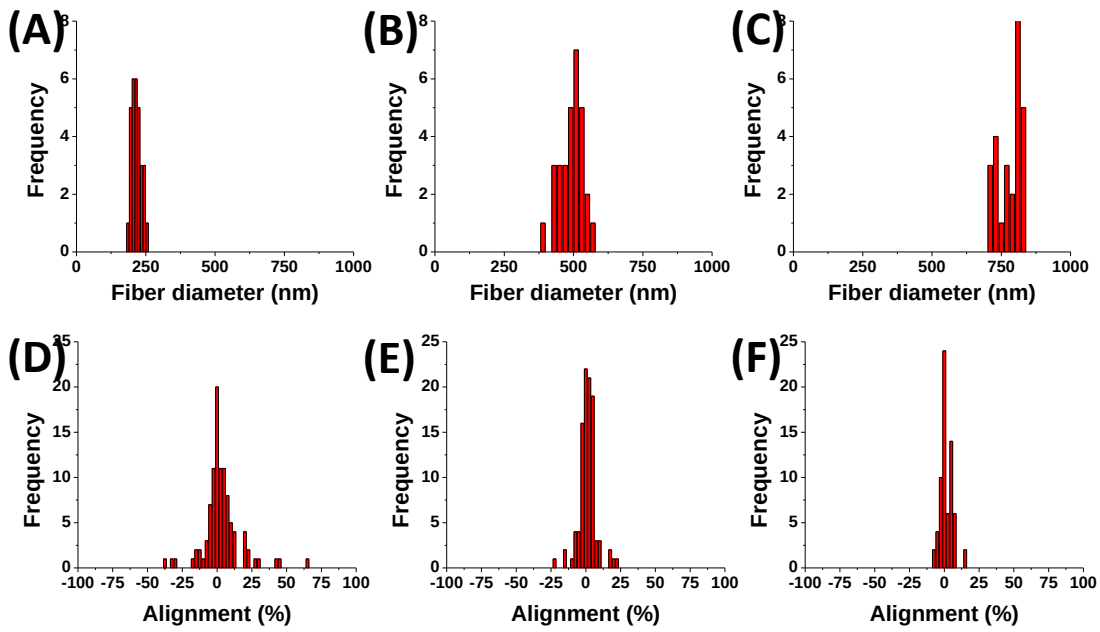

Figure 2.4. Quantitative analysis of electrospun PVDF-TrFE aligned nanofiber morphologies. SEM images of PVDF-TrFE aligned nanofibers were quantified to determine (A – C) average fiber diameters and (D – F) alignment from (A,D) 7% PVDF-TrFE dissolved in DMF/Acetone with PF buffer, (B,E) 11.5% PVDF-TrFE dissolved in DMF/Acetone with PF buffer, and (C,F) 16% PVDF-TrFE dissolved in DMF/MEK.

Solution			
[Polymer] (%)	7	11.5	16
Solvent	DMF/ Acetone/PF	DMF/ Acetone/PF	DMF/MEK
Electrospinning conditions			
Flow rate (mL/hr)	2	6	6
Distance (cm)	10		
Rotating speed (m/s)	47.9		
Environmental conditions			
RH (%)	40		
T (°C)	23		
Resulting fibers			
Fiber diameter (nm)	205 ± 28	498 ± 57	802 ± 17
Alignment (% within 10°)	79	86	93.5
Alignment (% within 20°)	92	94	98.4

Table 2.1. Optimized electrospinning parameters of PVDF-TrFE nanofibrous scaffolds having various fiber diameters and their morphological characterization.

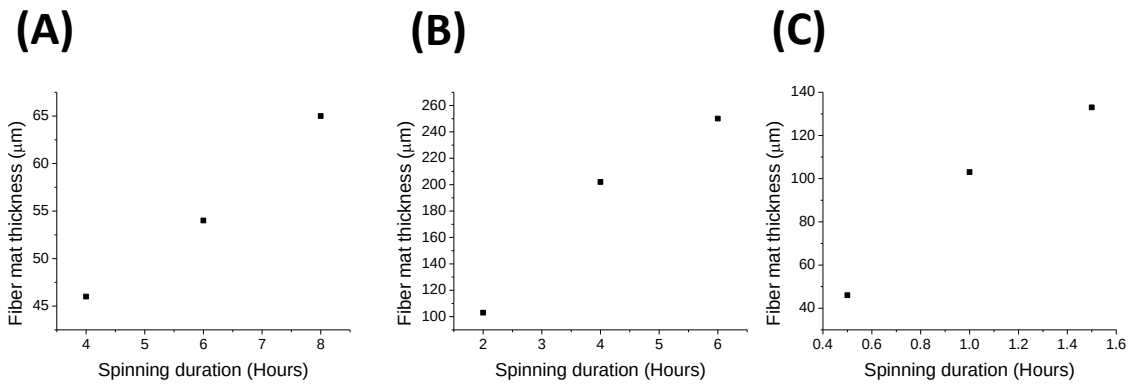

Figure 2.5. Deposition rate of electrospun PVDF-TrFE fiber mat. A relationship between the thickness of fiber mat as a function of electrospinning duration was determined to control fiber mat thickness for (A) 200, (B) 500, and (C) 800 nm fiber diameter scaffolds.

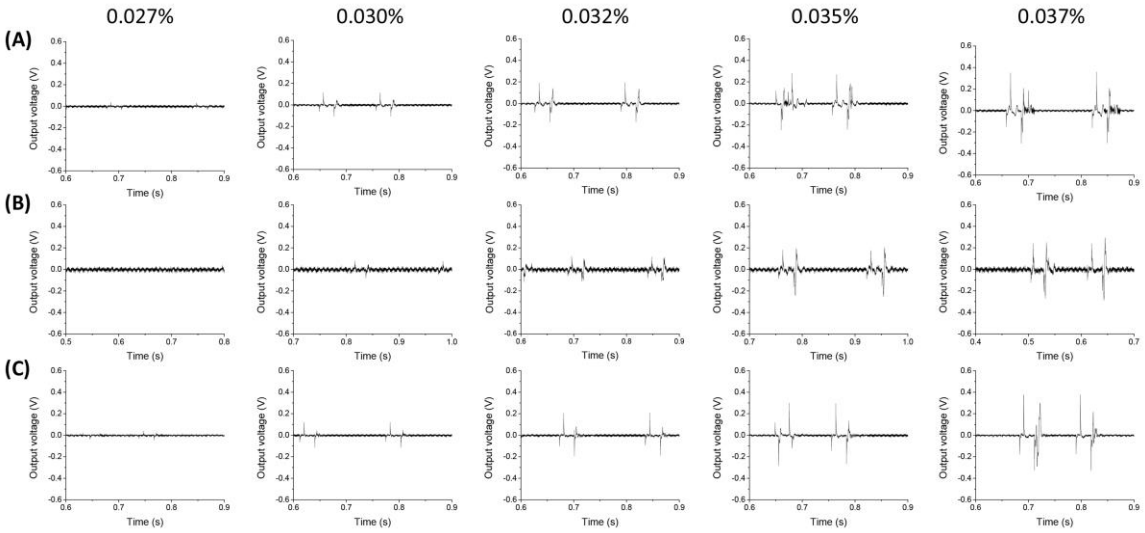

Figure 2.6. Potential generation of PVDF-TrFE nanofibers with an average fiber diameter of 200 nm. Representative plots of the peak-to-peak voltage response to different strains at (A) 46, (B) 54, (C) 65 µm.

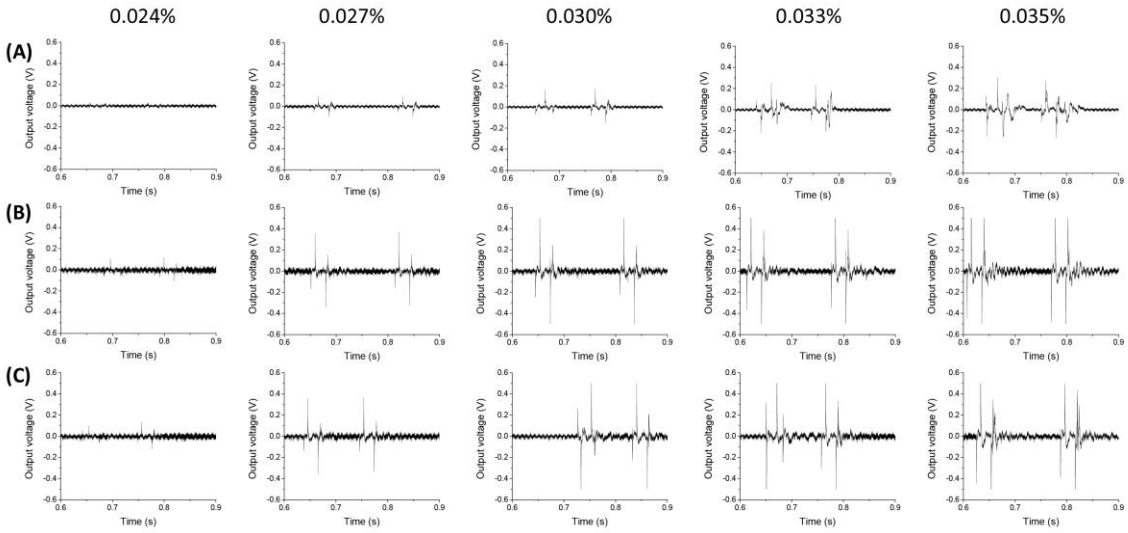

Figure 2.7. Potential generation of PVDF-TrFE nanofibers with an average fiber diameter of 500 nm. Representative plots of the peak-to-peak voltage response to different strains at (A) 48, (B) 103, (C) 202 µm.

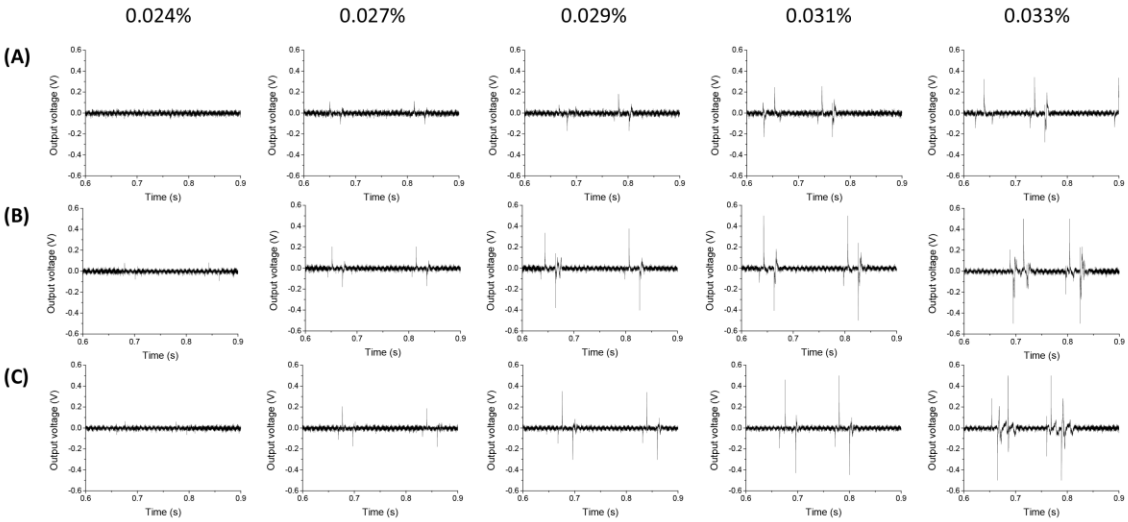

Figure 2.8. Potential generation of PVDF-TrFE nanofibers with an average fiber diameter of 800 nm. Representative plots of the peak-to-peak voltage response to different strains applied at (A) 46, (B) 103, (C) 133 µm.

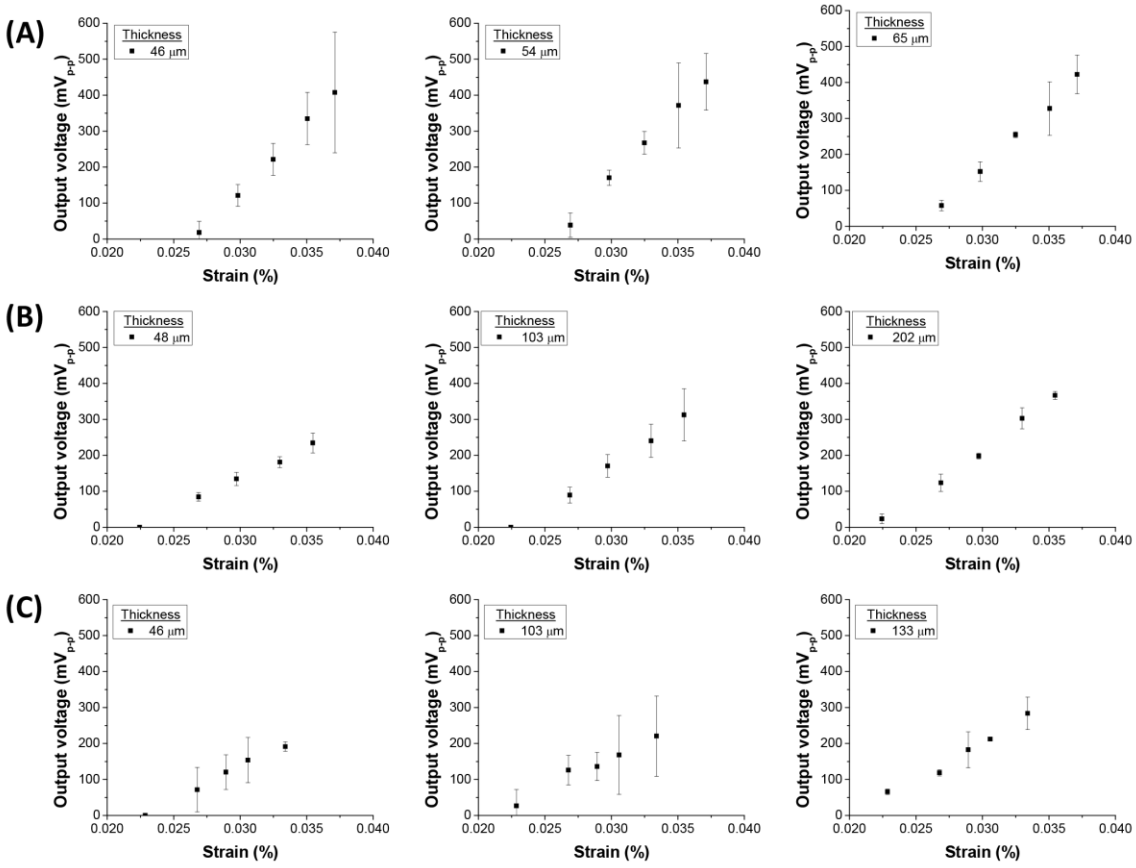

Figure 2.9. Potential generation of PVDF-TrFE nanofibers with various fiber diameters and fiber mat thickness stimulated at different strains. A relationship between the peak-to-peak output voltage as a function of applied strain was determined for (A) 200, (B) 500, and (C) 800 nm fiber diameter scaffolds.

References

1. Uemura, T., et al., *Long-term efficacy and safety outcomes of transplantation of induced pluripotent stem cell-derived neurospheres with bioabsorbable nerve conduits for peripheral nerve regeneration in mice.* Cells Tissues Organs, 2014. **200**(1): p. 78-91.

2. Ikeda, M., et al., *Acceleration of peripheral nerve regeneration using nerve conduits in combination with induced pluripotent stem cell technology and a basic fibroblast growth factor drug delivery system.* Journal of biomedical materials research Part A, 2014. **102**(5): p. 1370-1378.

3. Zhang, H., et al., *Implantation of neural stem cells embedded in hyaluronic acid and collagen composite conduit promotes regeneration in a rabbit facial nerve injury model.* Journal of translational medicine, 2008. **6**(1): p. 67.

4. Hsu, S.h., C.H. Su, and I.M. Chiu, *A novel approach to align adult neural stem cells on micropatterned conduits for peripheral nerve regeneration: a feasibility study.* Artificial Organs, 2009. **33**(1): p. 26-35.

5. Keilhoff, G., et al., *Transdifferentiation of mesenchymal stem cells into Schwann cell-like myelinating cells.* European journal of cell biology, 2006. **85**(1): p. 11-24.

6. Hu, J., et al., *Repair of extended peripheral nerve lesions in rhesus monkeys using acellular allogenic nerve grafts implanted with autologous mesenchymal stem cells.* Experimental neurology, 2007. **204**(2): p. 658-666.

7. Lee, A.C., et al., *Controlled release of nerve growth factor enhances sciatic nerve regeneration.* Experimental neurology, 2003. **184**(1): p. 295-303.

8. Brown, M.C., et al., *Macrophage dependence of peripheral sensory nerve regeneration: possible involvement of nerve growth factor.* Neuron, 1991. **6**(3): p. 359-370.

9. Rich, K.M., et al., *Nerve growth factor enhances regeneration through silicone chambers.* Experimental neurology, 1989. **105**(2): p. 162-170.

10. Lee, Y.-S., G. Collins, and T.L. Arinzeh, *Neurite extension of primary neurons on electrospun piezoelectric scaffolds.* Acta biomaterialia, 2011. **7**(11): p. 3877-3886.

11. Lee, Y.S., et al., *Enhanced noradrenergic axon regeneration into schwann cell-filled PVDF-TrFE conduits after complete spinal cord transection.* Biotechnology and bioengineering, 2017. **114**(2): p. 444-456.

12. Yang, F., et al., *Electrospinning of nano/micro scale poly (L-lactic acid) aligned fibers and their potential in neural tissue engineering.* Biomaterials, 2005. **26**(15): p. 2603-2610.

13. Lannutti, J., et al., *Electrospinning for tissue engineering scaffolds.* Materials Science and Engineering: C, 2007. **27**(3): p. 504-509.

14. Martins, P., et al., *Effect of poling state and morphology of piezoelectric poly (vinylidene fluoride) membranes for skeletal muscle tissue engineering.* Rsc Advances, 2013. **3**(39): p. 17938-17944.

15. Ico, G., et al., *Size-dependent piezoelectric and mechanical properties of electrospun P (VDF-TrFE) nanofibers for enhanced energy harvesting.* Journal of Materials Chemistry A, 2016. **4**(6): p. 2293-2304.

16. Schmidt, C.E., et al., *Stimulation of neurite outgrowth using an electrically conducting polymer.* Proceedings of the National Academy of Sciences, 1997. **94**(17): p. 8948-8953.

17. Richardson, R.T., et al., *The effect of polypyrrole with incorporated neurotrophin-3 on the promotion of neurite outgrowth from auditory neurons.* Biomaterials, 2007. **28**(3): p. 513-523.

18. Fields, R.D., E.A. Neale, and P.G. Nelson, *Effects of patterned electrical activity on neurite outgrowth from mouse sensory neurons.* Journal of Neuroscience, 1990. **10**(9): p. 2950-2964.

19. Wood, M. and R.K. Willits, *Short-duration, DC electrical stimulation increases chick embryo DRG neurite outgrowth.* Bioelectromagnetics, 2006. **27**(4): p. 328-331.

20. Kerns, J., et al., *Electrical stimulation of nerve regeneration in the rat: the early effects evaluated by a vibrating probe and electron microscopy.* Neuroscience, 1991. **40**(1): p. 93-107.

21. Brushart, T.M., et al., *Electrical stimulation promotes motoneuron regeneration without increasing its speed or conditioning the neuron.* Journal of Neuroscience, 2002. **22**(15): p. 6631-6638.

22. Alrashdan, M.S., et al., *Thirty minutes of low intensity electrical stimulation promotes nerve regeneration after sciatic nerve crush injury in a rat model.* Acta Neurologica Belgica, 2010. **110**(2): p. 168-179.

23. Sisken, B., et al., *Stimulation of rat sciatic nerve regeneration with pulsed electromagnetic fields.* Brain research, 1989. **485**(2): p. 309-316.

24. Schuh, C.M., et al., *Extracorporeal shockwave treatment: A novel tool to improve Schwann cell isolation and culture.* Cytotherapy, 2016. **18**(6): p. 760-770.

25. Wang, B., et al., *Low-Intensity Extracorporeal Shock Wave Therapy Enhances Brain-Derived Neurotrophic Factor Expression through PERK/ATF4 Signaling Pathway.* International journal of molecular sciences, 2017. **18**(2): p. 433.

26. Mense, S. and U. Hoheisel, *Shock wave treatment improves nerve regeneration in the rat.* Muscle & Nerve, 2013. **47**(5): p. 702-710.

27. Lee, J.-H. and S.-G. Kim, *Effects of extracorporeal shock wave therapy on functional recovery and neurotrophin-3 expression in the spinal cord after crushed sciatic nerve injury in rats.* Ultrasound in medicine & biology, 2015. **41**(3): p. 790-796.

28. Sunderland, S. and F. Walshe, *Nerves and nerve injuries.* 1968.

29. Shenoy, S.L., et al., *Role of chain entanglements on fiber formation during electrospinning of polymer solutions: good solvent, non-specific polymer–polymer interaction limit.* Polymer, 2005. **46**(10): p. 3372-3384.

30. Wang, H.B., et al., *Varying the diameter of aligned electrospun fibers alters neurite outgrowth and Schwann cell migration.* Acta biomaterialia, 2010. **6**(8): p. 2970-2978.

CHAPTER 3. ELECTRICAL STIMULATION OF NEURONAL CELLS VIA MECHANO-RESPONSIVE PIEZOELECTRIC SCAFFOLDS ENHANCES THEIR FUNCTIONAL GAIN THROUGH NEURITE ELONGATION

Abstract

An estimated 20 million people in the US suffer from some form of peripheral neuropathy, a condition resulting from damage to the peripheral nervous system, by disease or injury. Due to the complex nature of nerve regeneration, full functional recovery is difficult to achieve, especially for large nerve gaps. Therefore, there is an increasing need for strategies to enhance nerve regeneration for full functional recovery. Electrical stimulation has been shown to facilitate the promotion of axon regrowth and induce the secretion of neurotrophic factors from glial cells to further enhance the axon regeneration process. In this study, we demonstrate the use of non-contact electrical stimulation using a biocompatible, piezoelectric polyvinylidene fluoride trifluoroethanol (PVDF-TrFE) by taking advantage of its piezoelectric properties to enhance neurite elongation of the neuronal PC12 cells. Under mechanical/electrical stimulation for 96 hr PC12 cells elongated their neurites up to an average of 100 μm and with 60% of the cell population possessing elongated neurites as compared to 72 μm and 20%, respectively for the statically cultured cells. Of this population of cells, 40% possessed neurites that were 6 to 7 times longer than the nucleus body. These results demonstrate the usage of

piezoelectric materials to their full capacity provides a promising potential for nerve regeneration of severe nerve damage with large gaps.

3.1. Introduction

Despite the advancement of surgical procedures and strategies, complete functional recovery of severe damage to the peripheral nerve, caused by traumatic injury or disease, is rarely achieved due to inherently poor regenerative capabilities of neural system, especially for large nerve gaps [1]. The process of nerve regeneration requires a series of well-orchestrated steps including Wallerian degeneration of axon and re-mapping of nerve connection from the proximal nerve stump into the distal muscle targets. The success of this process is significantly impacted by pre-treatment duration, patient's age, and distance of injury to target tissue. Especially, the size of injured nerve gap is the critical factor, determining the efficacy of nerve regeneration. A large defect gap size of 30 mm or greater typically causes diversion of axon regrowth into inappropriate areas and/or uncontrollable branching which ultimately fails to reinnervate the proper target tissue.

To repair nerve gaps sizes that are 30 mm or larger, the current gold standard in the clinical setting is surgically removing a less used nerve, i.e., the sural nerve, the greater auricular nerve, or the medial antebrachial cutaneous nerve, from the patient and utilizing it as an autologous nerve graft [2]. Because it is acquired from the patient, it has no immune-responsive and possibility of rejection; it provides the biological cues ideal for cells to infiltrate the injury site, proliferate, and perform axon regeneration; and it is structurally stable and can withstand physiological stress. However, sacrificing the donor nerves typically lead to donor site morbidity, including loss of sensory function, prolonged

operative and recovery times, and the invasiveness of multiple surgeries. The autologous nerve graft also poses other limitations, such as differences in nerve trunk size and limited length. In this regard, non-biological nerve conduits have been developed to guide nerve regeneration, but current clinically-approved natural and synthetic conduits are typically biologically inert and cannot fully repair transected nerves to regain full functionality.

Recently, electrical stimulation has gained attention as a potent regenerative signal to modulate electro-responsiveness of neural cells for the auto-regulation of neurotropic factors to enhance nerve regeneration [3-5]. Specifically, studies demonstrated that bioelectric fields that induce local surface electrical charges, enhance nerve regeneration by inducing the secretion of various growth factors from neural cells to promote nerve fiber outgrowth [6-8]. In *in vitro* studies, electrical stimulation has shown to excite neurons to upregulate the release of several neurotrophic factors, such as brain-derived nerve factor (BDNF), NT4/5, and trkB, for nerve regeneration [4, 9]. It has also shown to stimulate ion flow in the plasma membrane of Schwann cells to induce the production of neurotrophins, nerve growth factor (NGF) and BDNF [10, 11]. Despite its promising potential for stimulating nerve regrowth, the application of electrostimulation has been limited in clinical settings due to its invasive nature and small effective area to apply electrical charges.

In this regard, piezoelectric materials provide an effective modality for non-contact electrical neuromodulation. By the direct piezoelectric effect, a mechanical strain on the electroactive materials induces electrical charge separation on the surface [12].

There were several attempts to utilize biocompatible poly(vinylidene fluoride) (PVDF) or its derivatives including P(VDF-trifluoroethanol) (PVDF-TrFE), an organic piezoelectric polymer, for nerve regeneration *in vitro* as well as *in vivo.* PVDF has been shown to enhance neurite outgrowth of neuronal cells *in vitro* [13]. *In vivo*, implanted PVDF-TrFE conduits demonstrated the ability to bridge short nerve gaps to regain partial functionality*[14]*. Although those studies showed some favorable phenomenological observations from the use of PVDF-TrFE, a lack of systematic piezoelectric characterization and its utilization for the material's design limited the realization of its full potential.

In this study, PVDF-TrFE nanofibrous scaffolds were synthesized by electrospinning to determine their potential for nerve regeneration. The optimization of piezoelectric scaffolds such as fiber size, scaffold thickness, and the magnitude of mechanical perturbation for piezoelectric activation was systematically approached to maximize the regenerative responses of a neuronal cell line. We demonstrated the capability of non-contact mechanical/electrical stimulation on neuronal cells cultured on electrospun PVDF-TrFE scaffolds to induce nerve regeneration via neurite elongation.

3.2. Materials and Methods

3.2.1. Synthesis and morphological characterization of PVDF-TrFE nanofibrous scaffolds

PVDF-TrFE (Solvay, Belgium) was dissolved at various concentrations in different solvent systems to produce a range of different electrospun fiber diameters, as described

in Chapter 2. Briefly, a 16 wt.% PVDF-TrFE (70:30 mol%) was dissolved in a 60/40 volume ratio of *N*,*N*-dimethylformamide (DMF, Sigma Aldrich, St. Louis, MO) to methyl ethyl ketone (MEK, Sigma Aldrich) solvent system. 11.5 wt.% and 7 wt.% PVDF-TrFE were dissolved in a 60/40 volume ratio of DMF to acetone solvent system, with the addition of 1 wt.% pyridinium formate (PF) buffer (Sigma Aldrich). The solutions were magnetically stirred at 1200 rpm for 3 hr at room temperature. The PVDF-TrFE solutions were individually electrospun using a grounded rotating mandrel to produce aligned fibers. The thickness of the fiber mat was controlled by adjusting the deposition time. A comprehensive table including the electrospinning parameters can be found in **Table 2.2**. To further enhance the piezoelectric properties of PVDF-TrFE, the electrospun fiber mats were subjected to annealing at 90 °C for 24 hr. The fiber morphology, diameter and alignment were characterized using scanning electron microscopy (SEM, Vega3, Tescan, Pleasanton, CA). The fibers were sputter-coated with gold to visualize under SEM. Using the ImageJ software, at least 100 individual fibers were assessed to determine the average fiber diameter and alignment.

3.2.2. Cell culture chamber for mechanical/electrical stimulation

A piezoelectric cell culture system was fabricated to apply non-contact mechanical/electrical stimulation to the nanofibrous PVDF-TrFE scaffold/cell constructs by a vertical actuation stage as described in detail in Chapter 2 (**Figure 3.1**). The chamber was designed to fit into a standard 6-well tissue culture plate. Briefly, the top and bottom

casings were 3D-printed with acrylonitrile butadiene styrene (ABS). When assembled, the PVDF scaffold is securely held by the silicone o-rings. Stainless steel screws hold the two casings together. The center cavity provides an area to hold media while allowing free deflection of the cell/scaffold construct under vertical actuation. The exposed area of the cell/ scaffold construct has the dimensions of 15 mm x 5 mm.

3.2.3. Piezoelectric characterization of electrospun nanofibers

To quantify the potential generation of the PVDF-TrFE scaffolds in the actuation system, acellular scaffolds were subjected to mechanical/electrical stimulation inside the cell culture system. PVDF-TrFE scaffolds were cut to the dimensions of 45 mm by 5 mm with various thicknesses. Gold electrodes with the dimension 40 mm by 4 mm were sputtered on both sides of the scaffolds. A hydrophobic poly(styrene-b-isobutylene-b-stryrene) (SIBS, Sibstar, Kaneka, Pasadena, TX) coating was spray coated on top of gold sputtered surfaces to prevent an electrical short circuit. The processed scaffold was assembled into the cell culture chamber and 2 mL of DI water was added. The chamber was placed on the vertical actuator and various magnitudes of strains were applied at 3 Hz while simultaneously measuring resultant potential generation by an oscilloscope (Pico Technologies, St. Neots, UK). The peak to peak output voltage was determined for 200, 500, and 800 nm fiber diameter at various scaffold thicknesses. The magnitude of applied strain was determined from images captured during the deflection of scaffolds under various magnitudes of actuation.

3.2.4. PC12 cell culture

PC12 cells, a rat adrenal pheochromocytoma cell line, were purchased from ATCC (Manassas, VA). The cells were maintained on tissue culture plates coated with type I collagen from rat tail (Sigma Aldrich) in F12K medium (ATCC), supplemented with 15% horse serum (Sigma Aldrich), 2.5% fetal bovine serum (FBS, VWR, Radnor, NJ), and 1% antimycotic/antibiotic solution (Corning, Corning, NY). To pre-differentiate the PC12 cells, the cells were detached from the surface by a cell scraper. To disintegrate cell clumps, the cells were passed through a 22 G needle several times. The cells were then seeded onto tissue culture plates at a density of 30,000 cells/cm^2 in starvation differentiation media (F12K medium supplemented with 1% FBS and 1% antimycotic/antibiotic solution). The cells were allowed to adhere for 6 hr, followed by the supplementation of the media with 50 ng/mL nerve growth factor (2.5S) (Corning). The cells were allowed to pre-differentiate for 48 hr before detaching by mechanical scraping for subsequent cell seeding on the scaffolds.

3.2.5. The effects of scaffold morphological and electrical stimulation on cellular behaviors

To determine the effects of PVDF-TrFE fiber diameter on neurite elongation, pre-differentiated PC12 cells were separately seeded onto PVDF-TrFE scaffolds with fiber diameters of 200, 500, or 800 nm at a density of 40,000 cells/cm^2. The cells were cultured for 96 hours, before fixation in 4% paraformaldehyde (PFA) for the morphological analysis as described below.

To determine the effects of the various magnitudes of applied potential regimen, pre-differentiated PC12 cells on the PVDF-TrFE scaffolds having an average fiber diameter of 500 nm were electrically stimulated without mechanical perturbation. The cell/scaffold construct was placed on a conductive surface to apply an electric field with respect to the thickness of the construct (**Figure 3.1 (A)**). Gold-coated polystyrene were cut out to the dimensions of 15 mm x 5 mm and adhered to a tissue culture plate. A PVDF-TrFE scaffold with the same dimensions was glued to the surface of the polystyrene. A hole was drilled through the tissue culture plate to expose the conductive polystyrene to make electrical connection to a function generator. A grounded gold-coated coverslip was placed 5 mm above the gold-coated polystyrene. A function generator was utilized to control the electrical impulses applied to the conductive surface at 100, 200, and 400 mV_{p-p}, with its shape similar to potential peaks generated from piezoelectrically actuated PVDF-TrFE scaffolds. The cell culture plates for this electrical stimulation were sterilized by ethanol and UV treatment of 30 min and 1 hr, respectively. The pre-differentiated cells by NGF treatment for 48 hr were detached and reseeded onto the PVDF-TrFE scaffolds at the density of 40,000 cells/cm^2. The cells were allowed to attach for 24 hr prior to being subjected to electrical stimulation. The PC12 cells were either electrically stimulated once for 2 hr, followed by 72 hr of static culture or daily stimulated for 2 hr for three days. For both conditions, the cells were cultured in a total duration of 96 hrs before fixation in 4% paraformaldehyde (PFA).

3.2.6. The effects of mechanical/electrical stimulation on cellular behaviors

Once the optimal scaffold fiber diameter and applied potential regimen were determined as described above, the differentiated PC12 cells were subjected to mechanical/electrical stimulation on PVDF-TrFE by using the vertical actuation stage. The scaffolds with the dimensions of 45 mm x 5 mm were treated with 20% FBS for 12 hr before cell seeding to enhance the adhesion of PC12 cells to the scaffolds. A hydrophobic SIBS coating was applied to leave an area of 10 mm x 5 mm to confine cell culture space. The scaffolds were assembled into the sterile chamber individually and the pre-differentiated cells were seeded onto the scaffolds at a density of 40,000 cells/cm^2 . The seeded cells were allowed to attach for 2 hrs before filling up the chamber with additional media. The cells were cultured for 24 hrs before subjecting them to mechanical/electrical stimulation. Similarly to the method used for determining potential generation of acellular PVDF-TrFE scaffolds, the cell-seeded scaffold was actuated by the vertical actuation stage to produce the optimum potential determined in the electrical stimulation study as previously described. The cell/scaffold constructs were either stimulated once for 2 hrs followed by 72 hrs of static culture or daily stimulated for 2 hrs for three days. For both conditions, the cells were cultured in a total duration of 96 hrs before fixation in 4% PFA.

3.2.8. Morphological characterization of PC12 cells

To visualize the elongation of neurites, the fixed cells were immune-stained with beta III-tubulin (Thermo Fisher), and counter-stained the nucleus with 4',6-Diamidino-2-Phenylindole (DAPI, Vector Labs, Burlingame, CA) nucleus and actin with Alexa Fluor 488-Phalloidin (Invitrogen, Carlsbad, CA). By imaging analysis using the ImageJ, neurite length, percentage of cell population bearing neurites, and the percentage of neurite-bearing cells possessing neurite lengths, within a certain range, greater than the nuclei length were quantitatively determined for both electrical and mechanical/electrical stimulation studies.

3.2.9. Statistical analysis

Statistical analysis was performed with at least three biologically independent samples, and represented as an average ± standard deviation (SD) or standard error of mean (SEM) as indicated. The data were subjected to ANOVA with Tukey's post-hoc test using the SPSS software (IBM) to determine statistical significance ($p < 0.05$).

3.3. Results

3.3.1. Effects of nanofibrous piezoelectric PVDF-TrFE on neurite elongation

The fiber diameter of electrospun scaffolds has been shown to significantly affect the alignment of neuronal cells, thus the neurite elongation (ref). In addition, we have recently shown that the fiber diameter of electrospun PVDF determines the piezoelectric

performance of the scaffolds as smaller fiber diameters exponentially enhance the piezoelectric constant (ref). To optimize fiber diameter that achieves a balance between high piezoelectric properties while promoting the elongation of neurites, PVDF was electrospun to produce three distinctly different fiber diameters. Various electrospinning conditions including solution properties (solvent system, polymer concentration, additives), processing parameters (solution flow rate, spinneret-to-collector distance), and environmental conditions (temperature and humidity) were optimized to reproducibly produce an average fiber diameter of 200, 500, or 800 nm (**Figure 3.2 (A)**). These scaffolds were morphologically characterized for their fiber diameter and alignment using SEM (**Figure 3.2 (A)**). Larger fiber diameter enhanced alignment, but all scaffolds exhibited relatively high fiber alignment within 20° of the neutral axis (**Figure 3.2 (B)**).

The fiber size-dependent piezoelectric performance of the electrospun PVDF scaffolds was determined by subjecting the samples to the vertical actuator at 3 Hz (**Figure 3.3**). The mechanical perturbation of the scaffolds generated electric potentials exhibiting the characteristic piezoelectric double peaks during each oscillation (up and down translational motion of the chamber). As expected from our previous study demonstrating the fiber size-dependency of piezoelectric constants in electrospun PVDF-TrFE, the smallest fiber diameter scaffolds generated the highest output voltage. Furthermore, the potential generation increased as the scaffold thickness increased for all fiber sizes. These results provided a means to tune the morphological properties of the

scaffolds (i.e., fiber diameter and scaffold thickness) accordingly for designed piezoelectric performance in the subsequent experiments.

We next examined the effects of fiber diameter on neuronal cell behaviors as the direction of neurite elongation is guided by the combination of fiber diameter and alignment (**Figure 3.4**). PC12 cells exhibited greater directionality on the scaffolds with larger fiber diameters that likely prevented spreading of the cells across adjacent fibers. The greater alignment of the cells on larger fiber diameters appears to positively affect neurite formation and its elongation. The average neurite length of the cells cultured on scaffolds with 800 nm fiber diameter was approximately 81 μm. The average number of neurites per cells was also greater in the cells on the scaffolds with larger fiber diameters (**Figure 3.4B**).The larger fiber diameter also induced a greater number of the cells to possess neurites longer than 4 times of the nucleus size (**Figure 3.4D**). To balance the better piezoelectric performance of the smaller fiber and the greater neuronal cell behaviors on the larger fiber, the scaffolds with an average fiber diameter of 500 nm were utilized for the remainder of the experiments.

3.3.2. Effects of electrical stimulation on neurite elongation

To determine the optimal electric potential to promote neurite elongation in PC12 cells, the cells were subjected to different magnitudes of electric fields (**Figure 3.5 (A)**). To take into account the contribution from scaffold morphology on cellular behaviors, the cells were cultured on electrospun PVDF with an average fiber diameter of 500 nm and

during electrical stimulation. A peak-to-peak electric potential of 100, 200, or 400 mV at 3 Hz, with a wave form similar to piezoelectric potential generation shown in Figure 3, was applied to the cells. Cellular responses were quantified by imaging analysis (**Figure 3.5**). As the magnitude of electrical stimulation increased from 0 (control) to 200 mV_{p-p}, PC12 cells increased neurite formation and elongation. However, a high magnitude of 400 mV_{p-p} resulted in a significant decline neurite length due to cell death. The multi-day application of both 100 and 200 mV_{p-p}, induced a greater percentage of PC12 cells that possessed neurites as well as promoted greater neurite elongation. Lastly, multi-day stimulation induced the greatest number of cells that possess neurites in the range of 6-10 times longer than the nucleus body.

3.3.3. Effects of mechanical/electrical stimulation on neurite elongation

From the previous results, the thickness of PVDF-TrFE scaffold with an average fiber diameter of 500 nm was optimized to produce 200 mV_{p-p} under mechanical perturbation. Pre-differentiated PC12 cells were seeded on these scaffolds and stabilized for 24 hr before the mechanical/electrical stimulation in the cell culture system. Based on the electrical stimulation study, a multi-day mechanical/electrical stimulation regimen was selected and carried out for 96 hr. Cellular responses were quantified by imaging analysis (**Figure 3.6**). Both mechanical/electrical stimulation conditions enhanced neurite formation and elongation as compared to static culture. At the end of the culture duration, mechanical/electrical stimulation condition induced the greatest number of

neurite-formed cells with its average length greater 6 to 8 times greater than their nucleus body. These results demonstrate that electrical activity from the PVDF-TrFE induced neurite formation and promoted elongation parallel to the direction of the fiber mat.

3.4. Discussion

Electrical stimulation has been shown to facilitate nerve regeneration by enhancing the secretion of neurotrophic factors from glial cells to support axon regeneration and/or directly promoting neurite elongation [10, 15, 16]. Several *in vivo* studies demonstrated the efficacy of electrical stimulation promoting nerve outgrowth in rat models of nerve injury [17-19]. The first human clinical trial showed a promising potential of therapeutic electrical stimulation, where improved post-surgical outcomes were achieved by localized low frequency of electrical stimulation on patients with their median nerve compressed in the carpal tunnel causing loss of functional nerve-muscle contracts [20]. Despite these positive outcomes, the application of electrical stimulation in the clinical setting is limited by several factors; its invasive nature requires the implantation of exposed electrodes. Furthermore, the electrode approach can activate neuron(s) only in direct contact with or close proximity to the electrodes, resulting in a small localized effective area. To address these issues, various methodologies have been developed to globally deliver electrical stimulation to a severed nerve using a continuous graft connecting the nerve gap.

Conductive nerve guidance conduits provide an opportunity to implement electrical stimulation as a means to guide the regeneration and regrowth of axons while reducing the infiltration of fibrous tissue. Several in vitro studies demonstrated enhanced neurite elongation of neuronal cells under electrical stimulation via conductive polymer scaffolds [6, 7, 21, 22]. In vivo, Xu et al. recently showed enhanced functionality of regenerated nerve using a PPy-PDLLA conduit in a rat sciatic nerve transection model, where a higher density of thick myelin sheaths of the cells in the PPy-PDLLA conduit was observed as compared to an autograft [23]. These studies collectively suggest a great potential of electrical stimulation to drive nerve regeneration, but it requires the use of implanted electrodes for clinical applications.

In this regard, piezoelectric materials provide a means to non-invasively induce electrical potentials. Especially, PVDF and its derivatives including PVDF-TrFE have been utilized for such applications due to their excellent biocompatibility and relatively high piezoelectricity for polymers. Early evidence of the implantation of poled PVDF conduits compared to unpoled conduits demonstration the feasibility of piezoelectric materials to enhance partial axon regeneration with myelination [24]. Recently, Lee et al. exploited the enhanced piezoelectricity of PVDF-TrFE scaffolds synthesized by electrospinning to accelerate neurite outgrowth of dorsal root ganglion neurons or promote neural differentiation of human neural stem/progenitor cells [13, 25]. However, these studies were likely unable to utilize the true potential of piezoelectricity as it requires dynamic straining of the materials to generate electrical potential. Although they attributed the

enhancement in cellular behaviors to piezoelectric responses of the PVDF fibers developed by cell exerting forces, they would be likely due to surface charges of the fibers [26].

In contrast, we optimized piezoelectric properties of PVDF-TrFE with a systematic approach and thorough material characterization, to generate the appropriate electric potential of 200 mV_{p-p} to stimulate neuronal cells by non-contact mechanical perturbation of electrospun PVDF-TrFE scaffolds. A recent study showed the novel use of aligned conductive polymer PLLA-graphene oxide scaffolds to induce PC12 cell neurite length of 90 μm in 6 days. With our optimized PVDF-TrFE scaffolds, we demonstrated that PC12 cells exposed to multi-day mechanical/electrical stimulation exhibited significantly enhanced neurite formation of 100 μm in merely three days of stimulation and 60% of the population possessed neurites. This signifies the potency of external piezoelectric stimulus for nerve regeneration. Furthermore, considering the relatively porous structure of electrospun PVDF-TrFE scaffolds that allow for selective diffusion of macromolecules and neurotrophic factors, our results demonstrate the promising potential of PVDF-TrFE to enhance nerve regeneration.

3.5. Conclusion

In the present study, we demonstrated that mechanical/electrical stimulation was effective in enhancing neuronal cell elongation. Under multi-day application of mechanical/electrical stimulation for 96 hr produced an average neurite length of

approximately 100 μm with 60% of the cell population possessing elongated neurites as compared to 72 μm and 20%, respectively for the statically cultured cells. Of this population of cells, 40% possessed neurites that were 6 to 7 times longer than the nucleus body. These results exemplify the potential of utilizing non-contact electrical stimulation induced by PVDF-TrFE for enhancing neuronal activities for the application of nerve regeneration.

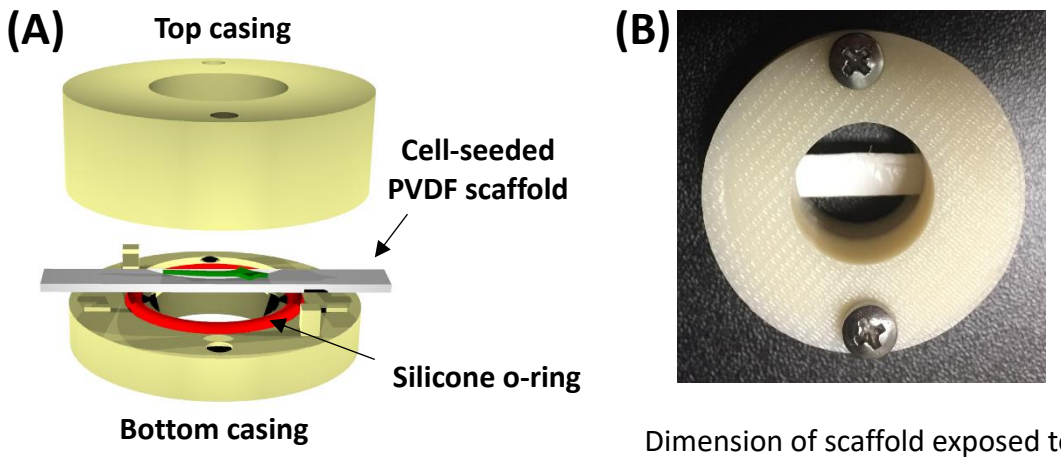

Figure 3.1. Piezoelectric cell culture system. (A) A schematic of the expanded cell culture system. (B) A photograph of an assembled cell culture device with a PVDF-TrFE aligned scaffold.

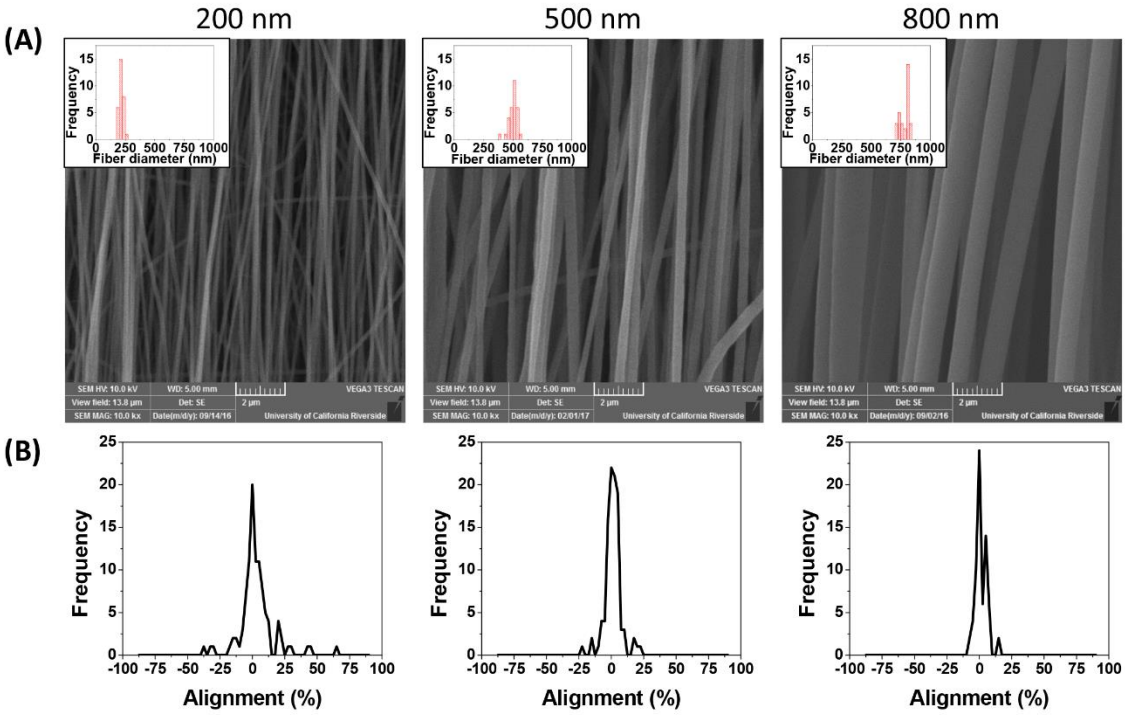

Figure 3.2. Morphological characterization of electrospun PVDF-TrFE aligned nanofibers. (A) SEM images of PVDF-TrFE aligned nanofibers with various average fiber diameters (inset: fiber diameter histogram). (B) Fiber alignment histograms of PVDF-TrFE aligned nanofibers with various fiber diameter.

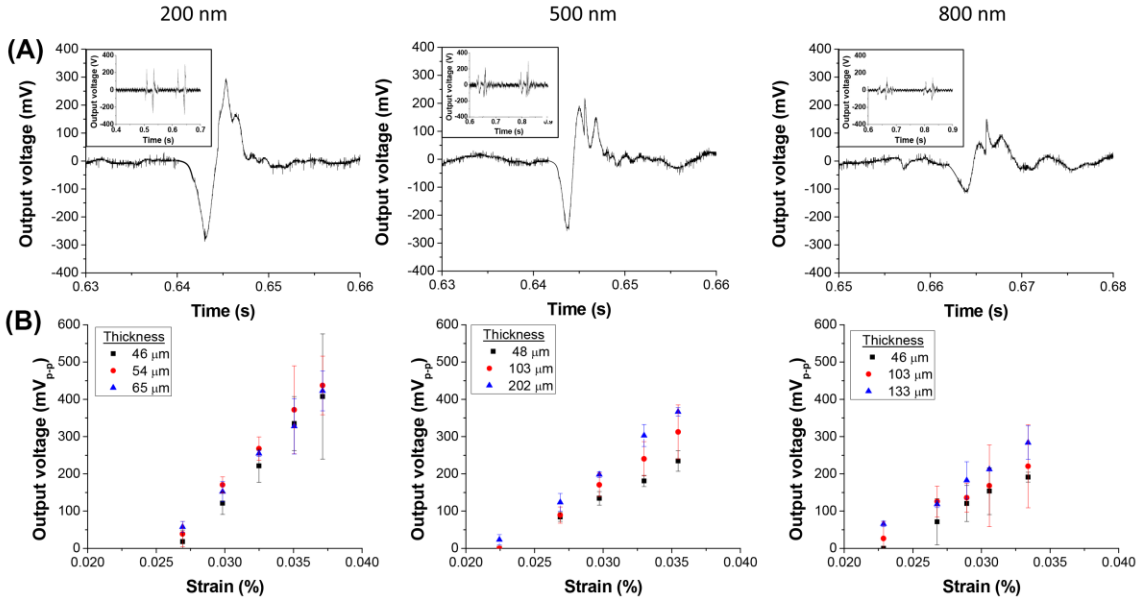

Figure 3.3. Piezoelectric characterization of PVDF-TrFE scaffolds having various fiber diameters and scaffold thicknesses. (A) The characteristic voltage response of PVDF-TrFE nanofibers with fiber diameters of 200, 500, and 800 nm and a fiber mat thickness of ~50 μm at the strain values of: 200 nm = 0.037%, 500 nm = 0.035%, 800 nm = 0.033%. The inset represents the recording of several peaks. (B) The relationship between the applied strain and output voltage when subjected to mechanical perturbation.

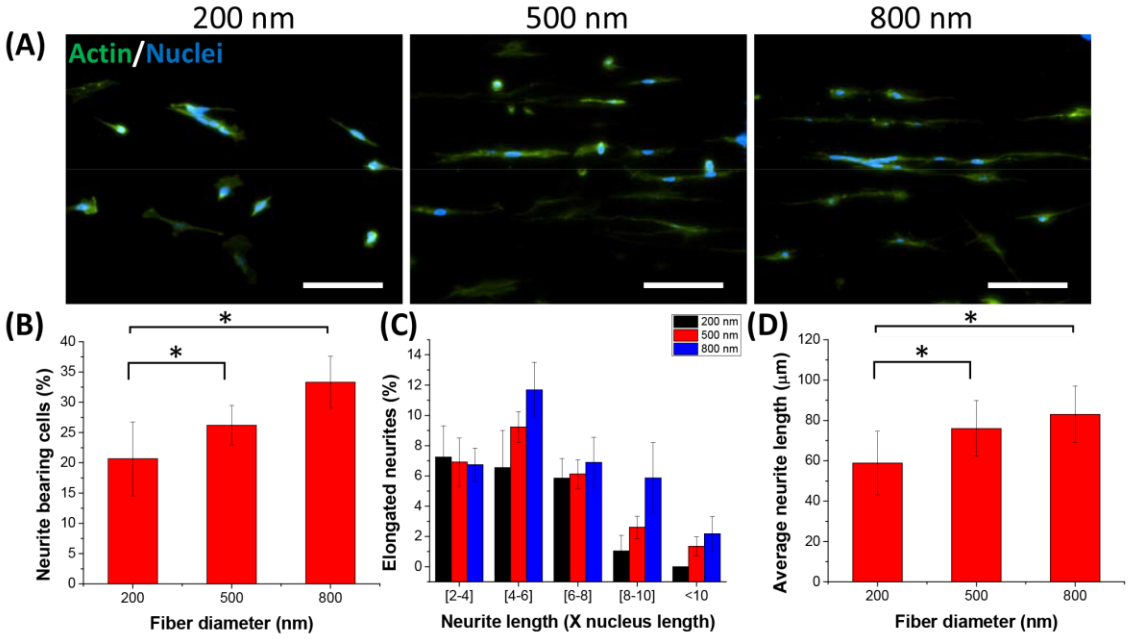

Figure 3.4. Effects of different fiber diameter on neurite formation and elongation. (A) Representative immunofluorescence images showing actin morphology of PC12 cells cultured on 200, 500, and 800 nm fiber diameter. Quantification of (C) the percentage of cell population bearing neurites, (D) the percentage of neurite-bearing cells possessing neurite lengths, within a certain range, greater than the nuclei length, and (E) the average neurite length. (Scale bar = 100 μm)

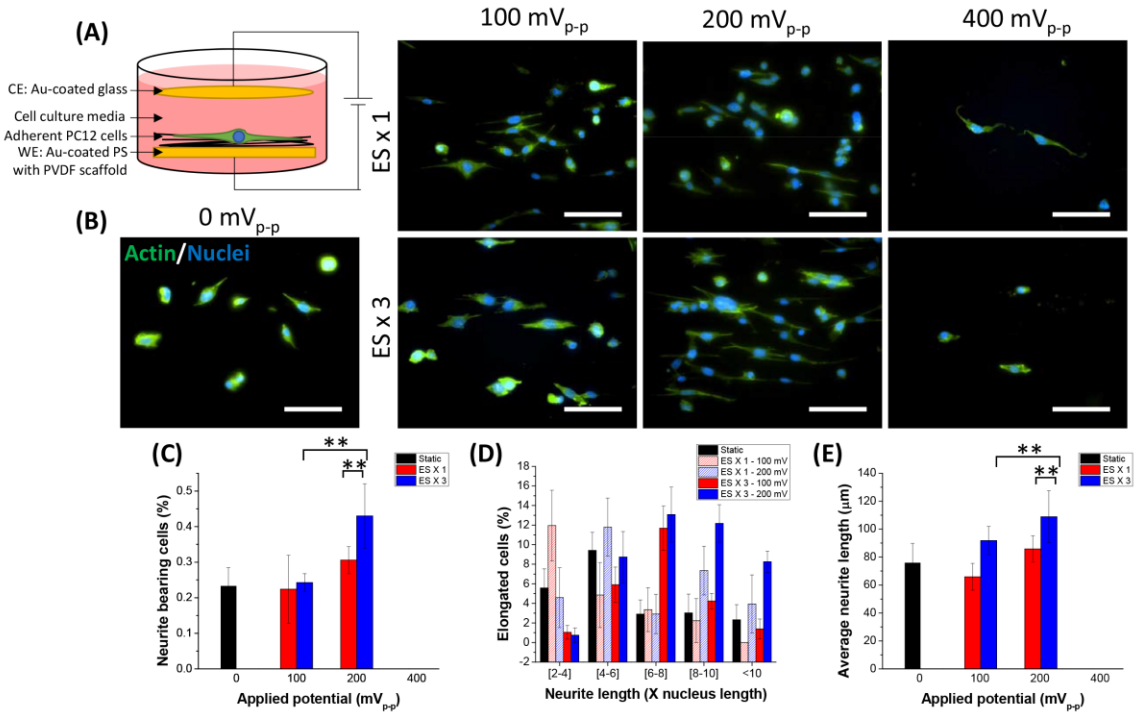

Figure 3.5. Effect of electrical stimulation on neurite formation and elongation. (A) A schematic of the electrical stimulation set up. (B) Representative immunofluorescence images showing actin morphology of PC12 cells subjected to a single or multi-day application of 100, 200, and 400 mV_{p-p}. Quantification of (C) the percentage of cell population bearing neurites, (D) the percentage of neurite-bearing cells possessing neurite lengths, within a certain range, greater than the nuclei length, and (E) the average neurite length. (Scale bar = 100 µm)

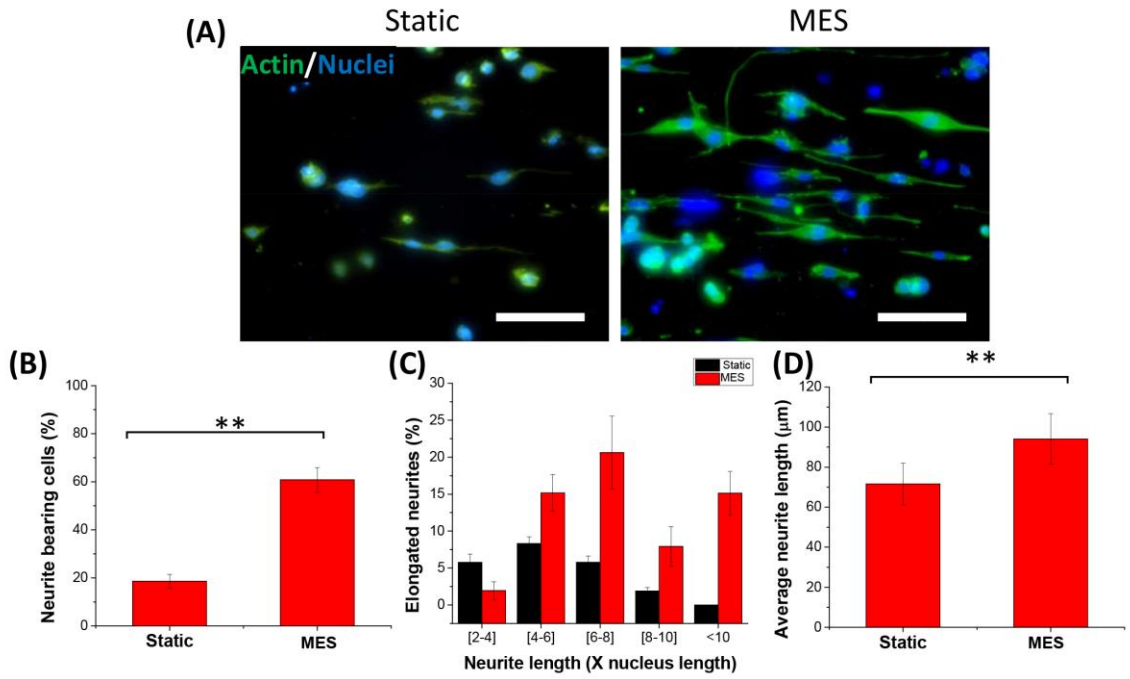

Figure 3.6. Effects of mechanical/electrical stimulation on neurite formation and elongation. (A) Representative immunofluorescence images showing actin morphology of PC12 cells subjected to multi-day mechanical/electrical stimulation and static. Quantification of (C) the percentage of cell population bearing neurites, (D) the percentage of neurite-bearing cells possessing neurite lengths, within a certain range, greater than the nuclei length, and (E) the average neurite length. (Scale bar = 100 μm)

References

1. Schmidt, C.E. and J.B. Leach, *Neural tissue engineering: strategies for repair and regeneration.* Annual review of biomedical engineering, 2003. **5**(1): p. 293-347.

2. Millesi, H., *Bridging defects: autologous nerve grafts.* How to improve the results of peripheral nerve surgery, 2007: p. 37-38.

3. Shepherd, R.K., A. Coco, and S.B. Epp, *Neurotrophins and electrical stimulation for protection and repair of spiral ganglion neurons following sensorineural hearing loss.* Hearing research, 2008. **242**(1): p. 100-109.

4. Gärtner, A. and V. Staiger, *Neurotrophin secretion from hippocampal neurons evoked by long-term-potentiation-inducing electrical stimulation patterns.* Proceedings of the National Academy of Sciences, 2002. **99**(9): p. 6386-6391.

5. English, A.W., et al., *Electrical stimulation promotes peripheral axon regeneration by enhanced neuronal neurotrophin signaling.* Developmental neurobiology, 2007. **67**(2): p. 158-172.

6. Schmidt, C.E., et al., *Stimulation of neurite outgrowth using an electrically conducting polymer.* Proceedings of the National Academy of Sciences, 1997. **94**(17): p. 8948-8953.

7. Zhang, Z., et al., *Electrically conductive biodegradable polymer composite for nerve regeneration: electricity-stimulated neurite outgrowth and axon regeneration.* Artificial Organs, 2007. **31**(1): p. 13-22.

8. Thompson, B.C., et al., *Conducting polymers, dual neurotrophins and pulsed electrical stimulation—dramatic effects on neurite outgrowth.* Journal of Controlled Release, 2010. **141**(2): p. 161-167.

9. Nagappan, G. and B. Lu, *Activity-dependent modulation of the BDNF receptor TrkB: mechanisms and implications.* Trends in neurosciences, 2005. **28**(9): p. 464-471.

10. Huang, J., et al., *Electrical stimulation induces calcium-dependent release of NGF from cultured Schwann cells.* Glia, 2010. **58**(5): p. 622-631.

11. Koppes, A.N., et al., *Electrical stimulation of Schwann cells promotes sustained increases in neurite outgrowth.* Tissue Engineering Part A, 2013. **20**(3-4): p. 494-506.

12. Vijaya, M., *Piezoelectric materials and devices: applications in engineering and medical sciences*2012: CRC Press.

13. Lee, Y.-S., G. Collins, and T.L. Arinzeh, *Neurite extension of primary neurons on electrospun piezoelectric scaffolds.* Acta biomaterialia, 2011. **7**(11): p. 3877-3886.

14. Fine, E.G., et al., *Improved nerve regeneration through piezoelectric vinylidenefluoride-trifluoroethylene copolymer guidance channels.* Biomaterials, 1991. **12**(8): p. 775-780.

15. You, S., et al., *The expression of the low affinity nerve growth factor receptor in long-term denervated Schwann cells.* Glia, 1997. **20**(2): p. 87-100.

16. Fields, R.D., E.A. Neale, and P.G. Nelson, *Effects of patterned electrical activity on neurite outgrowth from mouse sensory neurons.* Journal of Neuroscience, 1990. **10**(9): p. 2950-2964.

17. Kadekaro, M., A.M. Crane, and L. Sokoloff, *Differential effects of electrical stimulation of sciatic nerve on metabolic activity in spinal cord and dorsal root ganglion in the rat.* Proceedings of the National Academy of Sciences, 1985. **82**(17): p. 6010-6013.

18. Al-Majed, A.A., et al., *Brief electrical stimulation promotes the speed and accuracy of motor axonal regeneration.* Journal of Neuroscience, 2000. **20**(7): p. 2602-2608.

19. Nowak, L. and J. Bullier, *Axons, but not cell bodies, are activated by electrical stimulation in cortical gray matter I. Evidence from chronaxie measurements.* Experimental brain research, 1998. **118**(4): p. 477-488.

20. Gordon, T., et al., *Brief post-surgical electrical stimulation accelerates axon regeneration and muscle reinnervation without affecting the functional measures in carpal tunnel syndrome patients.* Experimental neurology, 2010. **223**(1): p. 192-202.

21. Gomez, N. and C.E. Schmidt, *Nerve growth factor-immobilized polypyrrole: Bioactive electrically conducting polymer for enhanced neurite extension.* Journal of biomedical materials research Part A, 2007. **81**(1): p. 135-149.

22. Kotwal, A. and C.E. Schmidt, *Electrical stimulation alters protein adsorption and nerve cell interactions with electrically conducting biomaterials.* Biomaterials, 2001. **22**(10): p. 1055-1064.

23. Xu, H., et al., *Conductive PPY/PDLLA conduit for peripheral nerve regeneration.* Biomaterials, 2014. **35**(1): p. 225-235.

24. Aebischer, P., et al., *Piezoelectric guidance channels enhance regeneration in the mouse sciatic nerve after axotomy.* Brain research, 1987. **436**(1): p. 165-168.

25. Lee, Y.-S. and T.L. Arinzeh, *The influence of piezoelectric scaffolds on neural differentiation of human neural stem/progenitor cells.* Tissue Engineering Part A, 2012. **18**(19-20): p. 2063-2072.

26. Saltzman, W.M. and T.R. Kyriakides, *Cell interactions with polymers.* Principles of tissue engineering, 2000. **2**.

CHAPTER 4. MECHANICAL/ELECTRICAL STIMULATION ENHANCES GLIAL CELL FUNCTIONALITY

Abstract

Glial cells of the peripheral and central nervous system play an essential role in the process of axon regeneration when the nerve is injured. When a peripheral nerve is damaged, Schwann cells, the glial cell type of the peripheral nervous system, are responsible for clearing necrotic axon and myelin debri, secreting neurotrophic factors to induce axon regrowth, and myelinate the regenerated axon. Following injury of a central nerve, neural stem cells differentiate into oligodendrocytes and astrocytes, the glial cell types of the central nervous system, to remyelinate the axon and for glial scar tissue which possess supportive factors for axon regrowth, respectively. Electrical stimulation has been widely investigated for its use to enhance nerve regeneration due to the innate electrical nature of the nervous system. Specifically, electrical stimulation has shown to enhance the functionality of glial cells. In this study, we demonstrated the capability of subjecting electrical stimulation by non-contact mechanical/electrical stimulation of aligned electrospun PVDF-TrFE scaffolds to induce the maturation of functional glial cells from the PNS and CNS. Mechanical/electrical stimulation induced Schwann cells of the PNS produced NGF for enhancing axon regrowth. Alternatively, mechanical/electrical stimulation induced differentiation of NSCs toward myelin-secreting oligodendrocytes and axon permissive factor-producing astrocytes.

4.1. Introduction

Injury to the peripheral and central nervous systems often leads to minimal or permanent loss of motor and sensory functions. It is debilitating and significantly decreases an individual's quality of life. Functional recovery depends of the capacity of axon regeneration following neural damage, whether it be from a traumatic injury or disease. The peripheral nervous system (PNS) is naturally more capable of axon repair than the central nervous system (CNS) after injury as a result of its own promoting cellular, environmental, and intrinsic factors (**Figure 4.1**) [1]. Specifically, the behaviors of glial cells, such as Schwann cells in the PNS, and oligodendrocytes and astrocytes of the CNS, play an important role in the regeneration process [2, 3].

When the PNS is damaged and axons are transected, a process known as Wallerian degeneration occurs and the distal axon stump degenerates to the target tissue [4]. Native Schwann cells, the glial cell of the PNS, dedifferentiate and convert into a repair Schwann cells phenotype to create and enhance a permissive environment to facilitate axon regeneration. These reprogrammed cells are responsible for the upregulation of neurotrophic factors, including nerve growth factor (NGF), elevation of pro-inflammatory (IL-1β and TNFα) and anti-inflammatory (IL-4 and IL-10) cytokines, recruitment of macrophages and additional Schwann cells for myelin breakdown and clearance , and formation of regeneration pathway for directing axons towards their target tissue [5, 6].

In contrast, when a CNS axon is damaged, i.e. spinal cord injury or traumatic brain injury, it does not spontaneous regenerate due to its prohibitive inflammatory

environment [7]. In response to an injury, adult neural stem cells in the white matter of the spinal cord differentiate into oligodendrocytes and astrocytes [8]. The differentiated mature myelinating oligodendrocytes, a glial cell type of the CNS, quickly remyelinates axons and secrete metabolic factors to maintain CNS neurons. However, reactive astrocytes form glial scars that create a physical barrier, inhibiting axon regeneration [9]. It was originally believed that the formation of glial scar tissue was the major inhibitory factor for regeneration following CNS injury. However, it has been recently demonstrated that regeneration cannot occur in the absence of glial scar formation [10]. In fact, scar-forming astrocytes upregulate growth supportive factors, CSPG4 and CSPG5, that promote axon regrowth. Therefore, it is essential to modulate the cellular activities of both myelinating oligodendrocytes and extracellular matrix-producing astrocytes to promote nerve regeneration across severe CNS injuries.

Applied electric field has been demonstrated to accelerate nerve regeneration in both PNS [11-13] and CNS [14-16]. In particular, glial cells have been shown to respond to electrical cues by activation of voltage-gated ion channels [17, 18]. In Schwann cells, electrical stimulation induces calcium influx through T-type voltage-gated calcium channels and subsequently enhances nerve growth factor (NGF) production, a neurotrophic protein essential for axon growth [19]. Electrical stimulation can also modulate neural stem cell behavior to differentiate towards the two glial cell types in the CNS, oligodendrocytes and astrocytes, as well as neurons [20, 21]. Despite its promising potential for stimulating glial cell differentiation and functionality, the application of

electrical stimulation has been limited in clinical settings due to its invasive implantation of electrodes and limited stimulation area.

In this regard, piezoelectric materials can be utilized as a non-contact electrical stimulation platform for glial cell differentiation. When the piezoelectric material is subjected to mechanical stress, an electric charge is generated at the surface of the material [22]. Poly(vinylidene fluoride) (PVDF) and its derivatives including P(VDF-trifluoroethanol) (PVDF-TrFE), biocompatible piezoelectric polymer, have been explored as a platform for nerve regeneration, including the stimulating Schwann cells to secrete neurotrophic factors, inducing differentiation of neural stem cells, and promoting neurite elongation of dorsal root ganglia [23-25]. However, due to the lack of systematic piezoelectric characterization and limited mechanistic understandings, the full potential of the piezoelectric polymer is yet to be explored.

In this study, PVDF-TrFE nanofibrous scaffolds were utilized to determine their potential for enhancing glial cell differentiation and functionality. Schwann cells and neural stem cells were subjected to mechanical/electrical stimulation and their changes behaviors were observed by assessing changes in gene and protein expression. We demonstrated the anabolic activities of mechanical/electrical stimulation to promote the functionalization of Schwann cells to mature myelinating cells and the differentiation of neural stem cells to oligodendrocytes and astrocytes for potential enhancement of nerve regeneration.

4.2. Materials and methods

4.2.1. Synthesis and morphological characterization of PVDF-TrFE nanofibrous scaffolds

11.5 wt.% PVDF-TrFE (Solvay, Belgium) was dissolved in a 60/40 volume ratio of dimethylformamide (DMF, Sigma Aldrich, St. Louis, MO) to acetone (Sigma Aldrich) solvent system, with the addition of 1 wt.% pyridinium formate (PF) buffer (Sigma Aldrich). The solution was magnetically stirred at 1200 rpm for 3 hr at room temperature. A high voltage source was utilized to apply -18.4 kV to charge the solution dispensing through a 22 G needle at 6 ml/hr and elongate the fluid jet across a 10 cm needle tip to grounded collector distance. Finally, the fluid jet was collected onto a high speed grounded mandrel rotating at 47.9 m/s to produce aligned fibers. The fibers were collected for 4 hr to produce a 200 µm thick scaffold. Lastly, the electrospun fiber mats were subjected to annealing at 90 °C for 24 hr to further enhance the piezoelectric properties of PVDF-TrFE.

4.2.2. Cell culture for mechanical/electrical stimulation

A custom cell culture system was utilized to apply non-contact mechanical/electrical stimulation to the cell-seeded electrospun PVDF-TrFE scaffolds by a translational actuation stage (**Figure 2.5**). PVDF-TrFE scaffolds were cut into 45 mm X 5 mm strips. A hydrophobic SIBS coating was applied to leave an area of 15 mm x 5 mm to confine the cell culture space. The cell culture chamber and PVDF-TrFE strips were sterilized separately in 70% ethanol for 1 hr. The cell culture chamber was dried overnight

drying to remove any ethanol vapor. The PVDF-TrFE strips were washed in PBS before assembling into the dried, sterile chamber.

Immortalized rat neuronal Schwann cells (RSC96) were purchased from ATCC (Manassas, VA). They were cultured in high glucose Dulbecco's Modified Eagle Medium (DMEM, Lonza, Morristown, NJ), supplemented with 10% fetal bovine serum (FBS, VWR, Radnor, NJ) and 1% penicillin/streptomycin (Mediatech, Manassas, VA) and maintained in a standard 37 °C incubator with 5% CO_2. Medium was replaced every 2-3 days and once it reached 70-80% confluency the cells were detached using 0.25% Trypsin/EDTA (Life Technologies, Carlsbad, CA) for 3 min at 37 °C. The RSC96 were seeded onto the PVDF-TrFE scaffold assembled in the cell culture chamber at 5,000 cells/cm^2 and allowed to attach for 2 h prior to filling the cell culture chamber. During the experiment, the cells were maintained in the maintenance media with no additional growth factors.

Alternatively, C17.2 neural stem cells (NSCs), derived from the cerebellum of neonatal mouse, were cultured in high glucose DMEM, supplemented with 10% FBS (Sigma Aldrich, St Louis, MO), 5% horse serum (Gibco, Gaithersburg, MD), 1% sodium pyruvate (Gibco), and 1% penicillin/streptomycin in a standard 37 °C incubator with 5% CO_2. The cells were cultured up to 70-80% confluency and medium was replaced every 2-3 days. Once the cells reached confluency, the cells were incubated in 0.05% trypsin EDTA/PBS for 2 min at 37°C. The NSCs were seeded onto the sterile PVDF-TrFE scaffolds assembled in the cell culture chamber at 5,000 cells/cm^2 and the cells were allowed to attach for 2 hours before filling up the chamber with additional media. During the

experiment, the cells were maintained in the maintenance media with no additional growth factors.

The cells seeded on the PVDF-TrFE scaffolds were cultured for 24 hr before subjecting them to mechanical/electrical stimulation. The cell-seeded scaffold was vertically actuated on the vertical oscillation stage to apply a surface strain of approximately 0.03%, which was determined to generate 200 mV_{p-p} for a 200 µm thick PVDF-TrFE scaffold when oscillating at 3 Hz. The cell/scaffold constructs were either stimulated daily for 2 hr for seven days. As a control, cells were cultured in the cell culture system statically as well as on tissue culture plates for the same duration. At the conclusion of the experiment, cells were subjected to lysis buffer for gene expression analysis or 4% paraformaldehyde (PFA) for protein expression analysis.

4.2.3. Protein expression analysis

To determine if mechanical/electrical stimulation induced the production of NGF by RSC96, NGF receptors on the cells were stained with anti-NGF (Santa Cruz Biotechnology, Dallas, TX) as the primary antibody and with Alexa Fluor-594 (Jackson ImmunoResearch, West Grove, PA) as the secondary antibody. The samples were subsequently counter-stained with 4',6-Diamidino-2-Phenylindole (DAPI, Vector Laboratories, Burlingame, CA) for nuclei and Alexa Fluor-488 Phalloidin (Invitrogen, Carlsbad, CA) for actin.

To characterize the phenotypic changes to NSCs that occurred during mechanical/electrical stimulation, the cells were immuno-stained with primary antibodies for markers of either NSCs (Nestin, DSHB, Iowa City, IA), neurons (βIII tubulin, Thermo Fisher Scientific, Waltham, MA), oligodendrocytes (O4, R&D Systems, Minneapolis, MN), or astrocytes (GFAP, Santa Cruz Biotechnology) with the appropriate secondary antibody Alexa Fluor-488. The samples were counter-stained with DAPI and Alexa Fluor-594 followed by analysis using immunofluorescence microscopy. The ImageJ software was utilized to determine the fluorescence intensity of each protein of interest.

4.2.7. Gene expression analysis

The effects of mechanical/electrical stimulation on RSC96 and NSCs, gene expression after 7 days of mechanical/electrical stimulation were determined at the gene level by real-time polymerase chain reaction (RT-PCR). Total RNA was extracted using an RNeasy Micro Kit (Qiagen, Valencia, CA), and cDNA synthesis was performed using iScript cDNA Synthesis Kit (Bio-Rad, Hercules, CA) according to manufacturers' protocols. Real-time PCR was performed to determine the gene expression of myelinating factors of rat RSC96s (**Table 4.1**) and phenotypic markers for mouse NSCs (**Table 4.2**). Data were analyzed by the comparative threshold cycle (C_T) method using *Rps18* for RSC96s and *Gapdh* for NSCs as an endogenous control.

4.2.8. Statistical analysis

Statistical analysis was performed with at least three biologically independent samples, and represented as an average ± standard deviation (SD) or standard error of mean (SEM) as indicated. The data were subjected to ANOVA with Tukey's post-hoc test using the SPSS software (IBM) to determine statistical significance ($p < 0.05$).

4.3. Results

4.3.1. Effects of non-contact mechanical/electrical stimulation on RSC96

Based on our previous study, the solution and electrospinning parameters were optimized to produce 200 μm thick scaffold of uniform cylindrical structures with a fiber diameter of 500 nm and 90% alignment within 20° deviation. RSC96 cells, a rat Schwann cell line, were seeded on the piezoelectric scaffolds and subjected to a dynamic strain regimen to produce approximately 200 V_{p-p}, which has shown to enhance neuronal functions. The effects of mechanical/electrical stimulation by PVDF-TrFE on the cells were was determined by immunocytochemistry (**Figure 4.2**) and real-time polymerase chain reaction (rt-PCR) (**Figure 4.3**). RSC96 cells cultured statically on the scaffolds and on tissue culture plastics served as controls. Under the static condition on the scaffolds, the cells grew in colonies, similar to those cultured on tissue culture plates. In contrast, mechanical/electrical stimulation induced more single cell formation (**Figure 4.2 (A)**). Coincidently, the expression of NGF by RSC96 was significantly greater in the mechanical/electrical stimulation condition as compared to statically cultured cells on

PVDF-TrFE (**Figure 4.2 (B)**). Furthermore, the application of mechanical/electrical stimulation induced a significant upregulation in gene expression of pro-myelinating Schwann cell markers, *NGF*, *Krox20*, and *PMP22*, while there was suppression of the immature Schwann cell marker, *NCAM-1* (**Figure 4.3**).

4.3.2. Effects of mechanical/electrical stimulation on NSCs

To determine the effects of mechanical/electrical stimulation on the phenotypic fate of NSC, changes in protein and gene expression by immunocytochemistry (**Figure 4.4 and 4.5**) and rt-PCR (**Figure 4.6, 4.7 and 4.8**), respectively, were analyzed. At the protein level, expression of Nestin, a NSC marker, is prevalent in both static and piezoelectric conditions, indicating there are still naïve undifferentiated cells differentiating (**Figure 4.5**). It is also observed that the NSC maintained its typical round morphology. Although both mechanical/electrical stimulation and static condition expressed the neuronal marker, βIII tubulin, as well as having an elongated cellular morphology characteristic of neurons,0 there is greater intensity of expression in the stimulated condition. Interestingly, the expression of oligodendrocyte marker, O4, and astrocyte marker, GFAP, were only observed in the mechanical/electrical stimulation conditions. Relative changes in gene expression for the maintenance of NSC phenotype or for differentiation towards the three neural cell types of the CNS was analyzed by rt-PCR. There was a downregulation of NSC genes in both static and mechanical/electrical stimulation conditions, indicating the on-going differentiation of cells (**Figure 4.6**), while there was a downregulation in the

immature neuron marker, *Tubb3*, but an upregulation of mature neuron marker, *Map2* and *Eno2*, under mechanical/electrical stimulation. This gene expression agrees with the observation of greater expression of βIII tubulin at the protein level. As expected from the immunocytochemistry results, mechanical/electrical stimulation induced a significant upregulation in gene expression for both oligodendrocyte (*Olig1*, *Cldn11*, and *Mog*) and astrocyte (*Gfap, Cspg4,* and *Ntf3*) markers, signifying the capability of mechanical/electrical stimulation to differentiate NSCs into glial cell types.

4.4. Discussion

The present study demonstrated that mechanical/electrical stimulation was effective in modulating glial cell behavior. In Schwann cells (RSC96), a glial cell type in the PNS, mechanical/electrical stimulation enhanced the production of a neurotrophic factor, NGF. In NSCs, mechanical/electrical stimulation induced the differentiation towards oligodendrocytes and astrocytes, glial cell phenotypes of the CNS, required for nerve regeneration.

A peak-to-peak voltage of 200 mV produced by PVDF-TrFE at 3 Hz, 2 hr per day for 7 days resulted in changes in gene and protein expression of myelinating markers and neurotrophin secretion in Schwann cells. Nerve growth factor (*NGF*), early growth response 2 (*Krox20*), and peripheral myelin protein 22 (*PMP22*) are markers that indicate myelination of Schwann cells [26, 27]. In contrast, *NCAM-1* is expressed in immature Schwann cells during development. When Schwann cells convert into their myelinating

phenotype, a downregulation of *NCAM-1* is observed, while an upregulation of *NGF*, *Krox20*, and *PMP22* occurs. Schwann cells have been shown to respond to electrical cues due to activation of voltage-gated calcium channels [28]. Calcium ions have been demonstrated to regulate many electrical stimulation-induced intracellular events, including its important role in regulating neurotrophin expression [17, 19, 29]. Specifically, NGF production in Schwann cells has been shown to require both an influx of calcium across the plasma membrane as well as calcium immobilization from internal calcium reservoirs [19, 30]. Both of these events can occur when the Schwann cells are exposed to electrical stimulation.

Neural stem cells predominately exist in the white matter of the spinal cord within the CNS [31]. Their phenotypic fate is glial cells, mainly oligodendrocytes and astrocytes. At the onset of CNS pathological diseases or injuries, NSCs are activated and differentiate into myelinating oligodendrocyte and astrocytes [8]. Neuronal activity, i.e., action potential propagation, is also important for inducing this transformation of NSC to myelinating oligodendrocytes and astrocytes for axon regrowth. These newly differentiated cells migrate to the location of the injury site and begin responding damaged tissue. The oligodendrocytes begin to remyelinate the damaged axon, while astrocytes begin to secrete inhibitory and permissive factors for glial scar formation.

Recent studies have demonstrated the capability of electrical stimulation to induce NSC differentiation [20, 32, 33]. Due to the native electrical activities of neurons, NSC differentiation towards neurons has been widely studied [34-36]. Although the

mechanism is not clear, electrical stimulation has been found to modulate signaling cascades that regulate calcium influxes which subsequently affects mitogenesis [37]. Biphasic electrical current has been demonstrated to induce the proliferation and differentiation of neural stem cells towards neuronal lineages [38]. Furthermore, electrical stimulation by conductive polymers have been utilized to differentiate NSC towards neurons with elongated neurites [39]. A similar differentiation of NSCs under mechanical/electrical stimulation was observed in this study, evident from the downregulation of NSC gene markers. Interestingly, βIII tubulin, a neuronal marker, was observed in both stimulated and static conditions. NSCs have been reported to respond to substrate morphology, enhancing differentiation towards neurons, due to their elongated nature [40, 41]. By culturing the cells on aligned PVDF-TrFE was sufficient to induce the cells to differentiate towards neurons, as seen in the static condition. At the gene level, there was downregulation of *Tubb3*, a marker for immature neurons , in both mechanical/electrical stimulation and static conditions. However, there was an upregulation in *Map2* and *Eno2*, both markers for mature neurons, only under mechanical/electrical stimulation, suggesting the functional maturation of the cells [42].

Unlike neuronal differentiation of NSCs, their differentiation towards oligodendrocytes and astrocytes is less explored. In the present study, we observed an upregulation of oligodendrocyte and astrocyte markers when the NSCs were subjected to mechanical/electrical stimulation as compared the static control. At the protein level, mechanical/electrical stimulation was enough to induce expression of O4, an

oligodendrocyte marker, and GFAP, an astrocyte marker, while there was no expression observed in the static conditions. At the gene level, an upregulation of *Olig1*, a marker for the maturation of oligodendrocytes, *Cldn11*, and *Omg*, both markers indicating myelination of oligodendrocytes [43]. There was also a significant upregulation of *Gfap*, a filament marker of astrocytes, *Cspg4*, and *Ntf3*, both markers of secreted protein by astrocytes that promote axon regeneration [10].

Mechanical/electrical stimulation may either directly or indirectly affect glial differentiation of NSC. Mechanical/electrical stimulation can directly affect neural stem cells by activating voltage-gated ion channels, specifically calcium ions, similarly to how the stimulation affects Schwann cells . Glial cells can also indirectly benefit from the activity of functional neurons activated by mechanical/electrical stimulation. Studies have shown that neuronal activity can drive oligodendrocyte progenitors to mature oligodendrocytes capable of remyelination of damaged nerves [44, 45]. It has been demonstrated that active neurons initiate ATP signaling, which stimulates astrocytes to release promoting factors of axon regeneration, such as neuroglycans and neurotrophins. The contribution and decoupling of direct and indirect piezoelectric effects on the glial cell differentiation of NSCs need further controlled experimentation. Nevertheless, we demonstrated that mechanical/electrical stimulation provides a means to enhance the functionality of glial cells to promote nerve regeneration.

4.5. Conclusion

Due to their impact on nerve regeneration, strategies for enhancing glial cell functionality can improve methods for effective nerve repair. In this study, we successfully demonstrated the feasibility of non-contact mechanical/electrical stimulation by aligned electrospun PVDF-TrFE scaffolds to induce the maturation of functional glial cells from the PNS and CNS. Mechanical/electrical stimulation induced Schwann cells of the PNS produced NGF for enhancing axon regrowth. Alternatively, mechanical/electrical stimulation induced differentiation of NSCs toward myelin-secreting oligodendrocytes and axon permissive factor-producing astrocytes.

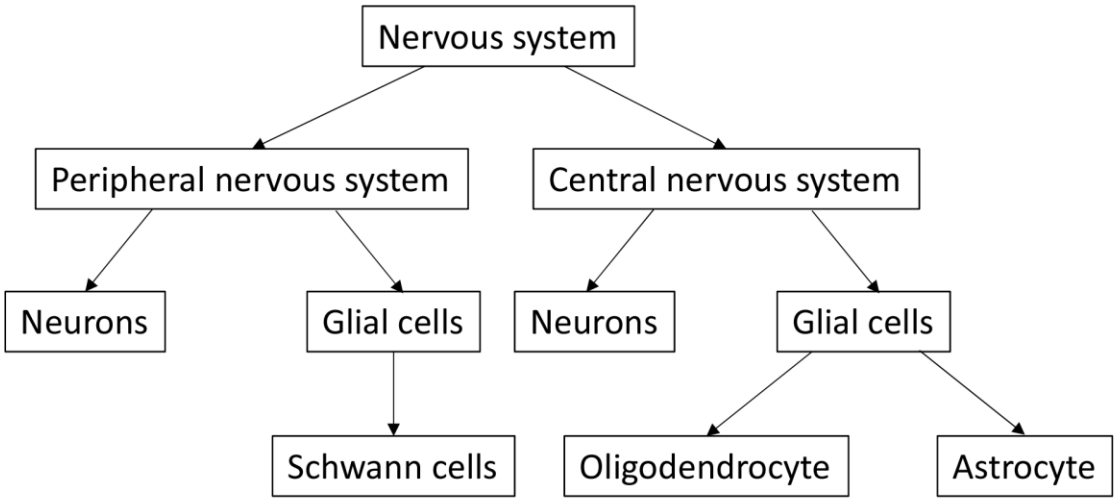

Figure 4.1. Cellular components of the nervous system. The nervous system is broken down into the peripheral and central nervous system. Each system possesses their own neuronal and glial cell types.

Primer	Forward	Reverse
Rps18	*5'*-CCCGAGAAGTTTCAGCACATC-*3'*	*5'*-ATGGCAGTGATAGCGAAGGCT-*3'*
Ngf	*5'*-TTCCAGGCCCATGGTACAAT-*3'*	*5'*-AAACTCCCCCATGTGGAAGAC-*3'*
Krox20	*5'*-TGCGCCTAGAAACCAGACCTT-*3'*	*5'*-ATGCCCGCACTCACAATATTG-*3'*
Pmp22	*5'*-TGTACCACATCCGCCTTGG-*3'*	*5'*-GAGCTGGCAGAAGAACAGGAAC-*3'*
Ncam-1	*5'*-TGGAACGCCGAGTACGAAGTA-*3'*	*5'*-TGAACACGAAGTGAGCTGCCT-*3'*

Table 4.1. Primer sets for rat RSC96 used for rt-PCR analysis

Marker	Primer	Forward	Reverse
Housekeeping	*Gapdh*	*5′*- GGCAAATTCAACGGCACAGT-*3′*	*5′*-TCGCTCCTGGAAGATGGTGAT-*3′*
NSC	*Nestin*	*5′*-GCGCTGGAACAGAGATTGGAA-*3′*	*5′*-TGGTATCCCAAGGAAATGCAG-*3′*
	Msi1	*5′*-GATGCCATGCTGATGTTCGAC-*3′*	*5′*-ATGTCCTCGCTCTCAAACGTG-*3′*
	Sox2	*5′*-TTTTGTCCGAGACCGAGAAGC-*3′*	*5′*-CATGAGCGTCTTGGTTTTCCG-*3′*
Neuron	*Tubb3*	*5′*-ACCTTGTGTCTGCCACCATGA-*3′*	*5′*-CACCATGTTCACAGCCAGCTT-*3′*
	Map2	*5′*-AAGCCATTGTGTCCGAACCA-*3′*	*5′*-GAGCGGAAGAGCAGTTTGTCA-*3′*
	Eno2	*5′*-ATCGCCACATTGCTCAGCTAG-*3′*	*5′*-TGAGAGCCACCATTGATCACA-*3′*
Oligodendrocyte	*Olig1*	*5′*-ACGCCAAAGAGGAACAGCA-*3′*	*5′*-TCCATGGCCAAGTTCAGGT-*3′*
	Cldn11	*5′*-TGGCATCATCGTCACAACGT-*3′*	*5′*-CCCAGTTCGTCCATTTTTCG-*3′*
	Mog	*5′*-TGCCCTGCTGGAAGATAACAC-*3′*	*5′*-TGCAGCCAGTTGTAGCAGATG-*3′*
Astrocyte	*Gfap*	*5′*-TGGAGCTCAATGACCGCTTT-*3′*	*5′*-GCTCGAAGCTGGTTCAGTTCA-*3′*
	Cspg4	*5′*-CTGAGCAATCTGTCTTTCCCAGT-*3′*	*5′*-TGTGTATGCAGAGGTTCAAGCCT-*3′*
	Ntf3	*5′*-TCACCACGGAGGAAACGCTAT-*3′*	*5′*-TCAATGGCTGAGGACTTGTCG-*3′*

Table 4.2. Primer sets for mouse NSCs used for rt-PCR analysis.

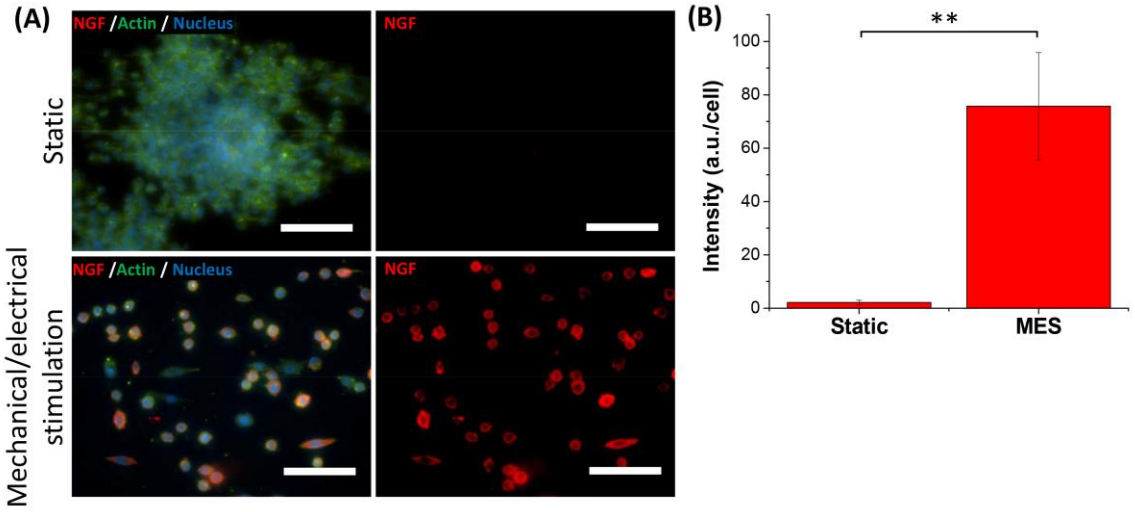

Figure 4.2. NGF protein expression of RSC96 cells subjected to mechanical/electrical stimulation for 7 days. (A) Protein expression for secretory protein, NGF, of myelinating RSC96 cells cultured (A) statically or (B) subjected to mechanical/electrical stimulation on PVDF-TrFE. (B) The fluorescent intensity was compared between the two conditions. (Scale bar = 100 μm)

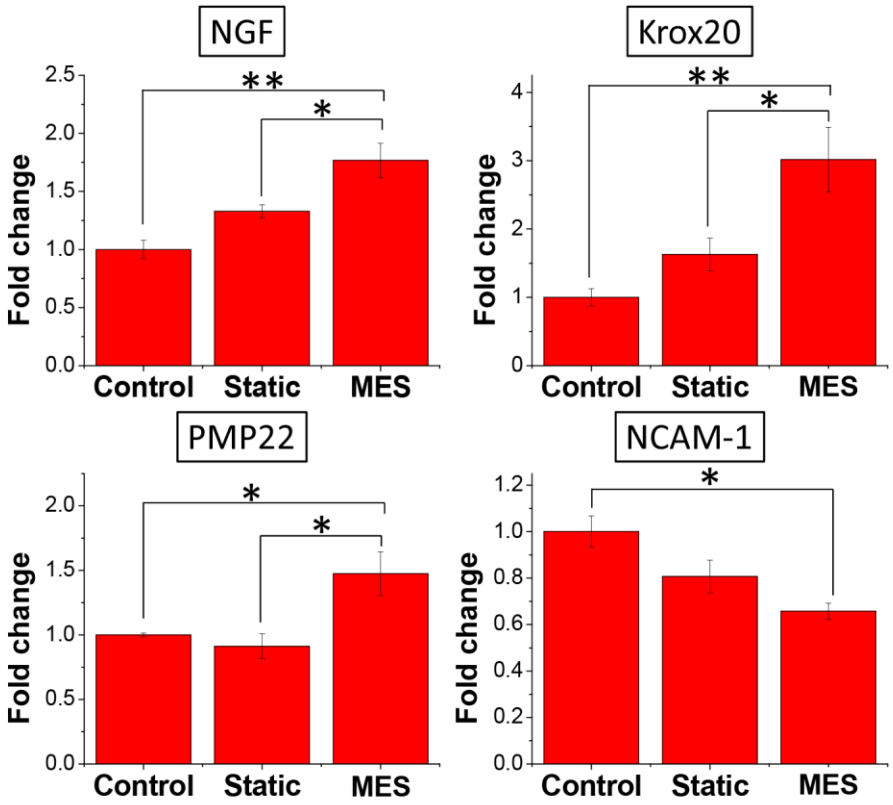

Figure 4.3. The relative gene expression of RSC96 subjected to mechanical/electrical stimulation for 7 days determined by RT-PCR. Myelination markers (Krox20, PMP22, and NCAM-1) and secretion of NGF. The gene expression of RSC96 cultured on tissue culture plates was used as a control.

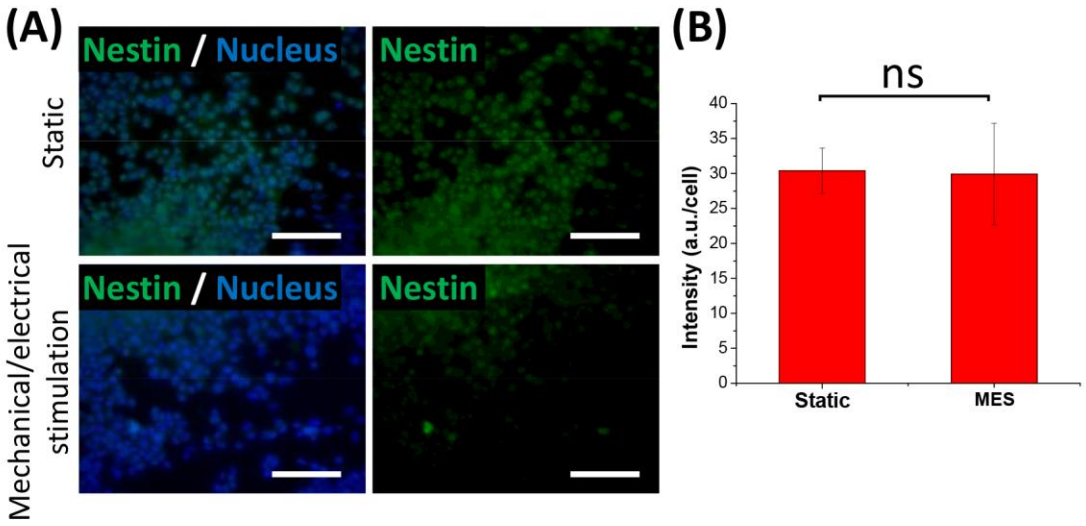

Figure 4.4. Nestin protein expression of mNSCs subjected to mechanical/electrical stimulation for 7 days. Protein expression for neural stem cell marker, Nestin, of mNSC cultured statically or (B) subjected to mechanical/electrical stimulation on PVDF-TrFE. (B) The fluorescent intensity was compared between the two conditions. (Scale bar = 100 µm)

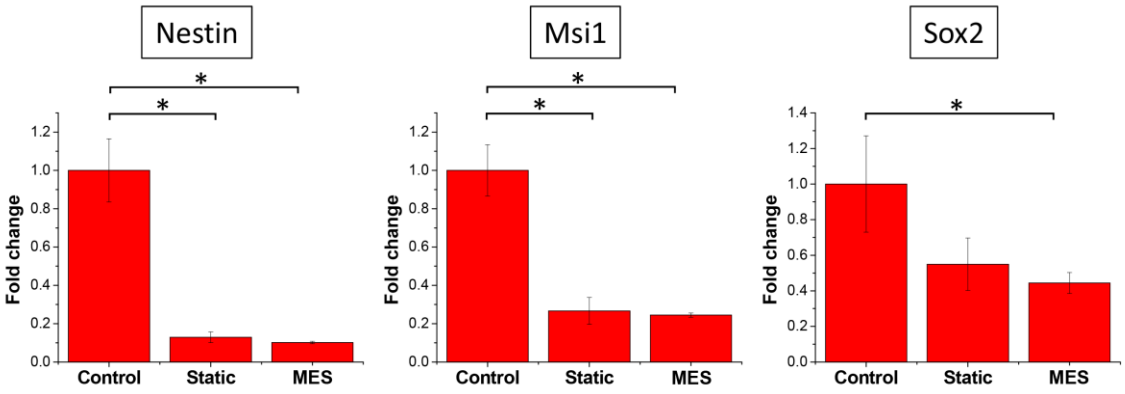

Figure 4.5. The relative gene expression of neural stem cell markers of mNSCs subjected to mechanical/electrical stimulation for 7 days determined by RT-PCR. The gene expression of mNSC cultured on tissue culture plates was used as a control.

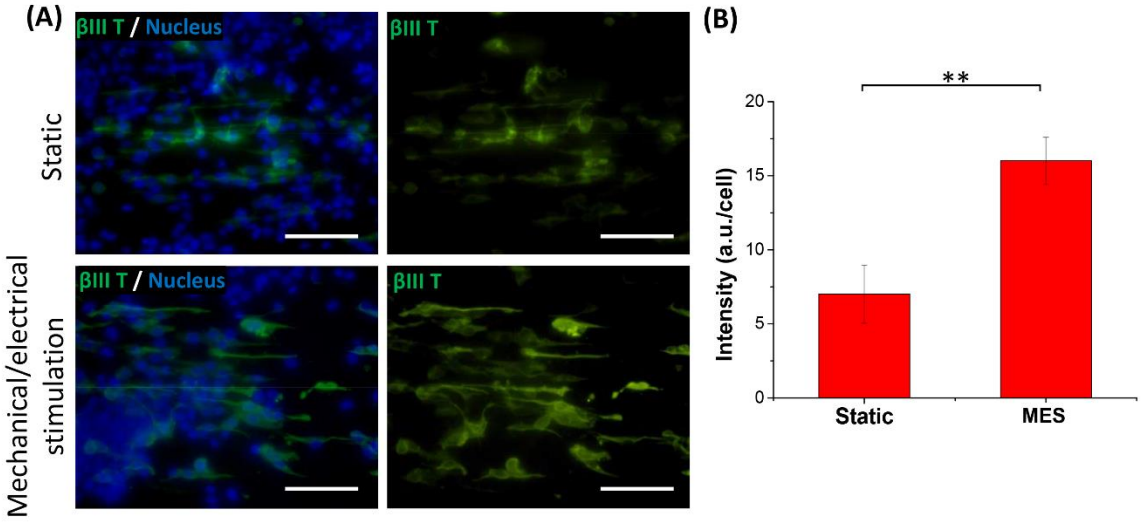

Figure 4.6. βIII tubulin protein expression of mNSCs subjected to mechanical/electrical stimulation for 7 days. Protein expression for neuronal marker, βIII tubulin, of mNSC cultured statically or (B) subjected to mechanical/electrical stimulation on PVDF-TrFE. (B) The fluorescent intensity was compared between the two conditions. (Scale bar = 100 μm)

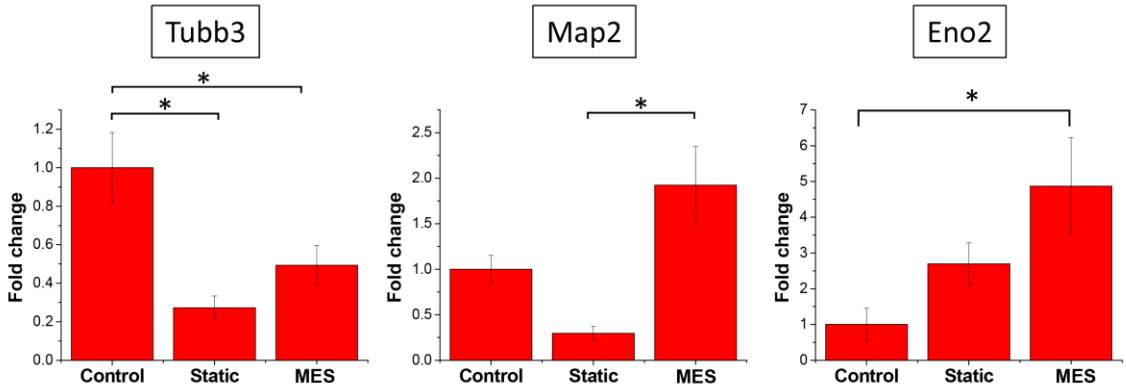

Figure 4.7. The relative gene expression of neuron makers of mNSCs subjected to mechanical/electrical stimulation for 7 days determined by RT-PCR. The gene expression of mNSC cultured on tissue culture plates was used as a control.

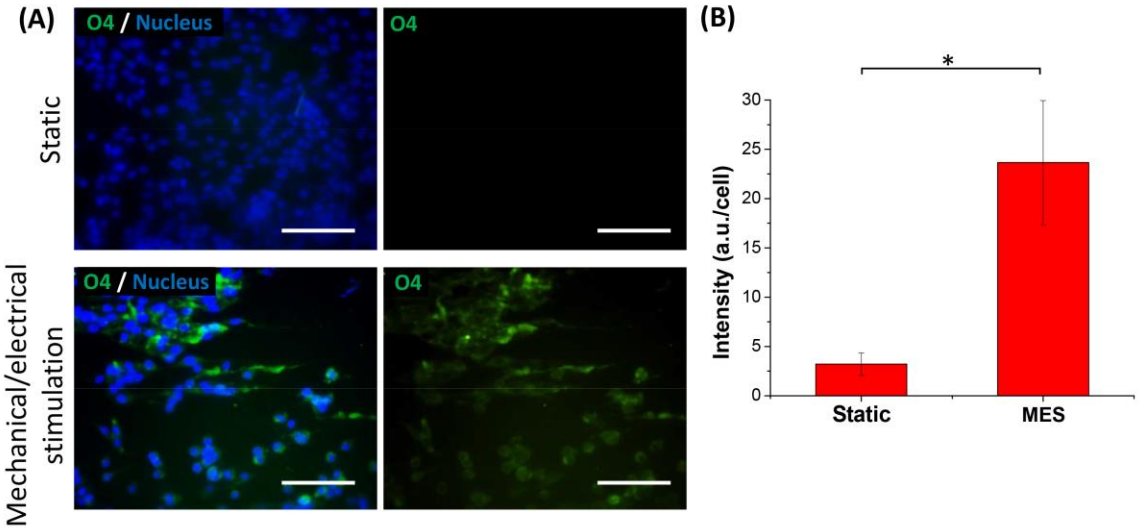

Figure 4.8. O4 protein expression of mNSCs subjected to mechanical/electrical stimulation for 7 days. Protein expression for oligodendrocyte marker, O4, of mNSC cultured statically or (B) subjected to mechanical/electrical stimulation on PVDF-TrFE. (B) The fluorescent intensity was compared between the two conditions. (Scale bar = 100 µm)

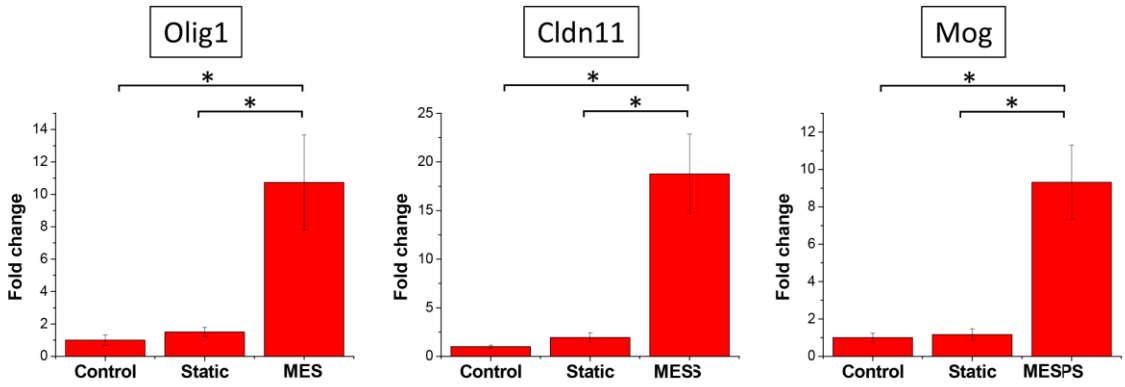

Figure 4.9. The relative gene expression of oligodendrocyte markers of mNSCs subjected to mechanical/electrical stimulation for 7 days determined by RT-PCR. The gene expression of mNSC cultured on tissue culture plates was used as a control.

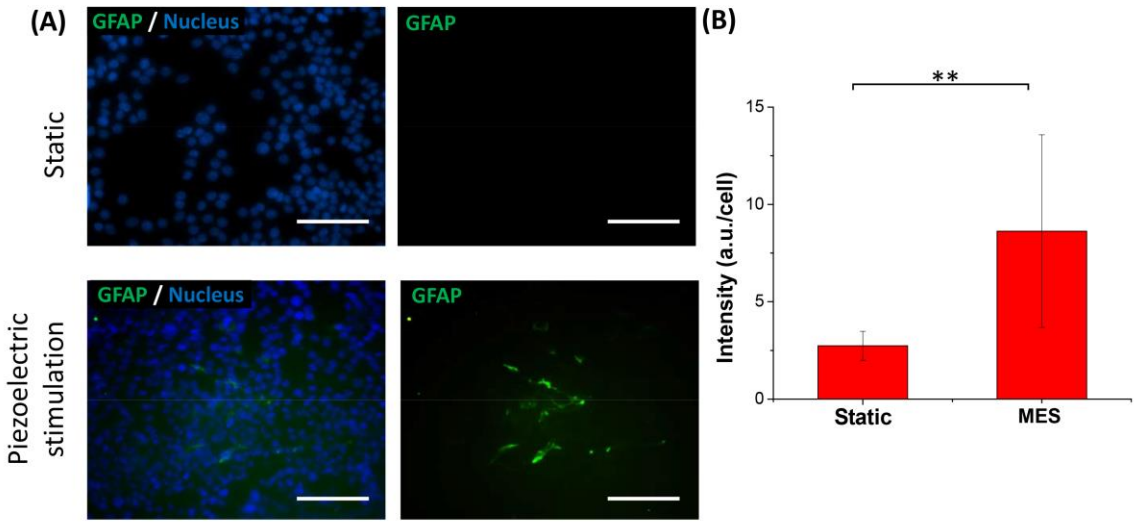

Figure 4.10. GFAP protein expression of mNSCs subjected to mechanical/electrical stimulation for 7 days. Protein expression for astrocyte marker, GFAP, of mNSC cultured statically or (B) subjected to mechanical/electrical stimulation on PVDF-TrFE. (B) The fluorescent intensity was compared between the two conditions. (Scale bar = 100 µm)

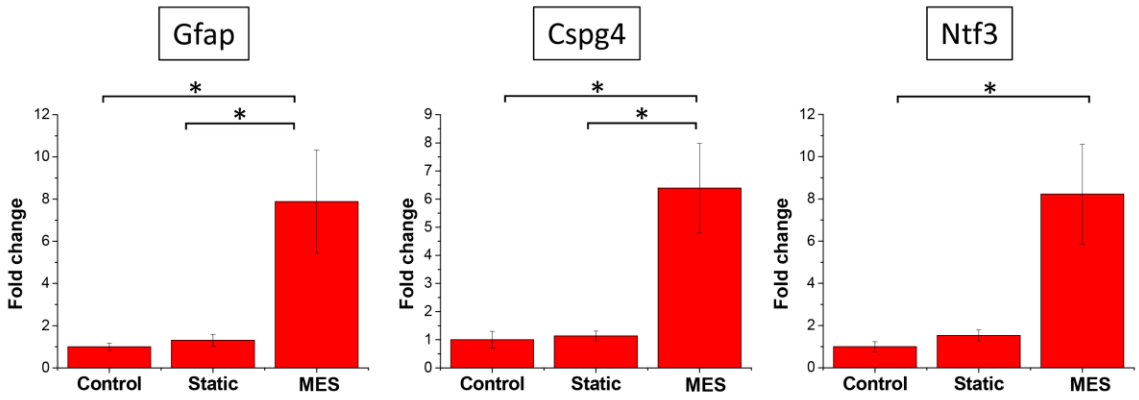

Figure 4.11. The relative gene expression of astrocyte markers of mNSCs subjected to mechanical/electrical stimulation for 7 days determined by RT-PCR. The gene expression of mNSC

References

1. Huebner, E.A. and S.M. Strittmatter, *Axon regeneration in the peripheral and central nervous systems*, in *Cell Biology of the Axon*2009, Springer. p. 305-360.

2. Sjöstrand, J., *Proliferative changes in glial cells during nerve regeneration.* Cell and Tissue Research, 1965. **68**(4): p. 481-493.

3. Fu, S.Y. and T. Gordon, *The cellular and molecular basis of peripheral nerve regeneration.* Molecular neurobiology, 1997. **14**(1-2): p. 67-116.

4. Faweett, J. and R.J. Keynes, *Peripheral nerve regeneration.* Annual review of neuroscience, 1990. **13**(1): p. 43-60.

5. Dubový, P., I. Klusáková, and I. Hradilová Svíženská, *Inflammatory Profiling of Schwann Cells in Contact with Growing Axons Distal to Nerve Injury.* BioMed Research International, 2014. **2014**: p. 691041.

6. Frostick, S.P., Q. Yin, and G.J. Kemp, *Schwann cells, neurotrophic factors, and peripheral nerve regeneration.* Microsurgery, 1998. **18**(7): p. 397-405.

7. Horner, P.J. and F.H. Gage, *Regenerating the damaged central nervous system.* Nature, 2000. **407**(6807): p. 963.

8. Sabelström, H., M. Stenudd, and J. Frisén, *Neural stem cells in the adult spinal cord.* Experimental neurology, 2014. **260**: p. 44-49.

9. Faulkner, J.R., et al., *Reactive astrocytes protect tissue and preserve function after spinal cord injury.* Journal of Neuroscience, 2004. **24**(9): p. 2143-2155.

10. Anderson, M.A., et al., *Astrocyte scar formation aids CNS axon regeneration.* Nature, 2016. **532**(7598): p. 195.

11. Kerns, J., et al., *Electrical stimulation of nerve regeneration in the rat: the early effects evaluated by a vibrating probe and electron microscopy.* Neuroscience, 1991. **40**(1): p. 93-107.

12. Asensio-Pinilla, E., et al., *Electrical stimulation combined with exercise increase axonal regeneration after peripheral nerve injury.* Experimental neurology, 2009. **219**(1): p. 258-265.

13. Lu, M.-C., et al., *Effects of electrical stimulation at different frequencies on regeneration of transected peripheral nerve.* Neurorehabilitation and neural repair, 2008. **22**(4): p. 367-373.

14. Baldessarini, R.J. and I.J. Kopin, *The effect of drugs on the release of norepinephrine-H3 from central nervous system tissues by electrical stimulation in vitro.* Journal of Pharmacology and Experimental Therapeutics, 1967. **156**(1): p. 31-38.

15. Udina, E., et al., *Electrical stimulation of intact peripheral sensory axons in rats promotes outgrowth of their central projections.* Experimental neurology, 2008. **210**(1): p. 238-247.

16. Ranck, J.B., *Which elements are excited in electrical stimulation of mammalian central nervous system: a review.* Brain research, 1975. **98**(3): p. 417-440.

17. Verkhratsky, A. and H. Kettenmann, *Calcium signalling in glial cells.* Trends in neurosciences, 1996. **19**(8): p. 346-352.

18. Sontheimer, H., *Voltage-dependent ion channels in glial cells.* Glia, 1994. **11**(2): p. 156-172.

19. Huang, J., et al., *Electrical stimulation induces calcium-dependent release of NGF from cultured Schwann cells.* Glia, 2010. **58**(5): p. 622-631.

20. Kam, N.W.S., E. Jan, and N.A. Kotov, *Electrical stimulation of neural stem cells mediated by humanized carbon nanotube composite made with extracellular matrix protein.* Nano letters, 2008. **9**(1): p. 273-278.

21. Park, S.Y., et al., *Enhanced differentiation of human neural stem cells into neurons on graphene.* Advanced materials, 2011. **23**(36).

22. Vijaya, M., *Piezoelectric materials and devices: applications in engineering and medical sciences*2012: CRC Press.

23. Ribeiro, C., et al., *Piezoelectric polymers as biomaterials for tissue engineering applications.* Colloids and Surfaces B: Biointerfaces, 2015. **136**: p. 46-55.

24. Lee, Y.-S. and T.L. Arinzeh, *The influence of piezoelectric scaffolds on neural differentiation of human neural stem/progenitor cells.* Tissue Engineering Part A, 2012. **18**(19-20): p. 2063-2072.

25. Lee, Y.-S., G. Collins, and T.L. Arinzeh, *Neurite extension of primary neurons on electrospun piezoelectric scaffolds.* Acta biomaterialia, 2011. **7**(11): p. 3877-3886.

26. Wu, Y., et al., *Electroactive biodegradable polyurethane significantly enhanced Schwann cells myelin gene expression and neurotrophin secretion for peripheral nerve tissue engineering.* Biomaterials, 2016. **87**: p. 18-31.

27. Chew, S.Y., et al., *The effect of the alignment of electrospun fibrous scaffolds on Schwann cell maturation.* Biomaterials, 2008. **29**(6): p. 653-661.

28. Huang, J., et al., *Electrical regulation of Schwann cells using conductive polypyrrole/chitosan polymers.* Journal of biomedical materials research Part A, 2010. **93**(1): p. 164-174.

29. Sher, E., et al., *Physiopathology of neuronal voltage-operated calcium channels.* The FASEB Journal, 1991. **5**(12): p. 2677-2683.

30. Lev-Ram, V. and M. Ellisman, *Axonal activation-induced calcium transients in myelinating Schwann cells, sources, and mechanisms.* Journal of Neuroscience, 1995. **15**(4): p. 2628-2637.

31. Dulin, J.N. and P. Lu, *Bridging the injured spinal cord with neural stem cells.* Neural regeneration research, 2014. **9**(3): p. 229.

32. Pires, F., et al., *Neural stem cell differentiation by electrical stimulation using a cross-linked PEDOT substrate: expanding the use of biocompatible conjugated conductive polymers for neural tissue engineering.* Biochimica et Biophysica Acta (BBA)-General Subjects, 2015. **1850**(6): p. 1158-1168.

33. Turner, J.T., *Human neural stem cell differentiation and electrical stimulation on a novel single walled carbon nanotube-polymer composite*2013: Rutgers The State University of New Jersey-New Brunswick and University of Medicine and Dentistry of New Jersey.

34. Yang, F., et al., *Electrospinning of nano/micro scale poly (L-lactic acid) aligned fibers and their potential in neural tissue engineering.* Biomaterials, 2005. **26**(15): p. 2603-2610.

35. Li, M., et al., *Neuronal differentiation of C17. 2 neural stem cells induced by a natural flavonoid, baicalin.* ChemBioChem, 2011. **12**(3): p. 449-456.

36. Wang, Q., L. Yang, and Y. Wang, *Enhanced differentiation of neural stem cells to neurons and promotion of neurite outgrowth by oxygen–glucose deprivation.* International Journal of Developmental Neuroscience, 2015. **43**: p. 50-57.

37. Spitzer, N.C., *Electrical activity in early neuronal development.* Nature, 2006. **444**(7120): p. 707.

38. Chang, K.-A., et al., *Biphasic electrical currents stimulation promotes both proliferation and differentiation of fetal neural stem cells.* PLoS One, 2011. **6**(4): p. e18738.

39. Li, N., et al., *Three-dimensional graphene foam as a biocompatible and conductive scaffold for neural stem cells.* Scientific reports, 2013. **3**: p. 1604.

40. Leipzig, N.D. and M.S. Shoichet, *The effect of substrate stiffness on adult neural stem cell behavior.* Biomaterials, 2009. **30**(36): p. 6867-6878.

41. Hu, J., et al., *Repair of extended peripheral nerve lesions in rhesus monkeys using acellular allogenic nerve grafts implanted with autologous mesenchymal stem cells.* Experimental neurology, 2007. **204**(2): p. 658-666.

42. Michibata, H., et al., *Inhibition of mouse GPM6A expression leads to decreased differentiation of neurons derived from mouse embryonic stem cells.* Stem cells and development, 2008. **17**(4): p. 641-652.

43. Yu, W.-P., et al., *Embryonic expression of myelin genes: evidence for a focal source of oligodendrocyte precursors in the ventricular zone of the neural tube.* Neuron, 1994. **12**(6): p. 1353-1362.

44. Canoll, P.D., et al., *GGF/neuregulin is a neuronal signal that promotes the proliferation and survival and inhibits the differentiation of oligodendrocyte progenitors.* Neuron, 1996. **17**(2): p. 229-243.

45. Emery, B., *Regulation of oligodendrocyte differentiation and myelination.* Science, 2010. **330**(6005): p. 779-782.

CHAPTER 5. CONCLUSION

5.1 Summary

The work presented in this doctoral dissertation demonstrates a novel methodology enabling effective peripheral and central nerve regeneration by enhancing the functionality of neuronal and glial cells, as well as the differentiation of neural stem cells towards the three phenotypes of the CNS utilizing non-contact mechanical/electrical stimulation. Electrospinning technique to synthesize nanofibrous PVDF-TrFE, a biocompatiable, piezoelectric polymer, allowed for precise control the fiber morphology (i.e., diameter), structure (i.e., uni-directional alignment), and dimensions (i.e., scaffold thickness) to ultimately modulate the piezoelectric performance, as well as neuronal cellular behaviors. We developed a piezoelectric cell culture system to subject neural cells to electric potentials generated from the nanofibrous PVDF-TrFE scaffolds by non-contact mechanical stimulation. This system was utilized to determine the effects of mechanical/electrical stimulation on neuronal, glial, and neural stem cell behaviors. When PC12 cells, a neuronal cell type, were subjected to mechanical/electrical stimulation, it enhanced the neurite growth in the direction of the fiber alignment and increased the population of neurite bearing cells as compared to a static control. Alternatively, mechanical/electrical stimulation induced the production of a neurotrophic factor, NGF, from Schwann cells, a PNS glial cell. As well as enhancing functionality of these neural cells, mechanical/electrical stimulation induced the differentiation of neural

stem cells towards the three phenotypes of the central nervous system, including functionally active oligodendrocytes and astrocytes, CNS glial cells. Collectively, the induction of glial phenotyp differentiation and the enhancement of their functionality are expected to facilitate nerve regeneration.

5.2 Future directions

The results from these studies demonstrate the promising potential of using piezoelectric technologies to modulate cellular behavior *in vitro*. To further progress this work, future studies should include a non-piezoelectric PVDF control to decouple the effects of mechanical stimulation and electric stimulation. Mechanical stimulation has been reported to induce mechano-responsive ion channels of neuronal and Schwann cells which can initiate signaling cascades for nerve regeneration. Therefore, by decoupling the two stimulation will elucidate the true role of piezoelectricity has on neural cell types. Having a better understanding on these mechanisms will allow for further optimization of the system to induce specific functionality or differentiation of neural cells.

The functionality of the elongated neurites from PC12 cells or differentiated neurons from NSCs subjected to piezoelectrical stimulation need to be assessed to determine the translational efficacy of the engineered tissues. We can utilized the multi-electrode array (MEA) technology. The MEA can stimulate neural cells by transducing electrical currents by the ionic movement within the media. This ionic flux triggers the voltage-gate channels on the plasma membrane of the excitable cells to depolarize and

induce an action potential. To recording these electrical signal propagations, the electrodes on the MEA detect potential changes within the media by ions into electrical current.

Since we observed enhanced functional behavior of neuronal cells and Schwann cells by mechanical/electrical stimulation separately, a co-culture of the two cell types will determine if the piezoelectric cell culture system can enhance *in vitro* myelination by Schwann cells onto the existing neuronal cells. Myelin is an essential component of the PNS and CNS. Damages to the nerve by injuries/diseases has a detrimental effect on myelin. We can utilize this *in vitro* model can give us better understanding of the mechanism of myelination to potentially finding therapeutic interventions for treating demyelinating diseases by our piezoelectric culture system.

Currently, we are inducing mechanical/electrical stimulation by actuation of a vertical platform controlled by a subwoofer speaker. To have relevant translational usage, we must test the ability of external mechanical stimulation via a shockwave system to acoustically stimulate the piezoelectric neuroconduit to generate electrical potential through a medium similar to skin and muscle.

Ultimately, *in vivo* implantation of the neuroconduit will determine the efficacy of this piezoelectric material to facilitate neuronal and glial cell functionality to enhance the functional recovery of nerve damage with large gaps. This can be validated in a rat model by transecting a sciatic nerve to create a 15 mm gap. A hollow PVDF-TrFE conduit will be wrapped around the two nerve stumps and the application of shockwave pulses will be

transmitted to the injury site. We can utilize OCT technology to monitor the elongation of axons within the tube as well as myelination of the axons.

Appendix A. Polyaniline/poly(ε-caprolactone) composite electrospun nanofiber-based gas sensors: optimization of sensing properties by dopants and doping concentration

Abstract

Electrospinning was utilized to synthesize a polyaniline (PANI)/poly(□-caprolactone) (PCL) composite in the form of nanofibers to examine its gas sensing performance. Electrical conductivity of the composite nanofibers was tailored by secondary doping with protonic acids including hydrochloride (HCl) or camphorsulfonic acid (HCSA). FT-IR and diffuse reflectance UV-Vis spectroscopy were utilized to examine doping-dependent changes in the chemical structure and the protonation state of the nanofibers, respectively. The oxidation and protonation state of the composite nanofibers were shown to strongly depend on the doping agent and duration, demonstrating a simple way of controlling the electrical conductivity of the composite. PANI/PCL electrospun nanofibers having various electrical conductivities via varying dopants and doping concentrations, were configured to chemiresistors for sensing various analytes, including water vapor, NH_3, and NO_2. Secondary doping with Cl^- and CSA differentially affected sensing behaviours by having distinctive optimal sensitivities. Biphasic sensitivity with respect to electrical conductivity was observed, demonstrating a facile method to enhance gas sensitivity by optimizing

secondary doping. A balance between Debye length of the nanofibers and overall charge conduction may play an important role for modulating such an optimal sensitivity.

Keywords: electrospinning, gas sensor, composite nanofibers, polyaniline, poly□□□caprolactone)

1. Introduction

The increasing need for sensors in various applications ranging from agriculture, automotive industry, medical diagnosis and public/national security demands the development of sensitive, reliable, fast responsive, and inexpensive chemical and biological sensors [1]. Solid-state sensors have been sought after due to their ability to alter their electrical properties (*e.g.,* electrical resistance and capacitance) upon exposure to analytes. Among the variety of sensing materials used for solid-state sensors, conducting polymers (CPs) such as polyaniline (PANI) [2], polypyrrole (PPy) [3], or polythiophene (PT) [4] have shown a promising potential as gas sensing materials because of their excellent physical, chemical, electrical and material properties including tunable electrical behaviour by dopants and doping levels, diverse monomer chemistry, and ease of functionalization [5]. More importantly, their low operating temperature and power consumption are enticing to configure them for various types of sensors such as amperometric and chemiresistive/conductometric devices [5].

CPs have some physical and chemical limitations, presenting difficulties in manufacturing [6]. In this regard, various polymer hosts have been used to improve processability, resulting in a composite that combines the excellent electrical properties of the CPs with the robust mechanical properties of the polymer host [6]. In addition to enhanced processability, introduction of polymer hosts provide an opportunity to tailor the gas sensing performance by optimizing the ratio of CPs dispersed in the host polymer

[7]. The advantages of these composites include tunable analyte selectivity, lower detection limits, fast response time, and improved environmental stability [7].

One-dimensional (1-D) nanostructures, such as nanowires, nanorods, nanobelts, and nanotubes, have emerged as attractive platforms for the fabrication of these gas sensors. They exhibit properties that their bulk material counterparts lack, such as a large surface-to-volume ratio for greater interaction between surface and analyte, two dimensional diffusion, and efficient electron transport to generate fast responses and quick recovery [8-11]. Fabrication strategies, such as solution or vapor-phase approaches [12], template-directed methods [13], solvothermal synthesis [14], and self-assembly methods [15] have been employed to produce 1-D CP composite nanostructures. Although these methods enable tight dimensional control, they typically require multi-step fabrication resulting in a low manufacturability. In comparison, electrospinning provides an alternative approach to mass-produce ultra-long 1-D composite nanofibers in a facile and cost-effective manner [16]. The feasibility of tuning the properties of the gas sensor by altering electrospinning parameters that control fiber dimensions and composition and by introducing secondary protonic dopants that modulate electrical properties, makes electrospinning an attractive method for the development of a highly sensitive 1-D nanostructured solid-state sensor towards various gases.

In this study, PANI/poly□□□caprolactone) (PCL) composite nanofiber mats were bulk-synthesized and configured in a chemiresistor for gas sensing studies. Because of its insolubility in water, PCL was selected as the insulating polymer host to provide structural

stability in humid air. The composite offers a competent platform to investigate the effects of secondary protonic doping to enhance the sensitivity of electrospun PANI/PCL composite nanofibers.

2. Experimental Methods

2.1. Synthesis of PANI/PCL composite nanofibers

A 5 wt. % solution of PCL (M_w = 65,000, Sigma-Aldrich, St. Louis, MO) was dissolved in 1,1,1,3,3,3-hexafluoro-2-propanol (HFIP) (Oakwood Products, Inc., Indianapolis, IN). PANI (3 mg/ml)- camphorsulfonic acid (HCSA, 3 mg/ml) solution was prepared by first adding (1R)-(–)-10-camphorsulfonic acid (Sigma-Aldrich, St. Louis, MO) in HFIP followed by rigorous stirring at 1,200 rpm to fully dissolve HCSA. Then, PANI in the emeraldine base form (M_w = 100,000, Sigma-Aldrich) was dispersed into the solution. The mixed solution was sonicated for 5 min and stirred at 1,200 rpm for 5 min at room temperature. The sonication/stirring process was repeated 4 times, and the solution was stirred for 4 hours in order to further disperse PANI. Subsequently, the PANI-HCSA solution was filtered with a 0.2 □m pore size membrane filter (Whatman, GE Healthcare Life Sciences, NJ) by vacuum filtration to remove undispersed particles. The filtered PANI was mixed with the PCL solution at a 4:1 volume ratio.

To synthesize nanofibers, the PANI/PCL solution was electrospun using a high voltage D.C. power supply (Glassman High Voltage, NJ) at -19 kV with a flow rate of 0.4

mL/hr and a 30 cm tip to plane collector distance to produce an approximately 2 □m-thick fiber mat. The thickness of the fiber mat was controlled by adjusting the deposition time.

2.2. Secondary doping by hydrochloric acid (HCl) and HCSA

To investigate the effects of dopants and doping concentration on the electrical resistivity and sensing performance of PANI/PCL composite nanofiber, the fiber mats were separately incubated with a solution of 1M HCl, 1M HCSA, or 1M NaOH for various durations ranging from 1 min to 12 hours. After the doping process, the solution was aspirated out and the fiber mats were rinsed with DI water, followed by air drying for 1 hour. The fiber mats were subsequently characterized for its chemical and electrical properties.

2.3. Characterization of PANI solution and PANI/PCL nanofibers

To determine PANI loss during the filtration process, the PANI concentration after filtration was quantified using a UV-Vis spectrometer (DU 800, Beckman Coulter, CA). Various concentrations of unfiltered PANI solution were prepared, and their absorbance spectra were obtained from the UV-Vis spectrometer by scanning the solutions at the wavelength ranging from 200 to 1100 nm to generate a calibration curve. The absorption spectrum of the filtered solution was compared to the calibration curve to quantify PANI content.

Fourier-transform infrared spectroscopy using the Equinox 55 FT-IR (Bruker, Billerica, MA) was utilized to characterize the chemical structures of the as-prepared and doped PANI/PCL composite nanofibers. The mat was placed on a highly polished NaCl substrate and measured with 32 scans at a resolution of 0.5 cm^{-1}. The transmission spectra were determined in the wavenumber range between 600 and 3000 cm^{-1}.

In order to determine doping states, diffuse reflectance spectroscopy was used to measure the absorbance of the as-prepared, secondary doped PANI/PCL composite, and pure PCL nanofiber mats using a UV-Vis Spectrometer (Evolution 300, Thermo Scientific, Waltham, MA). The absorbance spectra were measured in the wavelength range between 190 and 1100 nm.

The morphology and fiber diameter of the fiber mats were characterized using scanning electron microscopy (SEM, Nova NanoSEM450, FEI, Hillsboro, Oregon). The composite nanofibers were sputter-coated with platinum-palladium to visualize under SEM.

2.4. Characterization of electrical properties

To determine the electrical property of nanofibers, a 4 mm x 6 mm sized strip of nanofiber mat with a controlled thickness ~2 □m was placed onto 500 □m-thick oxidized silicon substrate. Using an aluminum stencil with a gap size of 1 mm x 80 mm, gold microelectrodes with the thickness of ~300 nm were deposited onto the sample by sputtering using the EMS 575X sputter (Electron Microscopy Science, Hatfield, PA). The

electrical characterization of PANI/PCL fiber mat was obtained from probing source and drain microelectrodes by sweeping the potential of -0.5 V to 0.5 V to generate I-V curves using a source-meter (Kiethley 2363, Cleveland, OH). The electrical conductivity of PANI/PCL composite nanofibers was determined by normalizing it to the thickness of the sample.

2.5. Device fabrication

The sensing device was fabricated and connected to the sensing system as previously reported [17]. Briefly, the fiber mat integrated with gold microelectrodes was mounted onto a sample holder and enclosed by a glass chamber with the volume of 3.15 cm^3 with a gas inlet and outlet ports for gas flow (figure 1). The chip was then clipped to a Kiethly source-meter to establish an electrical connection.

2.5. Gas sensing measurement

The doped PANI/PCL nanofibers were examined against various gases including water (H_2O) vapor, ammonia (NH_3), and nitrogen dioxide (NO_2) at room temperature with a custom built gas sensing system with the Alicat mass flow controllers (MFC) operated by Labview as described elsewhere [8]. Prior to exposure to various concentrations of analyte, dry air was introduced over the sensor for an hour to establish the sensor baseline. Afterward, the sensor was subjected to various concentrations of analyte, followed by a recovery period with dry air in a step-wise manner. All the analytes were

thoroughly mixed with carrier gas (dry air) before introduced to the sensor. Water-saturated dry air was prepared by bubbling the carrier gas through water. This was followed by varying the mixing ratio of dry air and water-saturated air to produce humidity-controlled air. The volumetric flow rate was kept constant to 200 standard cubic centimeters per minute (sccm) while various percentages of saturation were tested. The ratio of the two MFCs was used to control the exposure concentration.

3. Results and discussion

3.1. Synthesis of PANI/PCL composite nanofibers and their material characterization

Homogeneous incorporation of PANI into the electrospun blend PANI/PCL nanofibers is essential to prevent the bead formation of aggregated PANI particles along the nanofibers, which may deteriorate electrical and sensing properties [18]. Based on our preliminary studies, HFIP was selected as a common solvent because of its appropriate vapor pressure at room temperature that enables electrospinning nanofibers less than 100 nm in fiber diameter [19]. Additionally, HFIP may enhance the electrical conductivity of the composite nanofibers by inducing linear extension of PANI [20]. However, the emeraldine base of PANI has low solubility in organic solvents including HFIP [21]. Thus, HCSA was used to protonate the emeraldine base of PANI, making it a polyelectrolyte (or well-dispersion of PANI) in HFIP to enhance the uniform dispersion of PANI [22]. This dispersed PANI solution was then vacuum-filtered to remove non-dispersed PANI particles.

Due to possible changes of PANI content during filtration, the filtered PANI solution was quantified by UV-Vis spectroscopy. Various concentrations of unfiltered PANI solution were prepared and their UV-Vis absorption spectra were examined (figure S1). The absorption peak at wavelength of 300 nm that represents □□□□ transition of the benzenoid ring [23], was utilized to generate a calibration curve for determination of the final PANI content [24]. The final concentration of filtered PANI solution was estimated to be ~5.8 mg/ml, exceeding the initial PANI content of 3 mg/ml. The increase in PANI content after filtration may result from evaporation of HFIP during the vacuum filtration process. Multiple experiments confirmed the content change is consistent among experiments. The filtered PANI solution was mixed with PCL solution and then electrospun as described earlier. Figure 2(a) shows the microstructure of electrospun PANI/PCL composite nanofibers examined by SEM. The nanofibers are randomly oriented with relatively uniform size having a typical cylindrical morphology. A quantitative analysis of the fibers indicates the tightly controlled average fiber diameter at 83 ± 16 nm (figure 2(b)).

Prior to examining the structural and oxidation level changes of the PANI/PCL composite electrospun nanofibers, the surface of the nanofibers was examined for morphological changes after protonic acid doping by SEM (figure 3). The nanofibers maintained its morphology after 12 hours of doping treatment with HCl and HCSA.

In order to examine the effects of doping on the composite, FT-IR and diffuse reflectance UV-Vis spectroscopy were performed. The structure and the oxidation level of PANI/PCL composite electrospun nanofibers were analyzed after doping with protonic acids (*i.e.,* HCl and HCSA) and de-doping with a base (*i.e.,* NaOH) (figure 4). Figure 4(a) displays the FT-IR absorption spectra of de-doped, as-electrospun, Cl^- and CSA doped PANI/PCL nanofibers. The FT-IR characteristic absorption bands at 2949, 2866, and 1730 cm^{-1} are specific to asymmetric CH_2, symmetric CH_2 and carbonyl stretching of PCL, respectively [25]. The other bands at 825, 1161, 1297, 1493, and 1586 cm^{-1} are specific to C-H bending vibration of benzene ring, vibration mode of quinoid ring, stretching vibration of C-N, stretching vibration of N-benzenoid ring and stretching vibration of N-quinoid ring of PANI, respectively [26]. To determine changes in the levels of protonation by acidic doping and basic de-doping, the ratio of the peak area intensity between the benzenoid (protonated PANI) and quinoid (undoped PANI) rings at 1493 and 1586 cm^{-1} in the FT-IR spectra, respectively, was quantified [27]. The ratio of as-electrospun PANI/PCL is 0.91:1. This is close to the intrinsic emeraldine salt of PANI which has 1:1 ratio between benzenoid and quinoid rings [28]. De-doping the sample with NaOH decreased the value to 0.78:1, inferring that the benzenoid structure was deprotonated to quinoid rings after the treatment. Conversely, the increasing ratio values to 1.04:1 and 1.28:1 by doping with Cl^- and CSA for 5 min, respectively, indicate that PANI was further protonated. The smaller value obtained from Cl^- doping indicates slower protonation rate than that of CSA.

In addition to the PANI/PCL structural changes observed by FT-IR spectra, the protonation states of PANI/PCL composite nanofibers upon de/doping was further closely examined by diffuse reflectance UV-Vis spectroscopy. Figure 4(b) shows the diffuse reflectance UV-Vis spectra of 1 min de-doped in NaOH, as-electrospun, 1 min or 5 min doped with HCl, 1 or 5 min doped with HCSA PANI/PCL samples, and pure PCL sample along with their representative fiber colours. A colour change from green to blue was observed in de-doped PANI/PCL nanofibers in 1M NaOH, whereas that of protonic acids (*i.e.,* HCL and HCSA) doping turned the green colour lighter proportional to doping duration. These colour changes were closely related to the protonation states of the PANI/PCL characterized by the diffuse reflectance spectra in figure 2(b) [23]. The absorbance peak at wavelength of 206 nm is specific to PCL as shown by pure PCL sample [29]. Two absorbance peaks in de-doped PANI/PCL in NaOH appear at the wavelengths of 325 and 605 nm, respectively, denote the benzenoid and quinoid structures which are characteristics of PANI in emeraldine base form [24]. The larger absorbance peak at wavelength of 605 nm as compared to rest of the samples, indicates more quinoid contents, similarly observed in the FT-IR spectrum of de-doped PANI/PCL. As-electrospun PANI/PCL nanofibers exhibited a significant decrease in the peak intensity at 605 nm, indicating the conversion of quinoid rings to its polaron state [24]. A peak at 425 nm that was missing in the de-doped specimen indicates the degree of protonation resulting in bipolaron formation [30]. Upon doping with protonic acids, either HCl or HCSA, the peak at 605 nm vanished, and a free carrier tail became visible at 850 nm [31]. This

characteristic is consistent with the relaxation of the PANI chain as its typically coiled structure becomes more linearly extended by the reduction of □ defects that cause the compact structure [32]. This uncoiling process induces the delocalization of electrons in the polaron band of the PANI chain [24]. Interestingly, CSA doped nanofibers exhibit higher absorbance intensity of a free carrier tail than the Cl^- doped samples, indicating greater efficiency of doping. The greater intensity also is observed when the nanofibers were doped for a longer duration. This observation, combined with the FT-IR spectroscopy data, demonstrates that protonation of PANI/PCL composite strongly depends on the doping agent as well as doping duration.

3.2. Electrical properties of electrospun PANI/PCL composite nanofibers

After chemical characterization, the electrical properties and sensing performance of PANI/PCL nanofibers were investigated. The electrical conductivity of nanofibers was obtained from I-V characteristics generated by sweeping the voltage between -0.5 to 0.5 V across source and drain electrodes. Figure 5(a) and 5(b) show the typical I-V curves of Cl^- and CSA doped PANI/PCL nanofibers, respectively, as compared to that of as-prepared PANI/PCL nanofibers. The I-V curve of as-prepared nanofibers has a smaller slope with non-linear and asymmetric, indicating its insulating electrical property with Schottky contact prior to doping [33]. This observation is consistent with the high quinoid content within PANI/PCL nanofibers observed from its FT-IR and diffuse reflectance UV-Vis spectra. Electrical current increased after doping with Cl^- and CSA. The electrical

characterization also showed a linear I-V relation, a characteristic of Ohmic contact, indicating that the devices exhibit a good electrical contact between the nanofibers and the gold microelectrodes [34].

The electrical conductivity of doped PANI/PCL nanofibers was determined from slopes of I-V curves normalized by the geometry of the nanofiber mats after various treatments (figure 5(c)). The as-prepared composite nanofibers exhibited an electrical conductivity of ~$9X10^{-7}$ S/cm. After doping in 1 M HCl for 5 min, the electrical conductivity increased to ~$1X10^{-5}$ S/cm, and further increased to ~$5X10^{-4}$ S/cm after 10 min. In contrast, CSA was a more effective dopant as the electrical conductivity became ~$8X10^{-2}$ S/cm after 5 min doping. This substantiates dopant-dependent electrical property of PANI, corresponding to the observations from UV-Vis and diffuse reflectance spectroscopy. Electrical conductivities of PANI/PCL nanofibers doped with both Cl^- and CSA were saturated after certain thresholds, indicating that the extent of doping is diffusion controlled [35].

3.3. Gas sensing properties of electrospun PANI/PCL composite nanofibers

Various analytes including H_2O vapor, NH_3, and NO_2 were examined. Prior to exposure to various concentrations of analyte, dry air was introduced over the sensor for an hour to establish the sensor baseline. Afterward, the sensor was subjected to various concentrations of analyte, followed by a recovery period with dry air in a step-wise manner. The normalized change in electrical resistance ($\Delta R/R_o$) and sensitivity of Cl^- and

CSA doped PANI/PCL nanofibers plotted against different concentrations of various gas are shown in figures 6 and 7. The R_o and ΔR were defined as the initial base-line resistance and change in resistance upon subjected to analytes, respectively.

Figure 6(a)-(c) and 6(d)-(f) show the $\Delta R/R_o$ responses of Cl^- and CSA doped PANI/PCL nanofibers, respectively, to H_2O vapor, NH_3 and NO_2. During H_2O exposure, the sensors show negative $\Delta R/R_o$ responses as compared to the positive $\Delta R/R_o$ responses seen in NH_3 and NO_2 sensing. These sensing behaviours may result from different sensing mechanism depending on analyte interactions with PANI/PCL electrospun nanofibers. The decrease in electrical resistance of PANI/PCL nanofibers upon exposure to H_2O vapor may be attributed to proton exchange-assisted conduction of electrons (PEACE) mechanism [36]. The protonating agents, including H_2O, protonate the imine group and forms polarons, allowing free movement of charge carriers along the PANI backbone. On the other hand, a deprotonating agent such as NH_3 interacts with protons on the PANI backbone and yields ammonium ion, NH_4^+ [2]. This phenomenon reduces free charge carriers, causing an increase in electrical resistance of PANI/PCL nanofibers. Additionally, the sensors show a recovery in $\Delta R/R_o$ responses during pure dry air flow in both H_2O vapor and NH_3 due to their easy adsorption and desorption process from the PANI surface [37]. Although the sensors also display increases in $\Delta R/R_o$ in response to NO_2, the mechanism of electrical resistance changes differs from that of NH_3 sensing. Unlike NH_3, NO_2, a reducing gas, oxidizes emeraldine salt by removing electrons from the aromatic rings [38]. As a result, no recovery is observed due to strong interaction between NO_2 and PANI,

which makes the desorption rate of NO_2 become much slower, instigating a poisoning effect [38].

Figure 7(a)-(c) and 7(d)-(f) show the effect of dopant and doping concentration on the sensitivity of sensors. The data demonstrate that the extent of gas sensor sensitivity can be tailored by protonic doping that determines the electrical conductivity of PANI/PCL nanofibers. Interestingly, it was observed that the sensitivity change increased with increasing gas concentration, but at a fixed gas concentration, there was not a linear relationship between sensitivity change and the electrical conductivity of sensor. For closer examination, sensitivity changes per ppm with respect to different electrical conductivity for various gases were plotted (figure 8). The semi-log plots of the sensitivity are shown as a function of the electrical conductivity. The sensitivity was determined from the slope of the sensor response ($\Delta R/R_o$) plotted against the gas concentration in the linear region (figure 7). Sensitivity values that have been reported using PANI blends are 0.12 %/percent saturation for H_2O vapor [39], 4.23 %/ppm for NH_3 [40], and 19.91 %/ppm for NO_2 [41]. In this study, the Cl^- doped PANI/PCL nanofibrous composite exhibited sensitivities of 1.36 % for H_2O vapor, 13.75 and 70.31 %/ppm for NH_3 and NO_2, respectively, while CSA doped fiber mats showed sensitivities of 0.76 % for H_2O vapor, 21.43 and 54.41 %/ppm for NH_3 and NO_2, respectively, which is shown to be greater than literature values for PANI composites [39-48]. As shown in figure 8, the device shows biphasic sensitivity in the conductivity range of 10^{-5} to 10^{-3} S/cm, with the exception of CSA doped PANI/PCL upon exposure to NH_3.

The above observation is significant in that it demonstrates a means to optimize the sensitivity of an electrospun chemiresistive sensor with a simple secondary doping process (dopant and doping duration) without altering the composition of materials, which may affect processability and mechanical stability. The mechanisms underlying how doping modulates the optimum sensitivity are still elusive. One possible explanation could be a balance between Debye screening length and overall charge conduction. Sensitivity of chemiresistive sensor is proportional to Debye length, a scale that describes the alteration of conductance by an adsorbed charged molecule [11, 49]. Debye length is inversely related to charge carrier density, thus electrical conductivity as shown in our previous report [11]. In this study, we observed that the sensitivity increases when the electrical conductivity decreases (*i.e.,* less doped) above a threshold (optimum electrical conductivity yielding a maximum sensitivity). However, below this threshold, sensitivity reduces by lower electrical conductivity due to decrease in overall charge conduction. The discrepancies in the optimal electrical conductivities for the maximum sensitivity depending on dopants (*i.e.,* Cl^- and CSA), are probably due to their differences in hydrophilicity affecting responses to H_2O vapor and molecular size influencing molecular structures [50]. However, how these individual attributes collectively affect overall sensing performance needs to be further investigated. Nevertheless, we demonstrated that secondary doping significantly impacts the sensing performance of electrospun composite nanofibers.

4. Conclusion

In this study, we synthesized a sensitive PANI/PCL composite nanofibrous sensor using electrospinning and characterized its gas sensing performance. The electrical conductivity of this 1-D nanostructured sensor was further tuned by secondary protonic doping with Cl^- and CSA. More significantly, we demonstrated that optimal sensitivities toward H_2O vapor, NH_3, and NO_2 can be achieved by optimizing doping, where dopant- and doping duration-dependent biphasic sensitivity were observed.

5. Acknowledgement

We greatly acknowledge the financial support from KIMS Academy Laboratory Program.

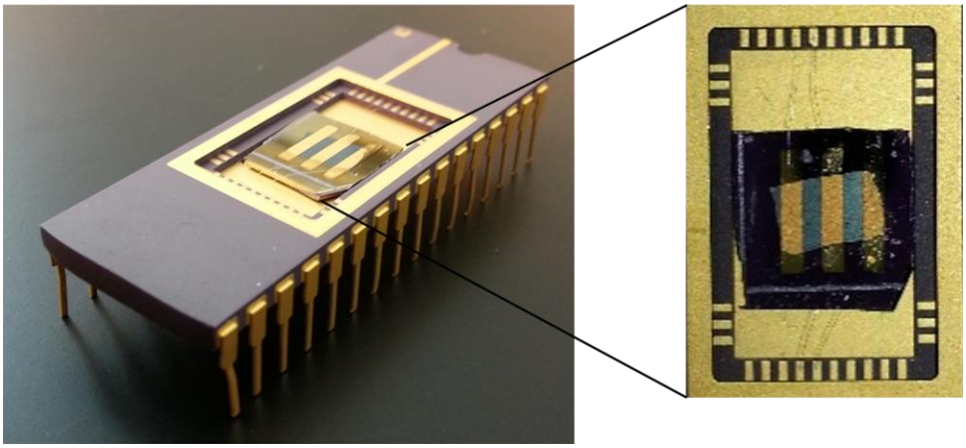

Figure A.1. A representative picture of gas sensor.

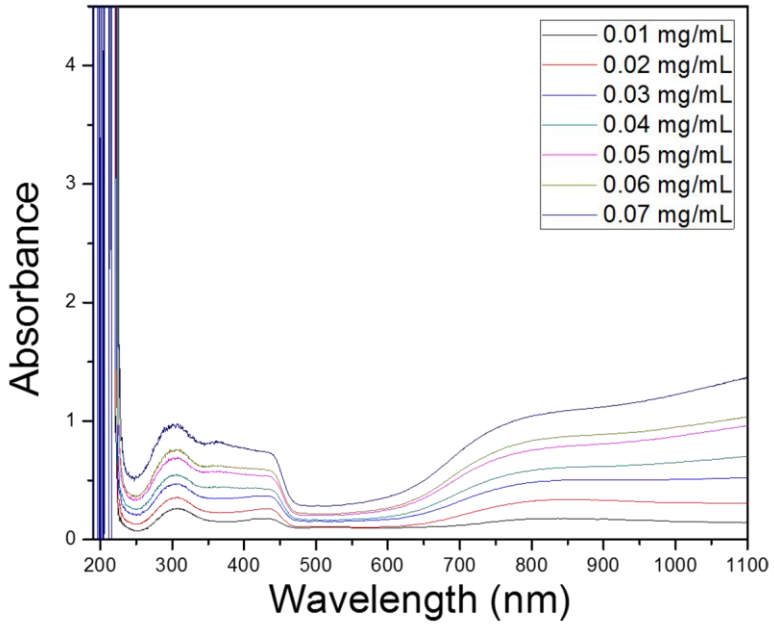

Figure A.2. Absorption spectra of PANI dispersion and their changes over concentration.

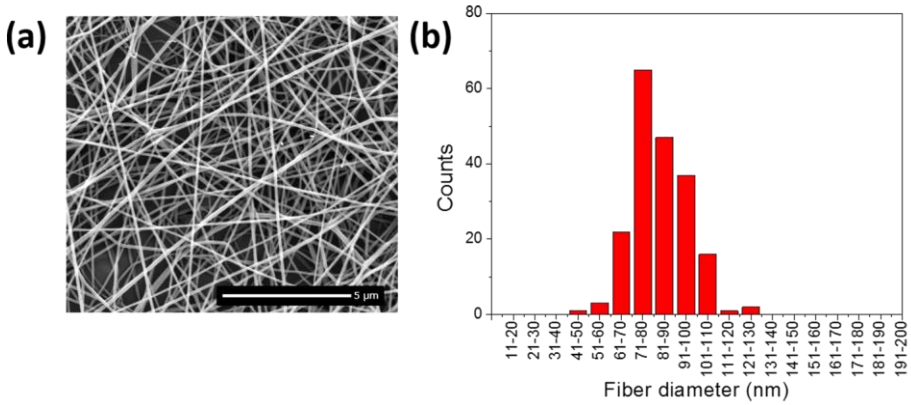

Figure A.3. Morphological characterization of as electrospun PANI/PCL composite nanofibers. (a) A representative scanning electron microscopy (SEM) image and (b) fiber diameter distribution.

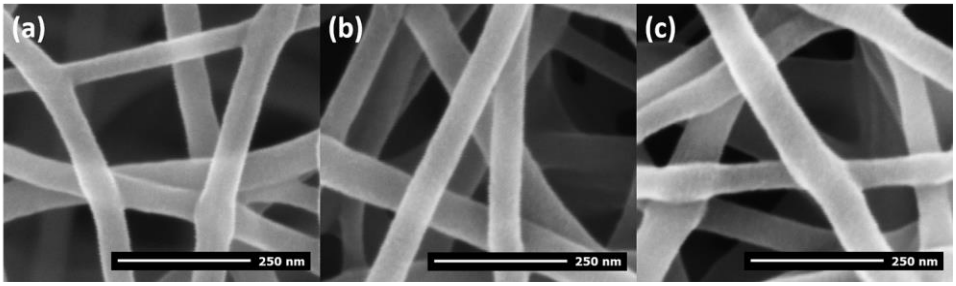

Figure A.4. Surface morphological characterization of electrospun PANI/PCL composite nanofibers (a) as prepared, (b) after Cl^- doping, and (c) after CSA doping.

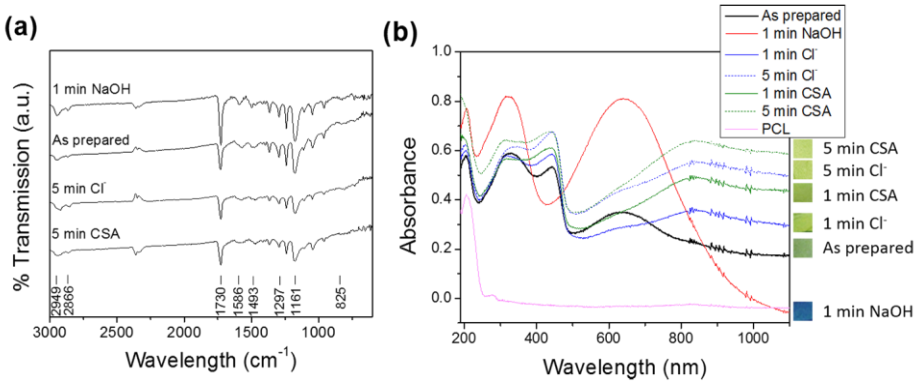

Figure A.5. Chemical characterization of PANI/PCL fiber mats with various doping agents and time using (a) FT-IR and (b) diffuse reflectance UV-Vis spectroscopy. Insets in (b) show representative color changes of the samples depending on doping agent and time.

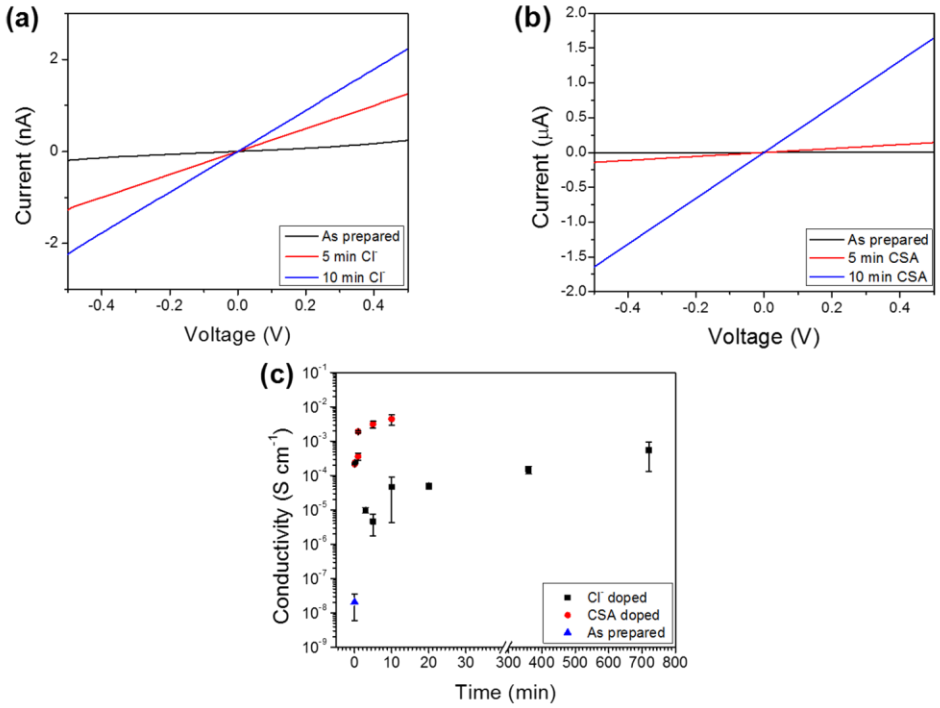

Figure A.6. I-V plots of (a) Cl^- and (b) CSA-doped electospun PANI/PCL composites. (c) Conductivity of Cl^- or CSA-doped PANI/PCL composite sensor is plotted as a function of doping time.

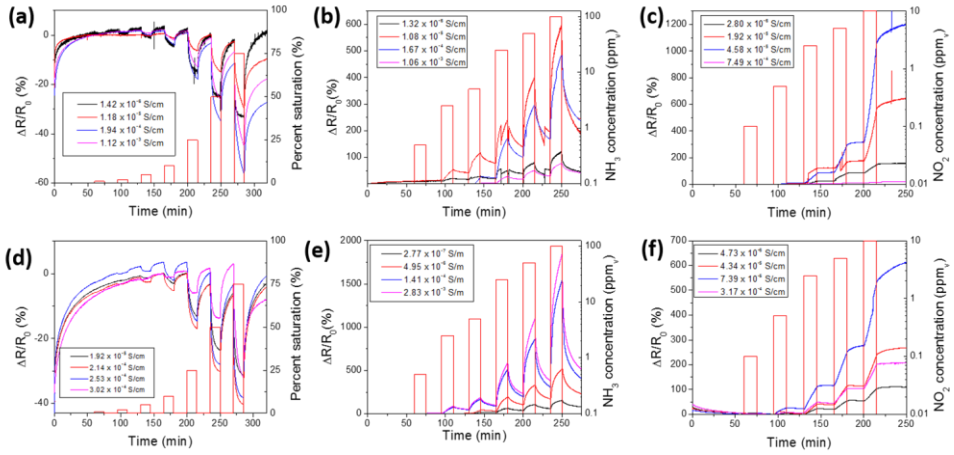

Figure A.7. Transient sensing profiles of ((a) – (c)) Cl^- and ((d) – (f)) CSA-doped electrospun PANI/PCL composite sensors at various as-fabricated conductivities in response to various concentrations of ((a) and (d)) H_2O vapor, ((b) and (e)) NH_3, and ((c) and (f)) NO_2.

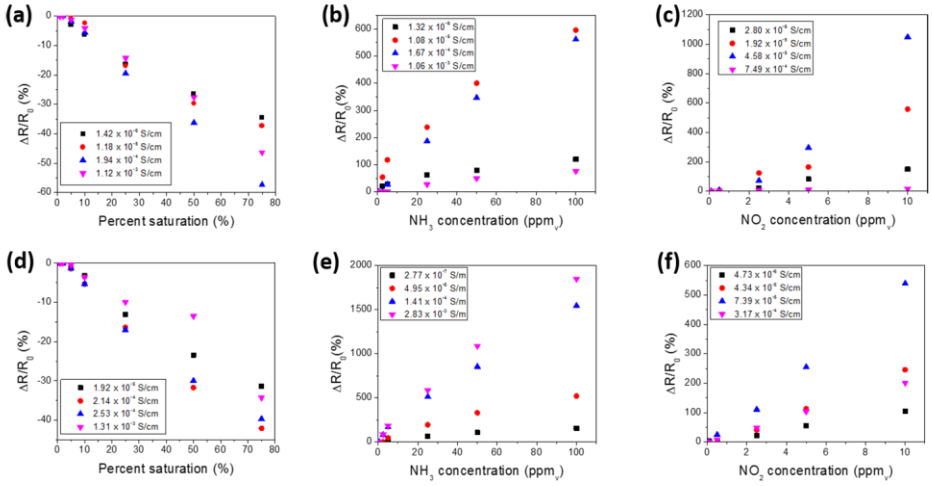

Figure A.8. Normalized responses of (a, b, and c) Cl^- and (d, e, and f) CSA-doped electrospun PANI/PCL composite sensors at various as-fabricated conductivities in response to various concentrations of (a and d) H_2O vapor, (b and e) NH_3, and (c and f) NO_2.

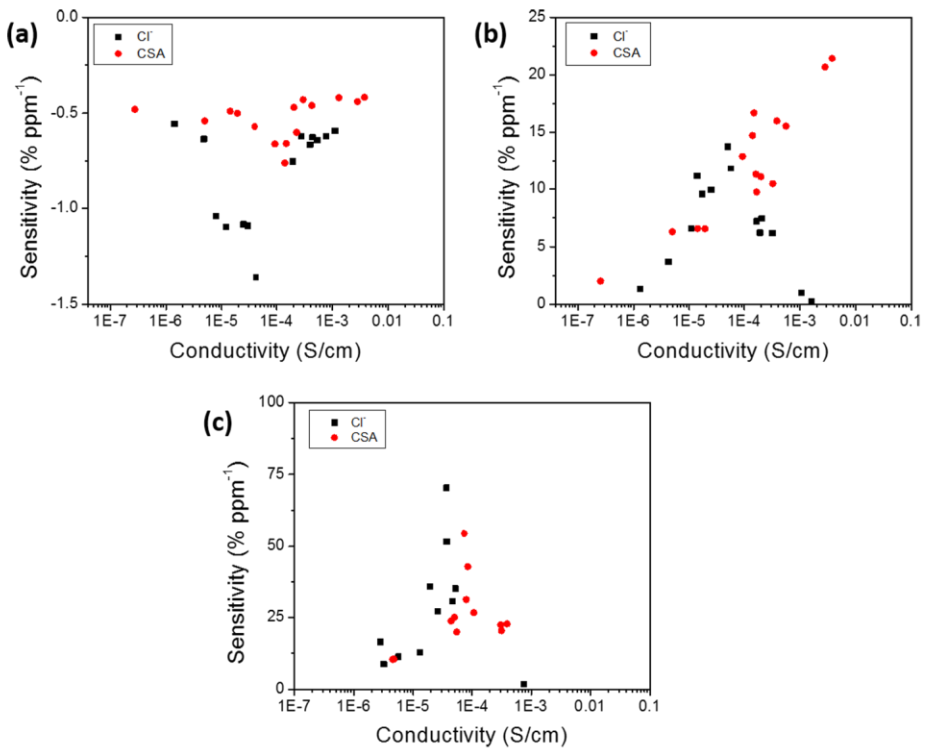

Figure A.9. Sensitivity of Cl^- or CSA-doped electrospun PANI/PCL composite sensors at various as-fabricated conductivities to (a) H_2O vapor, (b) NH_3, and (c) NO_2.

Reference

1. Kolmakov, A. and M. Moskovits, *Chemical sensing and catalysis by one-dimensional metal-oxide nanostructures.* Annual Review of Materials Research, 2004. 34: p. 151-180.

2. Virji, S., et al., *Polyaniline nanofiber gas sensors: Examination of response mechanisms.* Nano Letters, 2004. 4(3): p. 491-496.

3. Cabala, R., V. Meister, and K. Potje-Kamloth, *Effect of competitive doping on sensing properties of polypyrrole.* Journal of the Chemical Society-Faraday Transactions, 1997. 93(1): p. 131-137.

4. Bai, H. and G.Q. Shi, *Gas sensors based on conducting polymers.* Sensors, 2007. 7(3): p. 267-307.

5. Janata, J. and M. Josowicz, *Conducting polymers in electronic chemical sensors.* Nat Mater, 2003. 2(1): p. 19-24.

6. Strumpler, R. and J. Glatz-Reichenbach, *Conducting Polymer Composites.* Journal of Electroceramics, 1999. 3(4): p. 329-346.

7. Hatchett, D.W. and M. Josowicz, *Composites of intrinsically conducting polymers as sensing nanomaterials.* Chemical Reviews, 2008. 108(2): p. 746-769.

8. Sandra , C.H., et al., *Single Polypyrrole Nanowire Ammonia Gas Sensor.* Electroanalysis, 2007. 19(19-20): p. 2125-2130.

9. Hangarter, C.M., et al., *Tuning the gas sensing performance of single PEDOT nanowire devices.* Analyst, 2011. 136(11): p. 2350-2358.

10. Hangarter, C.M., et al., *Conducting polymer nanowires for chemiresistive and FET-based bio/chemical sensors.* Journal of Materials Chemistry, 2010. 20(16): p. 3131-3140.

11. Chartuprayoon, N., et al., *Wafer-Scale Fabrication of Single Polypyrrole Nanoribbon-Based Ammonia Sensor.* The Journal of Physical Chemistry C, 2010. 114(25): p. 11103-11108.

12. Wagner, R. and W. Ellis, *Vapor-liquid-solid mechanism of single crystal growth.* Applied Physics Letters, 1964. 4(5): p. 89-90.

13. Tran, H.D., D. Li, and R.B. Kaner, *One-Dimensional Conducting Polymer Nanostructures: Bulk Synthesis and Applications.* Advanced Materials, 2009. 21(14-15): p. 1487-1499.

14. Zhang, X., et al., *The first one-dimensional manganese polymer containing 4,5-dicarboxyimidazole: solvothermal synthesis, crystal structure and magnetic behavior of [Mn(phen)(Hdcbi)]$_n$ (H_3dcbi=4,5-dicarboxyimidazole, phen=1,10-phenanthroline).* Inorganic Chemistry Communications, 2004. 7(5): p. 662-665.

15. Palmer, L.C. and S.I. Stupp, *Molecular Self-Assembly into One-Dimensional Nanostructures.* Accounts of Chemical Research, 2008. 41(12): p. 1674-1684.

16. Huang, Z.M., et al., *A review on polymer nanofibers by electrospinning and their applications in nanocomposites.* Composites Science and Technology, 2003. 63(15): p. 2223-2253.

17. Heng, C.S., et al., *Metal nanoparticles and DNA co-functionalized single-walled carbon nanotube gas sensors.* Nanotechnology, 2013. 24(50): p. 505502.

18. Dong, H., et al., *Polyaniline/poly(methyl methacrylate) coaxial fibers: The fabrication and effects of the solution properties on the morphology of electrospun core fibers.* Journal of Polymer Science Part B: Polymer Physics, 2004. 42(21): p. 3934-3942.

19. Fong, H., et al., *Generation of electrospun fibers of nylon 6 and nylon 6-montmorillonite nanocomposite.* Polymer, 2002. 43(3): p. 775-780.

20. Hopkins, A.R., P.G. Rasmussen, and R.A. Basheer, *Characterization of solution and solid state properties of undoped and doped polyanilines processed from hexafluoro-2-propanol.* Macromolecules, 1996. 29(24): p. 7838-7846.

21. Kulszewicz-Bajer, I., et al., *Protonation of Polyaniline in Hexafluoro-2-propanol. Spectroscopic Investigation.* Macromolecules, 1997. 30(23): p. 7091-7095.

22. Jeong, S.I., et al., *Development of Electroactive and Elastic Nanofibers that contain Polyaniline and Poly(L-lactide-co-ε-caprolactone) for the Control of Cell Adhesion.* Macromolecular Bioscience, 2008. 8(7): p. 627-637.

23. Stejskal, J., P. Kratochvíl, and N. Radhakrishnan, *Polyaniline dispersions 2. UV—Vis absorption spectra.* Synthetic Metals, 1993. 61(3): p. 225-231.

24. Zheng, W., et al., *The Molecular Conformation of Non-Doped Polyaniline and its Effect on the Properties of Doped Polyaniline.* MRS Online Proceedings Library, 1995. 413: p. 413-535.

25. Elzein, T., et al., *FTIR study of polycaprolactone chain organization at interfaces.* Journal of Colloid and Interface Science, 2004. 273(2): p. 381-387.

26. Lijuan, Z. and W. Meixiang, *Synthesis and characterization of self-assembled polyaniline nanotubes doped with D-10-camphorsulfonic acid.* Nanotechnology, 2002. 13(6): p. 750.

27. Yelil Arasi, A., et al., *The structural properties of Poly(aniline)—Analysis via FTIR spectroscopy.* Spectrochimica Acta Part A: Molecular and Biomolecular Spectroscopy, 2009. 74(5): p. 1229-1234.

28. MacDiarmid, A.G. and A.J. Epstein, *Polyanilines: a novel class of conducting polymers.* Faraday Discussions of the Chemical Society, 1989. 88(0): p. 317-332.

29. Martins-Franchetti, S., et al., *Structural and morphological changes in Poly(caprolactone)/poly(vinyl chloride) blends caused by UV irradiation.* Journal of Materials Science, 2008. 43(3): p. 1063-1069.

30. Huang, W.S. and A.G. MacDiarmid, *Optical properties of polyaniline.* Polymer, 1993. 34(9): p. 1833-1845.

31. Min, Y., et al., *Vapor phase "secondary doping" of polyaniline.* Synthetic Metals, 1995. 69(1–3): p. 159-160.

32. MacDiarmid, A.G. and A.J. Epstein, *Secondary Doping in Polyaniline.* Synthetic Metals, 1995. 69(1-3): p. 85-92.

33. Chakrabarty, R.K., K.K. Bardhan, and A. Basu, *Nonlinear I-V characteristics near the percolation threshold.* Physical Review B, 1991. 44(13): p. 6773-6779.

34. Ramanathan, K., et al., *Individually Addressable Conducting Polymer Nanowires Array.* Nano Letters, 2004. 4(7): p. 1237-1239.

35. Sengupta, P.P., S. Barik, and B. Adhikari, *Polyaniline as a gas-sensor material.* Materials and Manufacturing Processes, 2006. 21(3): p. 263-270.

36. Ting, Z., et al., *A gas nanosensor unaffected by humidity.* Nanotechnology, 2009. 20(25): p. 255501.

37. Nicolas-Debarnot, D. and F. Poncin-Epaillard, *Polyaniline as a new sensitive layer for gas sensors.* Analytica Chimica Acta, 2003. 475(1–2): p. 1-15.

38. Agbor, N.E., M.C. Petty, and A.P. Monkman, *Polyaniline thin films for gas sensing.* Sensors and Actuators B: Chemical, 1995. 28(3): p. 173-179.

39. Matsuguchi, M., A. Okamoto, and Y. Sakai, *Effect of humidity on NH3 gas sensitivity of polyaniline blend films.* Sensors and Actuators B: Chemical, 2003. 94(1): p. 46-52.

40. Gong, J., et al., *Ultrasensitive NH3 Gas Sensor from Polyaniline Nanograin Enchased TiO2 Fibers.* The Journal of Physical Chemistry C, 2010. 114(21): p. 9970-9974.

41. Yan, X.B., et al., *NO2 gas sensing with polyaniline nanofibers synthesized by a facile aqueous/organic interfacial polymerization.* Sensors and Actuators B: Chemical, 2007. 123(1): p. 107-113.

42. McGovern, S.T., G.M. Spinks, and G.G. Wallace, *Micro-humidity sensors based on a processable polyaniline blend.* Sensors and Actuators B: Chemical, 2005. 107(2): p. 657-665.

43. Sharma, A.L., K. Kumar, and A. Deep, *Nanostructured polyaniline films on silicon for sensitive sensing of ammonia.* Sensors and Actuators A: Physical, 2013. 198(0): p. 107-112.

44. Chabukswar, V.V., S. Pethkar, and A.A. Athawale, *Acrylic acid doped polyaniline as an ammonia sensor.* Sensors and Actuators B: Chemical, 2001. 77(3): p. 657-663.

45. Tai, H., et al., *Fabrication and gas sensitivity of polyaniline–titanium dioxide nanocomposite thin film.* Sensors and Actuators B: Chemical, 2007. 125(2): p. 644-650.

46. Li, D., et al., *Self-assembly of polyaniline ultrathin films based on doping-induced deposition effect and applications for chemical sensors.* Sensors and Actuators B: Chemical, 2000. 66(1–3): p. 125-127.

47. Bishop-Haynes, A. and P. Gouma, *Electrospun Polyaniline Composites for NO2 Detection.* Materials and Manufacturing Processes, 2007. 22(6): p. 764-767.

48. Zhang, D., et al., *Detection of NO2 down to ppb Levels Using Individual and Multiple In2O3 Nanowire Devices.* Nano Letters, 2004. 4(10): p. 1919-1924.

49. Mönch, W., *Semiconductor surfaces and interfaces*. Vol. 26. 2001: Springer.

50. John, M.F., et al., *Biocompatibility implications of polypyrrole synthesis techniques.* Biomedical Materials, 2008. 3(3): p. 034124.

Appendix B. Composition-dependent sensing mechanism of electrospun conductive polymer composite nanofibers

Abstract

Electrospinning provides a means to synthesize nanofibrous structures with very high surface area-to-volume ratio that enhance the sensitivity of conductive polymer (CP)-based gas sensors in a cost effective manner. Despite these advantages, high intrinsic conductivity prevents electrospinning of pure CPs, therefore requiring an alloy with insulating polymers. Unlike CPs, the contribution of insulating polymers on overall sensing performance of composites has not been systemically investigated. To examine the effects of insulating polymers on the sensitivity to various analytes, different composition ratios of polyaniline (PANI)/poly(□-caprolactone) (PCL) nanofibers were produced by electrospinning. FT-IR spectroscopy was utilized to determine the mass composition of the composites. The nanofibers were secondary doped with camphorsulfonic acid to modulate their conductivity to a range appropriate for sensing. Diffuse reflectance UV-Vis spectroscopy was used for chemical characterization to determine its protonation state. The PANI/PCL electrospun composite nanofibers were configured in a chemiresistor and subjected to different analytes, including H_2O vapor, NH_3, and NO_2. H_2O vapor and NO_2 showed a polarity change in sensitivity past a threshold of PANI-to-PCL composition ratio. To investigate this polarity change, the

temperature dependence of electrical conductivity was examined. When H_2O vapor was exposed to the composite with the highest PANI content, there was a decrease in hopping distance; on the other hand, an increase in hopping distance was observed when H_2O vapor was exposed to the composite with the lowest PANI content. These results show an existence of competition between the conductive polymer, PANI, and the insulating host polymer, PCL, for analyte interaction, both of which integratively determine the overall sensitivity. The work demonstrates that the host polymer plays an important role in structural swelling as well as chemical interaction with analytes, which critically modulate sensing behavior.

Keywords: Polyaniline, poly(□-caprolactone), composite, host polymer, sensor, electrospinning

1. Introduction

Conductive polymers (CPs), such as polyaniline (PANI), polypyrrole (PPy), and poly(3,4-ethylenedioxythiophene) (PEDOT), have been extensively studied as sensing materials [1-4]. They provide ideal characteristics for sensing such as high sensitivity, short response time, and room temperature operation, as compared to conventional metal oxide sensors [5, 6]. These organic polymers behave similarly to semiconductors, where their electrical properties are tunable with dopants to induce conductivities ranging from metallic to insulating [7]. Moreover, their polymer chain structure provides an opportunity to control their interaction with specific analytes by modifying functional side groups or blending with different polymers as a composite [8, 9].

The sensitivity of gas sensors depends on the amount of analyte interaction with the sensing material. Therefore, the development of rapid responding and ultrasensitive sensors has focused on increasing the surface area-to-volume ratio by engineering their microstructure. In addition, nano-scale morphology improves sensitivity when the dimensions approach the Debye length, which significantly affects local charge transport [10]. In this regard, one-dimensional (1D) structures, such as nanowires and nanorods, have been developed to enhance sensitivity, response and recovery time, and low gas detection limits of CP gas sensors [10-14].

Many fabrication techniques have been employed to synthesized 1D structures in bulk quantities, such as electrochemical polymerization [15], interfacial polymerization [16], rapid-mixing reaction [17], and radiolytic synthesis [18].

Particularly, electrospinning provides a simple and low cost method of bulk-synthesizing long 1D nanostructures. The structures of electrospun nanofibers, such as fiber diameter dimensions and morphology, can be easily controlled by modifying processing parameters including the applied electric field and flow rates, and solution parameters including solvent selection, viscosity and conductivity of the electrospinning solution [19-21]. As a result, electrospinning allows the synthesis of polymeric nanofibers in a tunable and scalable manner.

Despite the many advantages of electrospinning for polymer processing, pure CPs cannot be directly electrospun due to its intrinsically high conductivity. Highly charged solution creates electrical instability during electrospinning that frustrates the formation of Taylor cone [22]. This leads to charged polymer chain repulsion before their entanglement to produce a continuous fibrous morphology [23]. In addition to its unsuitable electrical properties for electrospinning, pure CPs are typically brittle due to tight coil-like conformation in the backbone, resulting in mechanical instability [24]. Therefore, to improve the processability of electrospinning with CPs, they are incorporated into a non-conducting host polymer solution to enable electrospinning, improve mechanical properties, and control fiber morphology [25-27]. Furthermore, the chemical structure of the host polymer in the composite affects electron or proton transfers during charge conduction [28], providing an opportunity to tune the electrical properties of the composite. In addition to influencing charge conduction, the host polymer interacts with the analyte, depending on the solubility of the gas to the

polymer [29]. Therefore, it is important to understand the interaction between CP and host polymer with an analyte to improve sensor technology.

For electrospun CP-based configurations, there are two major approaches to modulate gas sensing performance: (1) controlling electrical conductivity of PANI gas sensor to enhance sensitivity and (2) varying CP : host polymer composition ratio to alter sensing behavior. Previously, we have shown how dopant and doping duration affect the electrical properties of PANI/poly(ε-caprolactone) (PCL) composite nanofibers, thus their sensitivity to various analytes [30]. In this study, we aimed to further understand how the composition of CP and host polymer affects the electrical properties and sensing behavior of electrospun PANI/PCL composite nanofibers. Different ratios of PANI/PCL composite nanofibers were synthesized and their responses to H_2O vapor, NH_3 and NO_2 gases were examined.

2. Experimental Methods

2.1. Synthesis of PANI/PCL composite nanofibers

Camphorsulfonic acid (HCSA, 2.75 mg/mL) solution was prepared by dissolving (1R)-(–)-10-camphorsulfonic acid (Sigma-Aldrich, St. Louis, MO) in 1,1,1,3,3,3-hexafluoro-2-propanol (HFIP) (Oakwood Products, Inc., Indianapolis, IN) with rigorous stirring at 1,200 rpm. Polyaniline (PANI, 3 mg/mL) in the emeraldine base form (M_w = 50,000, Sigma-Aldrich) was then dispersed into the prepared HCSA solution. The mixed

solution was sonicated for 5 minutes and stirred at 1,200 rpm for 5 minutes at room temperature. The sonication/stirring process was repeated 4 times, followed by a final continuous stirring for 4 hours in order to achieve a homogenous PANI dispersion. The PANI-HCSA solution was filtered with a 0.22 μm syringe filter to remove agglomerates, and its loss due to filtering was quantified by ultra-violet visible (UV-Vis) spectroscopy as previously described [30]. A 7 wt.% solution of PCL (M_w = 65,000, Sigma-Aldrich) was separately prepared by dissolving the pellets in HFIP. The filtered PANI solution was mixed with the PCL solution at various volume ratios of 7:3, 6:4, 5:5, and 4:6.

These PANI/PCL solutions with different compositions were electrospun to synthesize nanofibers having similar dimensions by adjusting their viscosity through dilution with solvent. Viscosity, one of the major solution properties that affect electrospinning, was determined by a Brookfield cone-and-plate viscometer. The stock PANI-PCL solutions with different compositions were serially diluted with HFIP to yield similar viscosity values. A high voltage D.C. power supply (Glassman High Voltage, NJ) at an applied voltage of approximately -5.8 kV with a solution flow rate of 0.3 mL/hr and a 55 cm tip to plane collector distance were set to produce an approximately 1.5 μm-thick fiber mat. The thickness of the fiber mat was controlled by adjusting the deposition time. The fiber mats were stored under vacuum to preserve the samples before any further experimentations.

2.2. Secondary doping by HCSA

Due to intrinsically low conductivity of PCL, the electrospun fibers were further doped with aqueous HCSA to increase their conductivity to appropriate levels in order to determine their gas sensing behavior. All the fiber mats were incubated in 50 μL of 1 M HCSA at room temperature for various durations ranging from 30 minutes to 9 hours. After the doping process, the acid was aspirated and the fiber mats were rinsed with DI water, followed by air drying for 1 hour at room temperature.

2.3. Characterization of PANI/PCL nanofibers

The morphology and fiber diameter of the electrospun fiber mats were characterized by using a scanning electron microscope (SEM, Nova NanoSEM450, FEI, Hillsboro, Oregon). The composite nanofibers were sputter-coated with platinum-palladium prior to visualization under SEM. At least 100 individual fibers were assessed to determine average fiber diameter.

To confirm the various compositional ratios of the PANI/PCL composite nanofibers, Fourier-transform infrared spectra were examined by the Equinox 55 FT-IR (Bruker, Billerica, MA). The HCSA-doped nanofiber mat was placed on a polished NaCl substrate and its infrared light transmission was measured with 32 scans at a resolution of 0.5 cm^{-1} in the range between 600 and 3000 cm^{-1}.

In order to determine doping states, diffuse reflectance UV-Vis spectroscopy was used to measure the absorbance of the various ratios of secondary doped composite nanofibers using a UV-Vis Spectrometer (Evolution 300, Thermo Scientific, Waltham, MA). The absorbance spectra were measured in the wavelength range between 190 and 1100 nm.

2.4. Characterization of electrical properties

To determine the electrical property of the composite nanofibers, a strip of nanofiber mat having an approximate dimension of 4 mm x 6 mm with a thickness of 1.5 □m was placed onto a 500 □m-thick oxidized silicon substrate. Gold microelectrodes with the thickness of ~300 nm were deposited onto the sample by sputtering using the EMS 575X sputter (Electron Microscopy Science, Hatfield, PA). The electrical characterization of a PANI/PCL fiber mat was performed by sweeping the potential of -0.5 V to 0.5 V from probing source and drain microelectrodes to generate I-V curves using a source-meter (Keithley 2363, Cleveland, OH). The electrical conductivity of PANI/PCL composite nanofibers was determined by normalizing it to the thickness of the sample.

2.5 Gas sensing measurement

A custom gas sensing device was fabricated to measure the analyte sensing performance of different composite nanofibers as previously described [31]. Briefly, the fiber mat integrated with gold microelectrodes was mounted onto a sample holder and enclosed by a glass chamber with the volume of 3.15 cm^3 with an inlet and outlet port for gas flow. The chip was then clipped to a Keithley source-meter to establish an electrical connection. The gas sensing performance of HCSA-doped PANI/PCL nanofibers were examined against various gases including water (H_2O) vapor, ammonia (NH_3), and nitrogen dioxide (NO_2) at room temperature with a custom built gas sensing system with Alicat mass flow controllers (MFC) operated by LabVIEW. All the analytes were thoroughly mixed with carrier gas (dry air) before being introduced to the chamber. The volumetric flow rate was kept constant to 200 standard cubic centimeters per minute (sccm), and the ratio of the two MFCs was used to control the exposure concentration.

2.6. Characterization of charge transport properties

To understand the electronic conduction mechanism for various ratios of PANI/PCL composite nanofibers, the temperature dependence of electrical conductivity of the composite nanofibers was investigated. I-V plots were obtained by sweeping from -0.5 to 0.5 V at temperatures ranging from 300 K down to 30 K. The change in temperature was controlled by a vacuum sealed refrigerator and compressor (Model

8200, Janis Research Company, INC), which was controlled by custom LabVIEW program.

3. Results and Discussion

3.1. Fabrication of PANI/PCL nanofibers and its material characterization

Electrospinning is a method for synthesizing nanostructured polymers with a high surface area-to-volume ratio in a cost effective manner, which provides an opportunity for the mass-production of ultrasensitive sensors. However, due to their high intrinsic conductivity, CPs are typically electrospun with insulating polymers. In this regard, understanding how analytes interact with the insulating polymer in addition to CPs is critical to manufacture a sensor with desired selectivity and optimal sensitivity. Therefore, the effects of composition in the electrospun composite nanofibers on sensing behavior were investigated in this study.

To produce similar nanofiber diameters with different ratios of PANI (CP) and PCL (insulating host polymer), the viscosity of the electrospinning solutions, one of the main factors that determines the electrospun fiber diameter, was adjusted for each condition (Table 1). The viscosity of 7:3, 6:4, 5:5, and 4:6 PANI/PCL solution mixtures was measured at the calculated solution shear rate during electrospinning at the spinneret (3.74 s^{-1}). Based on these measurements, the solutions were further diluted by 5%, 20%, 30%, and 40 V% in HFIP, respectively, which resulted in a close range of

viscosities among the solutions as shown in Table 1. Fig. 1 shows the resultant microstructure of electrospun PANI/PCL composites from each solution, exhibiting randomly oriented nanofibers with relatively uniform fiber diameter and a typical cylindrical morphology. Quantitative analysis of the fibers shows the tightly controlled average fiber diameter of approximately 150 nm for all conditions (Table 1). The fiber mat thickness was controlled to be approximately 1.50 □m.

FT-IR spectroscopy was performed to precisely determine the mass composition of PANI content of each resultant composite. Fig. 2 displays the FT-IR absorption spectra of 7:3, 6:4, 5:5, and 4:6 (V/V) PANI/PCL composites. PANI is characterized by the absorption bands at 825 for C-H bending vibration of benzene ring, 1161 cm^{-1} for vibration mode of quinoid ring, 1297 cm^{-1} for stretching vibration of C-N, 1493 cm^{-1} for stretching vibration of N-benzenoid ring, and 1586 cm^{-1} for stretching vibration of N-quinoid ring of PANI [32, 33]. On the other hand, the FT-IR characteristic absorption bands at 2949 cm^{-1} is for asymmetric CH_2, 2866 cm^{-1} is for symmetric CH_2, and 1730 cm^{-1} is for carbonyl stretching of PCL [34]. The mass composition was determined by the ratio of the PANI peak area (1294 cm^{-1}) to the total peak area of PANI and PCL (1728 cm^{-1}) [35]. This calculation resulted in the mass composition of approximately 20, 16, 12, and 9 wt.% PANI, corresponding to 7:3, 3:2, 1:1, and 2:3 (V/V) PANI/PCL solutions, respectively (Table 1).

3.2. Electrical characterization of electrospun PANI/PCL nanofibers

The electrospun PANI/PCL composites were further doped with HCSA to increase conductivities to a range appropriate for analyte detection [30]. The electrical properties of as-spun PANI/PCL nanofibers and those after various HCSA secondary doping durations were obtained from I-V characteristics by sweeping the voltage between -0.5 to 0.5 V and by normalizing them to the geometry of the nanofiber mats (Fig. 3). All the conductivities of the nanofiber mats with various compositions stabilized after 9 hours of HCSA secondary doping, resulting in the electrical conductivities of 20, 16, 12, and 9 wt.% PANI nanofiber mats to be approximately $7.0X10^{-4}$, $1.9X10^{-4}$, $7.2X10^{-5}$, and $4.1X10^{-5}$ S/cm, respectively. Based on these measurements, HCSA doping for 9 hours was used for the remainder of the study.

To observe the protonation state of the PANI/PCL composite nanofibers after the secondary doping, diffuse reflectance UV-Vis spectroscopy was utilized. Fig. 4 shows the diffuse reflectance UV-Vis spectra from the various ratios of PANI/PCL composites based on the Kulbeka-Munk Function [36]. During the doping process, the sulfonic group from HCSA induces the increase of the number of charge carriers by protonating the imine on PANI [37]. As a result, the band gap for electron excitation is altered during the doping process. The slope of the peak at approximately 2.8 eV, which indicates the protonation level of PANI, was used to calculate the band gap [38]. The band gaps of PANI in the various compositions exhibited a similar value at 2.3 eV, demonstrating that the

protonation state of the PANI is consistent after the secondary doping for all compositions.

3.3. Gas sensing properties of electrospun PANI/PCL nanofibers

To examine how different compositions of PANI/PCL nanofibers affect the composite's sensing behavior, responses to various analytes including H_2O vapor, NH_3, and NO_2 were tested. Prior to analyte exposure, dry air was introduced over the sensor for an hour to establish the baseline. Afterward, the sensor was subjected to various concentrations of analytes, followed by a recovery period with dry air in a step-wise manner. The normalized changes in electrical resistance ($\Delta R/R_o$) and sensitivity of various compositions of CSA-doped PANI/PCL nanofibers were plotted against different concentrations of various gas in Fig. 5 and Fig. 6. The R_o and ΔR were defined as the initial base-line resistance and the change in resistance from the base-line upon being subjected to an analyte, respectively.

During H_2O vapor exposure, at higher PANI content, the sensors show a negative $\Delta R/R_o$ similar to pure PANI thin film [39]. In this study, despite having slightly different conductivities, both 20 and 16 wt.% PANI exhibited negative responses, indicating proton exchange-assisted conduction of electrons (PEACE) mechanism, in which the imine group of PANI is protonated by H_2O vapor [40]. As the ratio of PANI content decreases and PCL increases, the sensing profile changes from a negative to a positive

$\Delta R/R_o$. Interestingly, 12 wt.% PANI exhibited both negative (at lower concentrations of H_2O vapor) and positive (at higher concentrations) $\Delta R/R_o$. The positive response of $\Delta R/R_o$ to H_2O was further intensified in 9 wt.% PANI. Fig. 6a shows the effect of different composition ratios of PANI to PCL on H_2O vapor sensitivity. The data demonstrate that the changes in PANI content can alter the polarity of sensitivity, indicated by the sign of the slope in $\Delta R/R_o$ vs. concentration of analyte. A possible explanation of this change in the polarity of sensitivity is the alteration in the underlying sensing mechanism from PANI dominant to PCL dominant charge conduction. PCL is a semi-crystalline polymer. When water interacts with the structure, hydrolysis occurs at the ester linkage of PCL [41]. This causes swelling of PCL chains in the radial direction [42]. Considering that the changes in resistance during gas sensing by PANI is due to proton movement along the backbone of the polymer, the volume increase of host polymer is likely to increase the path length of charge transport, thus increasing overall resistance.

On the other hand, all compositions of PANI/PCL composite nanofibers show a positive $\Delta R/R_o$ to NH_3 similar to the sensing profile of pure PANI film (Fig. 5) [43]. When introduced to the PANI/PCL nanofibers, NH_3, a deprotonating agent, interacts with protons on the PANI backbone and transforms to ammonium ion, NH_4^+. This reduces the number of free charge carriers in the system [44]. As a result, the electrical resistance of PANI/PCL nanofibers increases. When the PCL content increases, the sensitivity to NH_3 decreases significantly, possibly due to a decrease in available PANI polymers to interact

with the analyte and an increase in charge conduction pathway (Fig. 6). However, unlike H_2O vapor, high PCL content did not change the polarity of the sensitivity.

Lastly, NO_2, an oxidizing gas, chemically reacts with PANI, leading to changes in the doping level of PANI and altering its resistance. Due to its greater electron affinity, NO_2 typically removes electrons from the □-conjugated region of an undoped PANI backbone [45]. But in the case of the doped emeraldine salt form of PANI, when NO_2 interacts with it, it will further increase the oxidation state, decreasing the conductivity [46]. In parallel with this observation, there was an increase in $\Delta R/R_o$ in the highest PANI content (Fig. 5). Due to the strong interaction between NO_2 and PANI, the desorption rate of NO_2 is very low, inducing a poisoning effect [45]. Past a threshold, 12 and 9 wt.% PANI exhibit a change in response, from positive to negative $\Delta R/R_o$ (Fig. 5 and Fig. 6). Although the effects of NO_2 on PCL are unclear, higher PCL content does affect overall sensing response, depicted by the change of sensitivity polarity. To the best of our knowledge, there has not been any reports of chemical interaction between PCL and NO_2. Nevertheless, Ryan et al. showed an increase in $\Delta R/R_o$ when PCL-carbon black composite was exposed to SO_2, a reducing gas [47]. Carbon black is widely used as a conductive medium without specific sensing functionality and relays electrical signals detected by insulating polymers in an electronic nose [48]. In this setup, SO_2 interacts with the ester linkage, reacting with the carbonyl functional groups by donating its electron [49]. This interaction increases $\Delta R/R_o$ of the sensor. Based on this observation,

it is possible that an oxidizing gas like NO_2 would induce the opposite response, decreasing $\Delta R/R_o$ as observed in Fig. 5 and Fig. 6.

3.4. Composition-dependent charge transport

In order to investigate the charge conduction behavior of PANI/PCL composite nanofibers at different compositions, the charge hopping mechanism was examined by the temperature dependence of the electrical conductivity. The samples were subjected to different temperatures ranging from 30 to 300 K and the resistance of the nanofibers was obtained from I-V characteristics generated by sweeping the voltage between -0.5 to 0.5 V across source and drain gold electrodes. All compositions exhibit ohmic contact in this temperature range (Fig. S1). CPs are composed of branched 1D chains; thus, the charge carriers are primarily transported intra-chain or inter-chain by a hopping mechanism [50]. Fig. 7a shows the temperature-dependent resistivity of PANI/PCL nanofibers with various compositions. As expected, 9 wt% PANI showed the greatest change in resistivity with respect to temperature change, due to higher content of insulating polymer. To explain the disorderly movement of charge, the mechanism of Mott's variable-range hopping was utilized [51]. In the variable-range hopping model, the conductivity in three dimensions is given by [52]:

$$\sigma = \sigma_o \exp[-(T_o/T)]^{1/4} \quad (1)$$

and

$$\sigma_o = e^2 v R^2 N(E) \quad (2)$$

$$T_o = \lambda\alpha / kN(E) \quad (3)$$

, where e is the electronic charge, v a hopping frequency, λ≈18.1 a dimensionless constant [53], α the inverse rate of fall of the wave function [54], *k* Boltzmann's constant, N(E) the density of states at the Fermi level. The hopping distance, R, and hopping energy, W, can be then determined by:

$$R = [9/(8\pi\alpha kTN(E))]^{1/4} \quad (4)$$

$$W = (3/4)\pi R^3 N(E) \quad (5)$$

Assuming a reasonable value of α = 10 Å and characteristic phonon frequency γ = 10^{13} s^{-1} [53], the calculated values of N(E) were 1.27, 55.6, 61.9 and 779 $Å^{-3}$ for 20, 16, 12, and 9 wt.% PANI composites, respectively. Fig. 7b and 7c show the calculated the hopping distances and the required energy for charge hopping to distant, energetically available sites, demonstrating a significant increase of those values in 9 wt.% PANI. Overall, the higher PCL content increases the charge conduction pathway, which requires greater hopping distance and hopping energy.

The above observation is significant to understand the mechanism that changes the composition-dependent sensitivity of PANI/PCL. As shown in the sensing response to H_2O vapor, as the ratio of PANI/PCL decreases, the polarity of sensitivity changes from a negative to a positive $\Delta R/R_o$. To further investigate the mechanism behind this phenomenon, two extreme compositions that showed different polarity of sensitivity, 20 and 9 wt%. PANI, were subjected to the temperature-dependent electrical conductivity measurement under 50% H_2O vapor exposure (Fig. 8). 50% H_2O saturation was chosen due to the greatest response shown in the sensing performance (Fig. 5) while preventing water condensation at the low range of the examined temperatures. When exposed to H_2O vapor, the hopping distance decreased in the higher PANI content while it increased in the higher PCL content. It demonstrates that the composition-dependent change is likely due to the switch of the conduction mechanism from PANI to PCL dominant. This can be explained by the percolation theory in conjunction with two competing mechanisms of PANI-protonation and PCL-swelling [55]. When the concentration of PANI is high, a conduction pathway is formed for charge carriers to move along the PANI backbone. Thus, the protonation of PANI by H_2O vapor, a p-type semiconductor, decreases resistance. However, as the PCL content increases, the effect of PCL swelling that increases resistance due to lengthened charge hopping distance, dominates the overall conduction mechanism competing with the increase in charge carrier density by PANI protonation.

4. Conclusion

Various compositions of PANI/PCL nanofiber mats with similar structural and chemical characteristics were synthesized by controlling electrospinning parameters. When the different composite nanofiber sensors were exposed to H_2O vapor or NO_2, there was a change in the polarity of sensitivity past a threshold of PANI/PCL composition. This change in sensing behavior is attributed to competition between interactions of each polymer in the composite to analytes. Specifically, when there are competing mechanisms by the CP and the insulating host polymer that oppositely affect charge conduction, a polarity change in sensitivity exists depending on the composition ratio. This study demonstrates the importance of host polymer on the sensing behavior due to chemical interaction as well as physical swelling. Therefore, in addition to sensing properties of CPs, physiochemical interaction of host insulating polymer with various analytes must be accounted for when developing and optimizing sensors using conductive polymer composites.

5. Acknowledgement

We greatly acknowledge the financial support from KIMS Academy Laboratory Program.

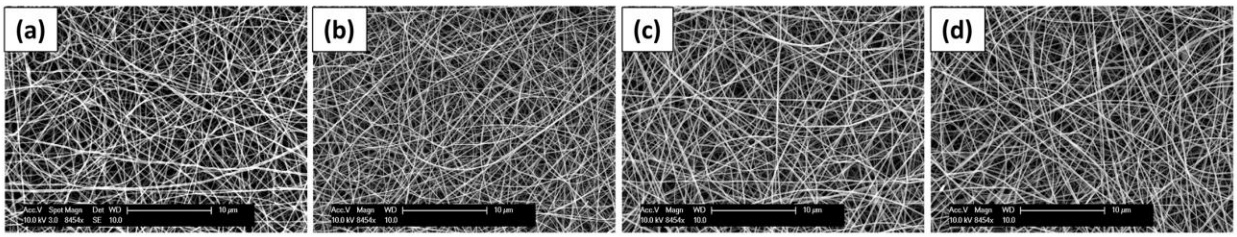

Figure B.1. Nanofiber morphologies from (a) 7:3, (b) 6:4, (c) 5:5, and (d) 4:6 (V/V) PANI/PCL solution mixtures.

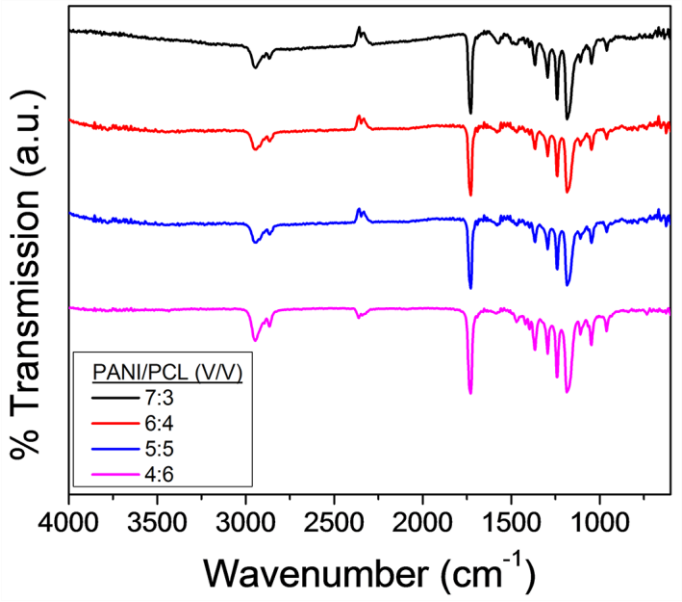

Figure B.2. FT-IR spectra of un-doped PANI/PCL composite nanofibers electrospun from 7:3, 6:4, 5:5, 4:6 (V/V) PANI/PCL solution mixtures.

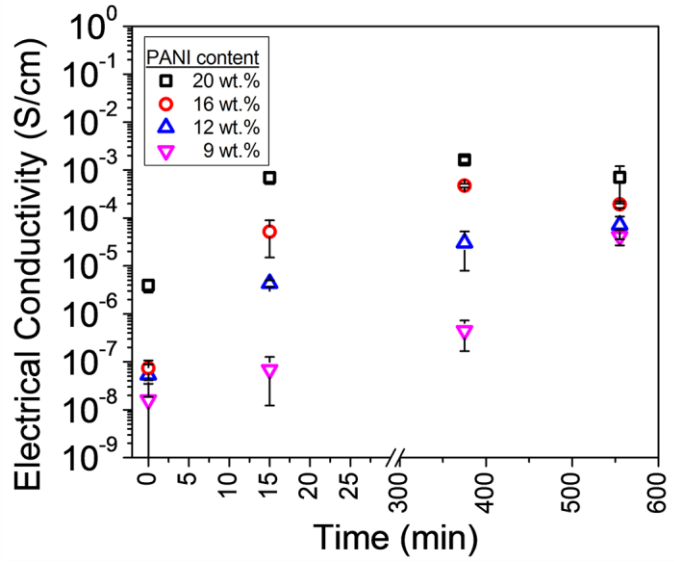

Figure B.3. Effect of HCSA secondary doping time on the electrical conductivity of PANI/PCL nanofiber composites.

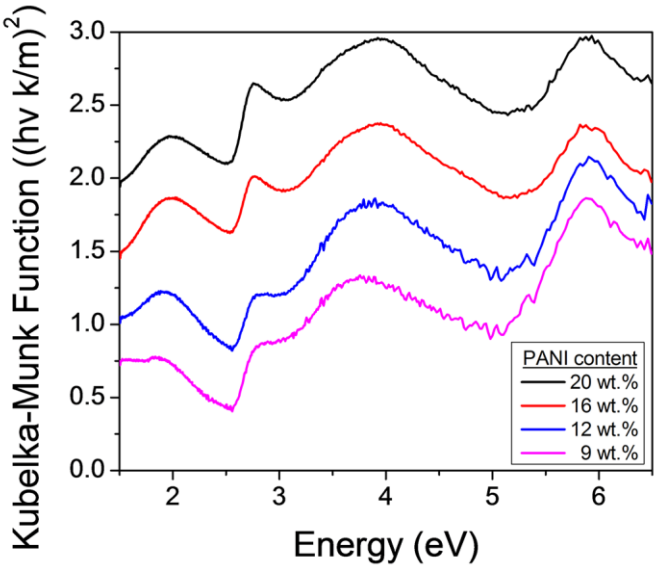

Figure B.4. UV-Vis spectra of CSA-doped 20, 16, 12, and 9 wt.% PANI composite nanofiber mats.

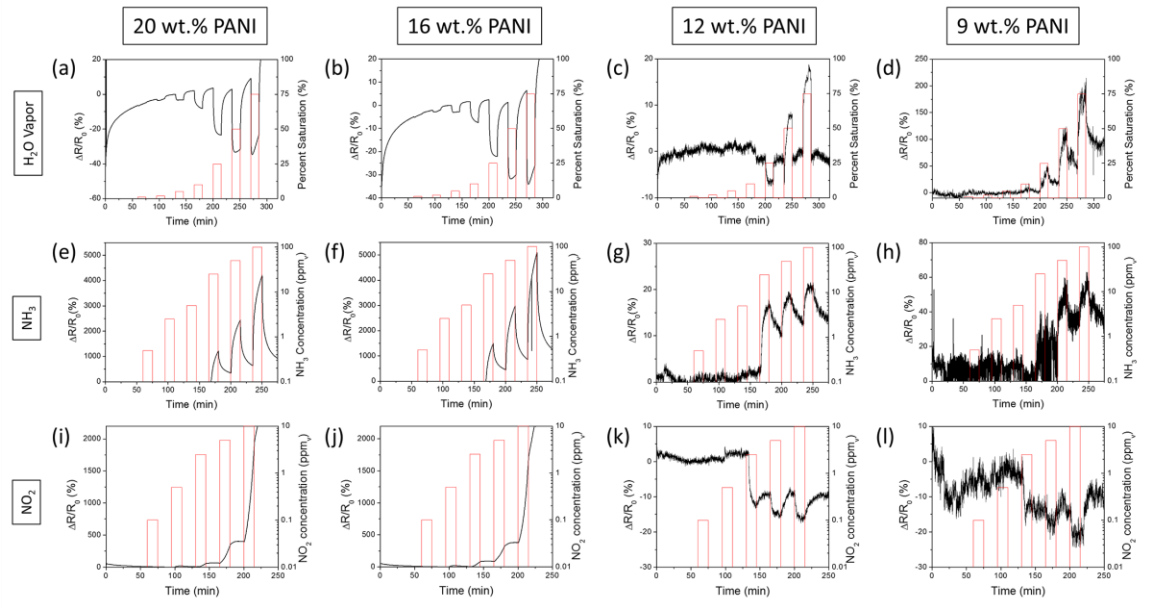

Figure B.5. Transient sensing profiles of ((a), (e), and (i)) 20, ((b), (f), and (j)) 16, ((c), (g), and (k)) 12 and ((d), (h), and (l)) 9wt.% PANI composite sensors to various concentrations of ((a) – (d)) H_2O vapor, ((e) – (h)) NH_3, and ((i) – (l)) NO_2.

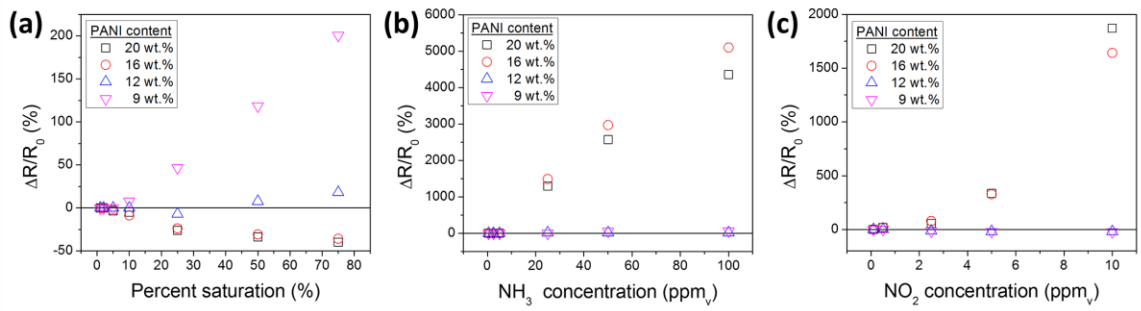

Figure B.6. Normalized responses of 20, 16, 12, 9 wt.%PANI composite sensors to various concentrations of (a) H_2O vapor, (b) NH_3, and (c) NO_2 gas.

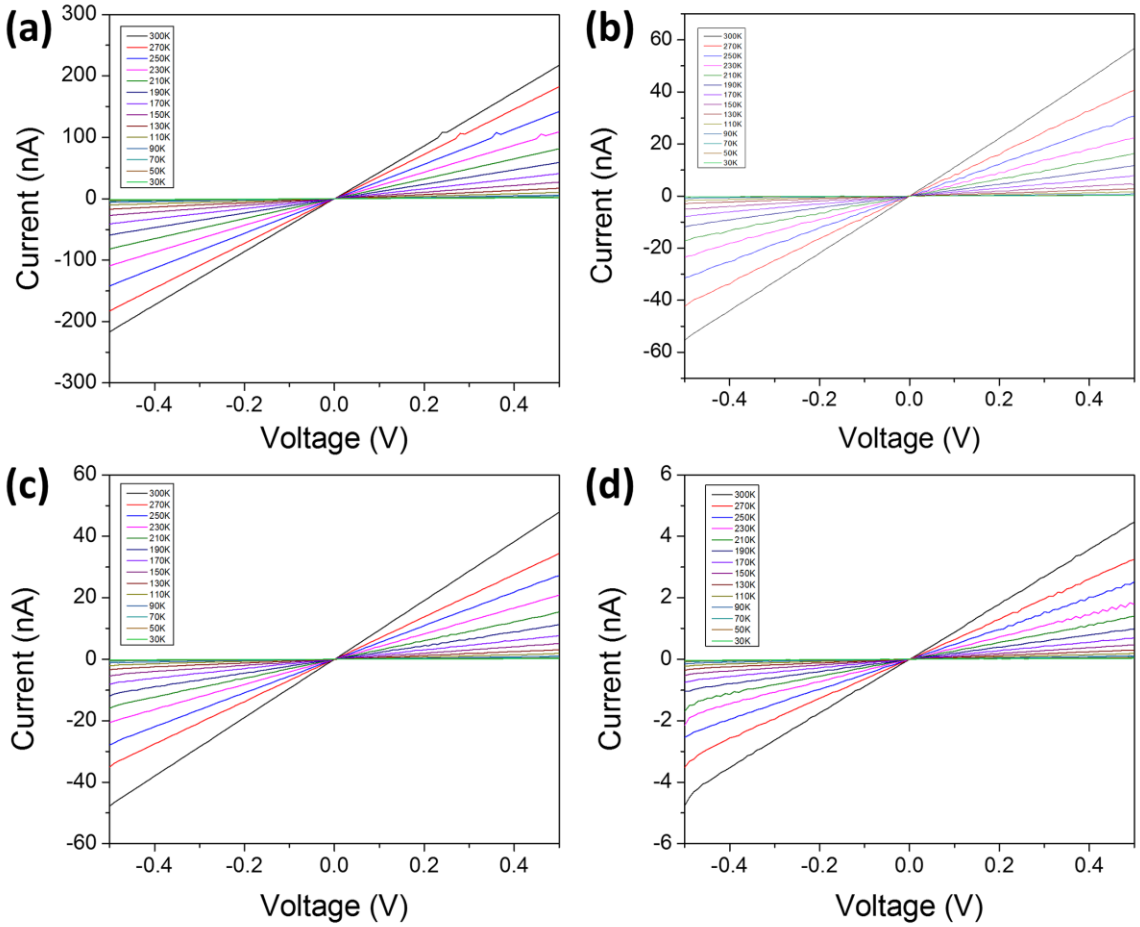

Figure B.7. I-V characteristic of (a) 20wt.%, (b) 16wt.%, (c) 12wt.% and (d) 9wt.% PANI composite sensors over a range of temperatures.

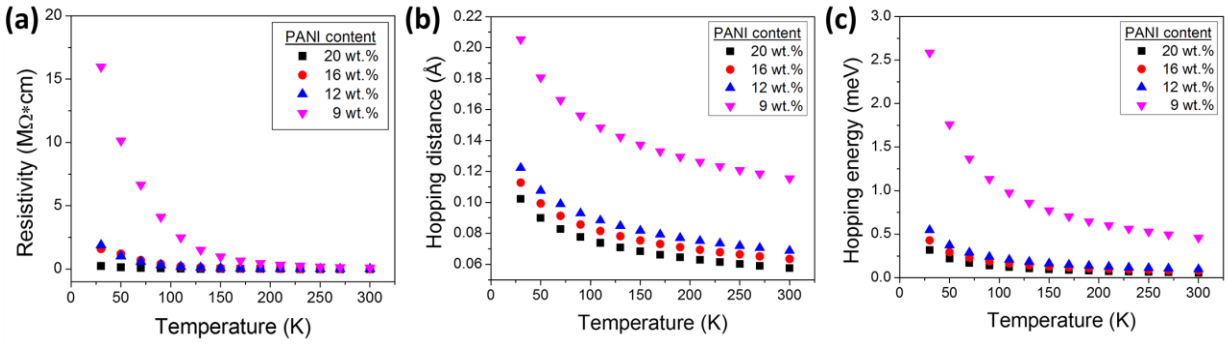

Figure B.8. (a) Resistivity, (b) hopping distance, and (c) hopping energy for 20, 16, 12, and 9 wt.% PANI composite with respect to temperature.

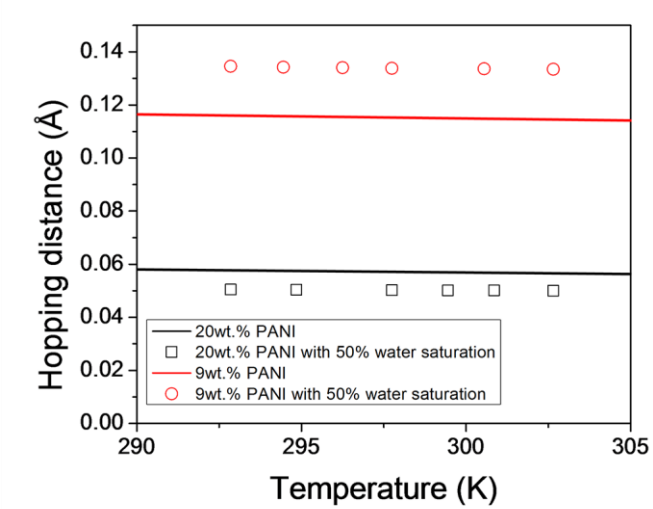

Figure B.9. Hopping distance for 20wt.% and 9wt.% PANI composite under exposure to 50% H_2O vapor for a range of temperatures.

References

1. Bai, H. and G. Shi, *Gas Sensors Based on Conducting Polymers.* Sensors, 2007. **7**(3): p. 267-307.

2. Janata, J. and M. Josowicz, *Conducting polymers in electronic chemical sensors.* Nat Mater, 2003. **2**(1): p. 19-24.

3. Lange, U., N.V. Roznyatovskaya, and V.M. Mirsky, *Conducting polymers in chemical sensors and arrays.* Analytica chimica acta, 2008. **614**(1): p. 1-26.

4. Chartuprayoon, N., et al., *Polypyrrole nanoribbon based chemiresistive immunosensors for viral plant pathogen detection.* Anal. Methods, 2013. **5**: p. 3497-3502.

5. Gerard, M., A. Chaubey, and B. Malhotra, *Application of conducting polymers to biosensors.* Biosensors and Bioelectronics, 2002. **17**(5): p. 345-359.

6. González-Rodríguez, D. and A.P. Schenning, *Hydrogen-bonded Supramolecular π-Functional Materials†.* Chemistry of Materials, 2010. **23**(3): p. 310-325.

7. Liu, H., et al., *Polymeric Nanowire Chemical Sensor.* Nano Letters, 2004. **4**(4): p. 671-675.

8. McQuade, D.T., A.E. Pullen, and T.M. Swager, *Conjugated polymer-based chemical sensors.* Chemical Reviews, 2000. **100**(7): p. 2537-2574.

9. Virji, S., et al., *Polyaniline Nanofiber Gas Sensors: Examination of Response Mechanisms.* Nano Letters, 2004. **4**(3): p. 491-496.

10. Chartuprayoon, N., et al., *Wafer-Scale Fabrication of Single Polypyrrole Nanoribbon-Based Ammonia Sensor.* The Journal of Physical Chemistry C, 2010. **114**(25): p. 11103-11108.

11. Hernandez, S.C., et al., *Single Polypyrrole Nanowire Ammonia Gas Sensor.* Electroanalysis, 2007. **19**(19-20): p. 2125-2130.

12. Hangarter, C.M., et al., *Tuning the gas sensing performance of single PEDOT nanowire devices.* Analyst, 2011. **136**(11): p. 2350-2358.

13. Hangarter, C.M., et al., *Conducting polymer nanowires for chemiresistive and FET-based bio/chemical sensors.* Journal of Materials Chemistry, 2010. **20**(16): p. 3131-3140.

14. Arafat, M.M., et al., *Gas Sensors Based on One Dimensional Nanostructured Metal-Oxides: A Review.* Sensors, 2012. **12**(6): p. 7207-7258.

15. Imisides, M.D., et al., *The use of electropolymerization to produce new sensing surfaces: a review emphasizing electrode position of heteroaromatic compounds.* Electroanalysis, 1991. **3**(9): p. 879-889.

16. Araújo, P.L.B., et al., *Synthesis and morphological characterization of PMMA/polyaniline nanofiber composites.* Microelectronics Journal, 2005. **36**(11): p. 1055-1057.

17. Huang, J. and R.B. Kaner, *The intrinsic nanofibrillar morphology of polyaniline.* Chemical communications, 2006(4): p. 367-376.

18. Pillalamarri, S.K., et al., *Radiolytic synthesis of polyaniline nanofibers: a new templateless pathway.* Chemistry of Materials, 2005. **17**(2): p. 227-229.

19. Reneker, D.H. and I. Chun, *Nanometre diameter fibres of polymer, produced by electrospinning.* Nanotechnology, 1996. **7**(3): p. 216.

20. Theron, S.A., E. Zussman, and A.L. Yarin, *Experimental investigation of the governing parameters in the electrospinning of polymer solutions.* Polymer, 2004. **45**(6): p. 2017-2030.

21. Nam, J., et al., *Materials selection and residual solvent retention in biodegradable electrospun fibers.* Journal of Applied Polymer Science, 2008. **107**(3): p. 1547-1554.

22. Rutledge, G.C. and S.V. Fridrikh, *Formation of fibers by electrospinning.* Advanced Drug Delivery Reviews, 2007. **59**(14): p. 1384-1391.

23. Hohman, M.M., et al., *Electrospinning and electrically forced jets. I. Stability theory.* Physics of Fluids (1994-present), 2001. **13**(8): p. 2201-2220.

24. Xia, Y., et al., *Camphorsulfonic Acid Fully Doped Polyaniline Emeraldine Salt: Conformations in Different Solvents Studied by an Ultraviolet/Visible/Near-Infrared Spectroscopic Method.* Chemistry of Materials, 1995. **7**(3): p. 443-445.

25. Kim, J.-S., S.-O. Sohn, and J.-S. Huh, *Fabrication and sensing behavior of PVF< sub> 2</sub> coated-polyaniline sensor for volatile organic compounds.* Sensors and Actuators B: Chemical, 2005. **108**(1): p. 409-413.

26. Strumpler, R. and J. Glatz-Reichenbach, *Conducting Polymer Composites.* Journal of Electroceramics, 1999. **3**(4): p. 329-346.

27. Brady, S., et al., *The development and characterisation of conducting polymeric-based sensing devices.* Synthetic Metals, 2005. **154**(1-3): p. 25-28.

28. Ogura, K., et al., *The humidity dependence of the electrical conductivity of a solublepolyaniline–poly (vinyl alcohol) composite film.* J. Mater. Chem., 1997. **7**(12): p. 2363-2366.

29. Belmares, M., et al., *Hildebrand and Hansen solubility parameters from molecular dynamics with applications to electronic nose polymer sensors.* Journal of computational chemistry, 2004. **25**(15): p. 1814-1826.

30. Low, K., et al., *Polyaniline/poly(ε -caprolactone) composite electrospun nanofiber-based gas sensors: optimization of sensing properties by dopants and doping concentration.* Nanotechnology, 2014. **25**(11): p. 115501.

31. Sandra , C.H., et al., *Single Polypyrrole Nanowire Ammonia Gas Sensor.* Electroanalysis, 2007. **19**(19-20): p. 2125-2130.

32. Yelil Arasi, A., et al., *The structural properties of Poly(aniline)—Analysis via FTIR spectroscopy.* Spectrochimica Acta Part A: Molecular and Biomolecular Spectroscopy, 2009. **74**(5): p. 1229-1234.

33. Zeng, X.-R. and T.-M. Ko, *Structures and properties of chemically reduced polyanilines.* Polymer, 1998. **39**(5): p. 1187-1195.

34. Elzein, T., et al., *FTIR study of polycaprolactone chain organization at interfaces.* Journal of Colloid and Interface Science, 2004. **273**(2): p. 381-387.

35. Bowley, B., et al., *The determination of the composition of polymeric composites using TG-FTIR.* Thermochimica acta, 1992. **200**: p. 309-315.

36. Murphy, A., *Band-gap determination from diffuse reflectance measurements of semiconductor films, and application to photoelectrochemical water-splitting.* Solar Energy Materials and Solar Cells, 2007. **91**(14): p. 1326-1337.

37. Wlodarski, W., et al. *Camphor sulfonic acid-doped polyaniline nanofiber-based 64o YX LiNbO3 SAW hydrogen gas sensor*. 2006.

38. Li, Y., et al., *Semiconducting properties of nanofiber polyaniline organic semiconductor.* Optoelectron. Adv. Mater., Rapid Commun, 2012. **6**: p. 235-238.

39. Nohria, R., et al., *Humidity sensor based on ultrathin polyaniline film deposited using layer-by-layer nano-assembly.* Sensors and Actuators B: Chemical, 2006. **114**(1): p. 218-222.

40. Ting, Z., et al., *A gas nanosensor unaffected by humidity.* Nanotechnology, 2009. **20**(25): p. 255501.

41. Woodward, S.C., et al., *The intracellular degradation of poly (ε-caprolactone).* Journal of biomedical materials research, 1985. **19**(4): p. 437-444.

42. Gorrasi, G., et al., *Vapor barrier properties of polycaprolactone montmorillonite nanocomposites: effect of clay dispersion.* Polymer, 2003. **44**(8): p. 2271-2279.

43. Matsuguchi, M., A. Okamoto, and Y. Sakai, *Effect of humidity on NH< sub> 3</sub> gas sensitivity of polyaniline blend films.* Sensors and Actuators B: Chemical, 2003. **94**(1): p. 46-52.

44. Kukla, A., Y.M. Shirshov, and S. Piletsky, *Ammonia sensors based on sensitive polyaniline films.* Sensors and Actuators B: Chemical, 1996. **37**(3): p. 135-140.

45. Agbor, N., M. Petty, and A. Monkman, *Polyaniline thin films for gas sensing.* Sensors and Actuators B: Chemical, 1995. **28**(3): p. 173-179.

46. Li, D., et al., *Self-assembly of polyaniline ultrathin films based on doping-induced deposition effect and applications for chemical sensors.* Sensors and Actuators B: Chemical, 2000. **66**(1): p. 125-127.

47. Ryan, M.A., et al., *Expanding the capabilities of the JPL electronic nose for an international space station technology demonstration*, 2006, SAE Technical Paper.

48. Ryan, M., et al., *Polymer–carbon black composite sensors in an electronic nose for air-quality monitoring.* MRS bulletin, 2004. **29**(10): p. 714-719.

49. Barbe, J.-C., et al., *Role of carbonyl compounds in SO2 binding phenomena in musts and wines from botrytized grapes.* Journal of agricultural and food chemistry, 2000. **48**(8): p. 3413-3419.

50. Kivelson, S., *Electron hopping in a soliton band: Conduction in lightly doped (CH) x.* Physical Review B, 1982. **25**(6): p. 3798.

51. Mott, N., E. Davis, and R. Street, *States in the gap and recombination in amorphous semiconductors.* Philosophical Magazine, 1975. **32**(5): p. 961-996.

52. Campos, M. and B.B. Jr, *Mechanism of conduction in doped polyaniline.* Journal of Physics D: Applied Physics, 1997. **30**(10): p. 1531.

53. Nair, K. and S.S. Mitra, *Electrical properties and hopping transport in amorphous silicon carbide films.* Journal of Non-Crystalline Solids, 1977. **24**(1): p. 1-17.

54. Singh, R., et al., *Low-frequency ac conduction in lightly doped polypyrrole films.* Journal of applied physics, 1991. **69**(4): p. 2504-2511.

55. Reghu, M., et al., *Transport in polyaniline networks near the percolation threshold.* Physical Review B, 1994. **50**(19): p. 13931.

Appendix C. Physicoelectrochemical characterization of pluripotent stem cells during self-renewal or differentiation by a multi-modal monitoring system

Abstract

Monitoring pluripotent stem cell behaviors (self-renewal and differentiation to specific lineages/phenotypes) is critical for a fundamental understanding of stem cell biology and their translational applications. In this study, a multi-modal stem cell monitoring system was developed to quantitatively characterize physicoelectrochemical changes of the cells in real time, in relation to cellular activities during self-renewal or lineage-specific differentiation, in a non-destructive, label-free manner. The system was validated by measuring physical (mass) and electrochemical (impedance) changes in human induced pluripotent stem cells undergoing self-renewal, or subjected to mesendodermal or ectodermal differentiation, and correlating them to morphological (size, shape) and biochemical changes (gene/protein expression). An equivalent circuit model was used to further dissect the electrochemical (resistive and capacitive) contributions of distinctive cellular features. Overall, the combination of the physicoelectrochemical measurements and electrical circuit modeling collectively offers a means to longitudinally quantify the states of stem cell self-renewal and differentiation.

Introduction

Human induced pluripotent stem cells (IPSCs), derived from individual patients, provide an excellent cell source for personalized regenerative medicine [1]. The efficacy of IPSCs has been well documented in animal models and the first human clinical trial using patient-derived IPSCs for retinal transplant is currently on-going [2]. In addition to their clinical applications, IPSCs also provide an ideal platform to develop patient-oriented and disease-specific *in vitro* models that can be utilized to understand pathological and molecular mechanisms during disease progression. For example, IPSCs have been used to study the pathology of amyotrophic lateral sclerosis (ALS) by reprogramming the patient's fibroblasts to IPSCs and differentiating the cells into functional motor neurons [3-5]. Such IPSC-derived *in vitro* models are especially valuable for drug screening aimed at developing personalized pharmaceutical therapies [6, 7]. Therefore, it is critical to quantitatively monitor the cellular behaviors during the course of IPSC self-renewal or differentiation toward specific lineages to fully utilize these diverse potentials of IPSCs.

Traditionally, stem cells have been characterized by biochemical techniques, such as polymerase chain reaction (PCR) and immuno-blotting, to determine changes in gene and protein expression. Although these traditional techniques offer semi-quantitative measurements for cellular behaviors, they are destructive in nature, which prevent tracking of specific populations of the cells throughout its biological processes. The most common non-destructive analytical method is flow cytometry, but this

technique requires labeling of surface-expressed biomarker as well as detachment of the cells from substrates, thus limiting longitudinal monitoring of the cells. In this regard, physical changes of the cells, i.e., mass and morphology, provide another means to assess cellular behaviors. Stem cell proliferation or self-renewal is distinguished by increased cell quantity, which corresponds to mass change. On the other hand, differentiation is typically associated with changes in cell morphology which can be qualitatively characterized by size, shape, and structural features [8-10]. For this reason, albeit semi-quantitative at best, morphology characterization via optical microscopy has been the gold standard to routinely observe cellular behaviors.

Such physical changes in cells, occurring during self-renewal or differentiation, result in corresponding alterations in their electrical properties as the cell acts as both a resistor and a capacitor [11-14]. Diverse morphological features (i.e., cell spread, roundness, and compactness), as well as changes in the type and quantity of cell-cell and cell-substrate junctions, affect the resistive and capacitive properties of the cell layer. Electrochemical impedance spectroscopy (EIS) is an analytical method to measure such electrical properties [15]. This technique applies alternating current (AC) voltage perturbation at a low amplitude over a range of frequencies to an electrochemical system, for example, composed of extracellular matrix (ECM), cells, and cell culture media. Cell adhesion and its morphological changes on a substrate surface causes alterations in the impedance derived from the resistive and capacitive components of the system. Especially, spectroscopic analysis of AC impedance over a range of

frequencies provides important information regarding cell-substrate and cell-cell interactions.

The electrical properties of cells were recently analyzed by EIS during the differentiation of stem cells [12, 16, 17]. These pioneering works have demonstrated a possibility of using changes in impedance as a biomarker for stem cell behaviors. However, the studies were limited to qualitative analyses, unable to fully realize the quantitative potentials of EIS to correlate the physical (cell quantity and morphology) and electrical (resistive and capacitive) properties of the cells with stem cell self-renewal/differentiation.

In this study, we developed a cell culture system to quantitatively monitor stem cell behaviors in real time during self-renewal and differentiation of IPSCs. The system combines quartz crystal microbalance (QCM) to monitor mass changes and EIS to measure impedance, in addition to optical clearance for cell visualization. The non-destructive, label-free nature of the system allows for longitudinal monitoring of the same population of the cells. Using this QCM-EIS real-time monitoring system, mass and impedance changes of IPSCs were correlated to changes in cell quantity and morphology. Furthermore, an equivalent circuit model was utilized to further dissect the changes in resistive and capacitive electrical properties of the cells, which were correlated to the progression of IPSC self-renewal and differentiation.

Results

Development of the multi-modal cell monitoring system

To non-destructively and quantitatively monitor stem cell behaviors in real time, a QCM-EIS device was developed using a three-electrode setup (Figure 1). The setup incorporates the working, reference, and auxiliary electrodes used for both QCM and EIS. A polytetrafluoroethylene (PTFE) bottom casing houses two gold electrodes, which are in contact with the electrode pattern on the QCM crystal. The working electrodes deliver an AC potential perturbation to resonate the crystal at its resonant frequency for monitoring mass changes. An indium tin oxide (ITO) QCM crystal was used due to its transparency, which allows for visual observation of the cells during culture. The electrode on the top surface of the QCM crystal was alternatively used as the voltage source when the device was used in the EIS mode. The top casing holds the Ag/AgCl reference electrode and platinum wire auxiliary electrode to complete the three electrode setup for the EIS system. A glass window is secured by a stainless steel ring above the top casing to provide an optical pathway while maintaining sterility during cell culture.

Morphological characterization of IPSCs during self-renewal and mesendodermal/ ectodermal differentiation

To obtain baseline morphological characteristics of IPSCs during self-renewal and differentiation, cells were cultured on Geltrex-coated tissue culture plates and subjected

to either self-renewal or differentiation conditions for various durations (Figure 2). The maintenance of pluripotency in the self-renewal condition and the differentiation efficiency toward mesendodermal and ectodermal lineages under the differentiation conditions were determined by immunofluorescence imaging (Figures 2A and S1). As expected, NANOG, a marker for pluripotency, was expressed throughout the duration of the culture for the self-renewal condition. GSC expression under the mesendodermal differentiation condition gradually increased beginning at Hour 72, while Nestin, an early ectodermal marker, was detected at Hour 96 for the cells subjected to the ectodermal differentiation condition.

To further confirm the pluripotency or differentiation state, gene expression after 96 hours for each condition was determined by real-time polymerase chain reaction (RT-PCR) (Figure 2B). For the self-renewal condition, there was no significant changes in the expression of *OCT4, NANOG,* and *DNMT3B* after 96 hours of culture in the system. For the mesendodermal differentiation condition, a significant upregulation of *T*, *GSC,* and *MIXL1* was observed after 96 hours. Similarly, a significant upregulation of *PAX6*, *NES*, and *SOX1* was induced by the ectodermal differentiation condition. The data, together with the protein expression analyses, indicate that the conditions utilized in this study resulted in the maintenance of the pluripotency or differentiation toward mesendodermal and ectodermal lineages.

The immunofluorescent images were utilized to determine the number of cells (Figure 2C) and cell morphology (Figures 2D-2F). Up to Hour 60, all three conditions

exhibited an increase in cell number. Following Hour 60, self-renewal and ectodermal differentiation continued to increase in cell number, while mesendodermal differentiation began to decrease. A slight decrease in cell number was observed for all three conditions after Hour 84, likely due to contact inhibition when reaching 100% confluency. The changes in cell morphology were characterized by the morphological features of individual nucleus at various time points, based on the previous reports showing a strong correlation between cell and nuclei shape (Figures 2D-2F) [18, 19]. Cell size estimated from nucleus size, circularity, and aspect ratio were quantified based on their distinctive morphological changes during IPSC self-renewal and differentiation. Self-renewing cells exhibited a decrease in cell size while maintaining relatively constant values for circularity and aspect ratio. This behavior is one of the characteristics of IPSCs during self-renewal in which compact cell colonies are formed and expand [20, 21]. Similarly, cells undergoing ectodermal differentiation also showed a decrease in cell size during differentiation, but they exhibited a deviation from the round cell morphology observed in the self-renewal condition. Unlike self-renewal or ectodermal differentiation, cells undergoing mesendodermal differentiation exhibited a sharp increase in cell size and aspect ratio at Hour 60 and a decrease in circularity, signifying that the cells were spreading and elongating during the differentiation period.

Cell behavior monitoring using QCM-EIS device

In comparison to imaging analysis of IPSCs cultured on tissue culture plates for various durations as described above, cells were alternatively cultured in the QCM-EIS device and subjected to the same self-renewal and differentiation conditions. Cell colony expansion was optically monitored during culture, enabled by the transparent ITO QCM crystal (Figure 3). The optical observation was conducted every 12 hours starting at Hour 24 post-device assembly, which typically showed approximately 70% confluency (Figures 3A and S2). Cell coverage on the crystal was quantified from the optical images (Figure 3B). By Hour 60 post-assembly, the cells for all conditions reached 100% confluency.

The optical observations in cell growth were compared to the mass changes that were continuously measured by QCM (Figure 4). During the initial 24 hours, the mass change exhibited two phases, the initial lag phase followed by a sharp increase, which is typical for the growth behavior of adherent cells. Differentiation initiated at Hour 24 resulted in different mass change behaviors among the three conditions. Self-renewal and ectodermal differentiation conditions exhibited similar mass change trends up to approximately Hour 48, while the mesendodermal differentiation condition showed a slower mass increase (Figure 4). After the cells reached 100% confluency at Hour 60 with peak masses for all three conditions, they exhibited dramatically different behaviors. While the cells under ectodermal differentiation condition maintained a relatively constant mass, those under self-renewal and mesendodermal differentiation

conditions exhibited a decrease in mass. Combined with the optical observation where all three conditions maintained 100% confluency after Hour 60, these results suggest that there are significant changes in cell number and morphology (e.g., size) among the three conditions. Pearson's correlation analysis showed statistically significant relationship between the cell number and the mass change for each condition (self-renewal: 0.588, $p < 0.05$; mesendodermal: 0.229, $p < 0.05$; ectodermal: 0.975, $p < 0.01$).

In addition to optical observations and mass change measurements, the impedance was determined every 12 hours during the culture by EIS using the multi-modal system. Impedance changes at various time points are presented in the form of Bode magnitude/phase plots (Figures 5A and 5B), or the Nyquist plot (Figure 5C). Representative impedance data sets for the time points that exhibited significant differences in mass among the three conditions, Hours 48, 72, and 96, are shown (complete data sets for all time points are shown in Figure S3). In the Bode magnitude plot at Hour 48, all three conditions exhibited similar impedance values at low frequencies, indicating similar cell-substrate interaction (e.g. surface coverage by the cells) (Figure 5A). However, at high frequencies, mesendodermal differentiation exhibited a different impedance behavior, suggesting changes in cell membrane [22]. Over the course of IPSC culture, all three conditions showed different impedance changes, indicating differential development of the electrochemical interfaces (e.g., cell morphology, cell coverage, cell-cell and cell-substrate interactions). The phase angle plots clearly showed a differential peak development over the duration of cell culture

for the three conditions, also indicating significant differences in cell-cell and cell-substrate interactions (Figure 5B). During the culture period, for example, the mesendodermal differentiation condition formed a shoulder, while self-renewal lost its shoulder approximately at 200 Hz. Similar to the Bode plots, the Nyquist spectra also showed clear differences in resistance and capacitance of the cells subjected to different conditions at various time points (Figure 5C). However, these impedance data do not readily deconvolute the contributions of cellular and extracellular components and their resistive and capacitive behaviors.

Equivalent circuit modeling

For a detailed analysis of impedance changes during the cell culture, an equivalent circuit model based on a cell/protein layer/electrode system was utilized [23]. The model consists of the resistance of the media (R_m), the impedance of the cellular components (resistance: R_c and capacitance: C_c), and the impedance of the extracellular components (Geltrex/electrode; resistance: R_e, capacitance: C_e, and constant phase element: CPE_e) (Figure 6A). Assuming that Z_c (combination of R_c and C_c) is the only component significantly changing during culture, fixed values for R_m and Z_e (R_e, C_e and CPE_e) were determined by direct solution measurement and impedance measurement without cells, respectively. Figure 6B shows a relatively good fitting of the equivalent circuit model on the representative experimental data for the self-renewal condition (a complete set of fitted data can be found in Figure S4). The fitted values of

R_c and C_c from impedance results of IPSCs during the course of self-renewal and differentiation are presented in Figures 6C and 6D, respectively. There was a steady increase in R_c in all conditions up to Hour 48 after which different behaviors were observed (Figure 6C). R_c was strongly correlated to the changes of cell number as determined by Pearson's correlation analysis (self-renewal: 0.717, $p < 0.01$; mesendodermal differentiation: 0.927, $p < 0.01$; ectodermal differentiation: 0.927, $p < 0.01$). Interestingly, R_c was positively correlated to the cell size in the self-renewal renewal (-0.628, $p < 0.01$) and ectodermal differentiation (-0.714, $p < 0.01$) conditions while it was negatively correlated to that in the mesendodermal differentiation condition (0.264, $p < 0.01$). C_c also exhibited different trends after reaching confluency (Figure 6D). The values for C_c increased for cells undergoing self-renewal and ectodermal differentiation after Hour 48 while C_c for the mesendodermal cells remained relatively constant. The changes in C_c strongly correlate with changes in cell size for self-renewal (-0.604, $p < 0.01$) and ectodermal differentiation (-0.385, $p < 0.01$), while there is no correlation between the C_c and the cell size/morphology for the mesendodermal differentiation condition.

Discussion

During stem cell differentiation, the cells undergo transient changes in cell shape until reaching end-phenotypes. These physico-morphological changes are important markers to determine the differentiation state of the cells [24, 25]. Optical microscopy

has been a choice of non-destructive analytical methods to monitor cellular behaviors. However, an optical analysis is semi-quantitative at best, and often subjective by observers. In this regard, a new quantitative analytical methodology enabling real-time observation of cellular behaviors in a non-destructive manner would advance our fundamental understanding in stem cell biology. Recently, Raman spectroscopy demonstrated its ability to assess the degree of stem cell differentiation by non-destructively detecting macromolecular compositional changes [26-28]. However, such chemical changes are associated with protein expression, which typically occur at the later stages of stem cell differentiation. In this study, we demonstrated that the differentiation lineage/state-dependent morphological changes of human IPSCs were significantly correlated to the changes in mass and impedance spectra that were continuously monitored throughout the culture period, providing a quantitative means to determine stem cell development.

The changes in cell mass (or surface coverage) and cell morphology are the most apparent characteristic features associated with the self-renewal and differentiation of the stem cells. During IPSC self-renewal, the cell morphology relatively maintained a round and compact shape as cell surface coverage increased by the formation and expansion of the cell colonies. In contrast, differentiation of IPSCs was marked by their transformation in cell shape as distinctive morphology was developed between differentiation toward different lineages, i.e., mesendodermal and ectodermal cells. Cells undergoing mesendodermal differentiation exhibited spreading and elongation. In

contrast, cells undergoing ectodermal differentiation showed a slightly round morphology, and exhibited stacking to form a multi-layered structure at a later stage. Such overall physical changes including cell surface coverage, morphological features of individual cells and cell-cell interactions collectively influence impedance of the cells, providing quantitative distinction among different states of cell growth/differentiation when optical visualization do not provide sufficient information.

Monitoring the mass changes provides information about general cell expansion, but it alone cannot completely depict cellular behaviors especially after reaching 100% confluency. For example, there was an increase in mass corresponding to an increase in surface coverage up 100% coverage at Hour 60. Following Hour 60, there were differences in mass change patterns, yet the surface coverage remained at 100%, due to changes in cell size. In this regard, impedance measurement can supplement the missing information, i.e., cell morphology, as impedance response depends on the electrical current pathway determined by cell surface coverage and cell morphology [22, 29-31]. As expected, impedance measurements were similar at Hour 48 before the cells reached 100% surface coverage at Hour 60, regardless of their culture conditions. Thereafter, differential and dynamic impedance changes were observed among the conditions likely due to the combinational effects from lineage-/stage-dependent cell morphology changes. Interestingly, after the cells undergoing ectodermal differentiation reached 100% confluency, up to which similar mass and impedance changes to the self-renewal condition were observed, there was a differential development in impedance spectrum.

Typically, cells subjected to ectodermal differentiation become tightly packed to form neural rosettes [32, 33]. These tightly packed cells stack on top of each other, therefore affecting the electrical pathway, leading to possible increase in impedance at lower frequencies. In contrast, cells undergoing mesendodermal differentiation exhibited a slightly different development of impedance spectrum from the initiation of differentiation as compared to the other conditions. This is likely due to the changes in cell shape before reaching 100% confluency. The changes in cell size and morphology continued with a mass decrease while maintaining 100% surface coverage. This resulted in fewer cell-cell junctions that may have led to the changes in impedance. However, it is not readily available to decouple the individual contributions of such changes in cell coverage, shape and cell-cell/cell-substrate interactions from the overall impedance of the complex system.

In this regard, equivalent circuit modeling provides a means to extract the contribution of individual components (i.e., cell, substrate, and cell culture media) from overall impedance changes. There were several studies that attempted to characterize stem cell differentiation via monitoring impedance measurements at a specific frequency [17, 34, 35]. While those studies pioneered the application of EIS in the stem cell field, they were limited to comparing impedance changes to unidentified cellular changes during stem cell differentiation in a semi-quantitative manner. The studies lacked the full realization of electrochemical analysis to link physico-morphological changes associated with various stem cell states. This study attempts to correlate the

relationship between physical properties and electrochemical responses of IPSCs in order to characterize stem cell development. An equivalent circuit model was utilized to dissect the individual contributions from resistive and capacitive reactances of the cellular components. A mechanism model for impedance responses associated with cell morphology changes during stem cell self-renewal/differentiation is proposed in Figure 7. As shown in Figure 6, R_c, resistance of the cells, increased proportionally with cell coverage before it reached 100% confluency at Hour 60. The fastest expansion of cell colonies during this period under the self-renewal condition likely led to the greatest resistance increase as compared to the differentiation conditions. At a later stage, there was a decrease in R_c in the self-renewal condition while an increase was observed in the ectodermal differentiation condition. Considering the fact that the conditions have relatively similar cell number and morphology changes, cell stacking in the ectodermal differentiation may result in a greater resistance. For mesendodermal differentiation, after 100% confluency, cell size continued to increase, leading to fewer cell-cell junctions and the highest R_c.

Changes in C_c typically indicate alterations in the cell membrane [36-38]. Clear differences in C_c among the conditions began to appear after the cells reached 100% confluency. As expected, there was a strong correlation between C_c to cell size, indicating that cellular capacitance depends on the membrane area. The C_c of self-renewing cells and cells undergoing ectodermal differentiation gradually increased up to Hour 72, strongly correlated with cell size decreases, hence increased membrane area.

Differences in C_c become apparent between the two conditions at the later stage where there is a decrease in C_c in the ectodermal differentiation condition, probably due to stacking. However, the C_c for mesendodermal cells remained relatively constant unlike the other conditions. During mesendodermal differentiation, cell size increases while they elongate (decrease in circularity and increase in aspect ratio), effectively maintaining a relatively uniform cell membrane area. This probably resulted in statistically insignificant correlation between capacitance of mesendodermal cells and their size/shape. Nevertheless, the deconvolution of electrical components demonstrated lineage and stage-specific changes, enabling the determination of stem cell behaviors during self-renewal and differentiation.

Although we have not tested this multi-modal system for different kinds of stem cells, we fully expect that any stem cell differentiation associated with mass and morphology changes can be detected by the system. It is supported by the observation that lineage-specific impedance changes at a specific frequency occur during osteogenic and adipogenic differentiation of mesenchymal stem cells [16]. In addition, the system should be able to distinguish further lineage specification that induces morphological changes, e.g., cell alignment and elongation during long-term cardiac and neural differentiation, which affect cell-substrate and cell-cell interactions, thus impedance. The EIS measurements can be continuously conducted without affecting cellular behaviors for any culture duration as long as the cells do not detach from the QCM crystal [16]. However, the system cannot detect cellular behaviors that are not

associated with morphological changes (i.e., protein secretion). In this regard, the use of the QCM-EIS system complemented by another non-destructive, label-free analytical tool that can detect chemical/macromolecular changes, like Raman spectroscopy, would further enhance the analysis of cellular behaviors.

In summary, we have demonstrated that our multi-modal system offers a powerful technology to non-destructively monitor stem cell behaviors in real time by incorporating three analytical techniques, QCM, EIS, and optical microscopy. The combination of QCM and EIS provides the capability to simultaneously quantify cellular mass change and electrical impedance of the system; QCM provides information about cell growth, while EIS offers a means to characterize cell morphology changes. Additionally, the optical visualization capability allows linking such physicoelectrochemical changes to the morphological changes of the cells. Therefore, the combination of these quantitative information and electrical circuit modeling collectively offers a means for an in-depth understanding of cellular processes during stem cell self-renewal and differentiation.

Experimental Procedures

QCM Crystal Preparation

The ITO QCM crystal (Microvacuum, Budapest, Hungary) was cleaned by ultrasonication in the sequence of acetone, isopropanol, then deionized water for 30 minutes per bath, followed by drying in a gentle flow of nitrogen gas. The crystal was

subjected to 30 seconds of oxygen plasma treatment (Electron Microscopy Sciences, Hatfield, PA) at 30 W, then sterilization with 70% ethanol for one hour, and subsequent UV-sterilization for 30 min. A commercially available basement membrane matrix, Geltrex (Life Technologies, Carlsbad, CA), was coated onto the crystal surface overnight. The Geltrex layer allows for better IPSC attachment and adhesion. Following the completion of each experiment, the crystal was subjected to an ammonia-peroxide water mixture (1:1:5 volume ratio of NH_4OH, H_2O_2, and H_2O, respectively) for 5 minutes at 75° C to effectively remove secreted proteins adhered to the crystal surface.

IPSC Culture

A well-characterized human IPSC line was utilized in this study [39-41]. Cells were seeded on to the Geltrex-coated QCM-crystal at approximately 75,000 cells/cm^2. The cells were then cultured in an incubator for 24 hours in 37°C and 5% CO_2 with mTeSR1 maintenance media (StemCell Technologies, Vancouver, Canada) supplemented by a ROCK inhibitor (Y-27632, 1:1000, Reagents Direct, Encinitas, CA) to ensure cell survival and attachment. After the 24 hours of incubation, when the cells were approximately 40% confluency, the cell-seeded ITO QCM crystal was then assembled into the device. ROCK inhibitor was removed from the culture media and cells were maintained in mTeSR1 to monitor self-renewal until reaching 70% confluency. Cells were then cultured for 72 hours under mTeSR1 maintenance media or subjected to mesendodermal or ectodermal differentiation. Optical images using a microscope were

taken every 12 hours to monitor changes in cell morphology and quantify surface coverage. For the positive controls, the same batches of IPSCs were seeded at the same seeding density onto Geltrex-coated glass coverslips in a tissue culture plate. Samples were fixed every 12 hours with 4% paraformaldehyde (Fisher Scientific, USA) and stored in PBS for subsequent immunocytochemistry.

In vitro differentiation of IPSC toward mesendodermal and ectodermal lineages

Differentiation was induced at 70% cell confluency. For mesendodermal differentiation, the cells were subjected to a medium composed of DMEM-F12, L-glutamine, ITS, non-essential amino acids, B27, and β-mercaptoethanol supplemented with the following growth factors: Day 1: 25 ng/µL Wnt3a (R&D Systems, Minneapolis, MN), 10 µg/µL Activin-A (Peprotech, Rocky Hill, NJ) ; Day 2: 25 ng/µL Wnt3a, 10 µg/mL Activin-A, 4 ng/mL bFGF (R&D Systems), Day 3: 25 ng/µL Wnt3a, 10 µg/µL Activin-A, 4 ng/µL bFGF, 50 ng/µL BMP4 (R&D Systems) [39]. Media was exchanged daily in the QCM-EIS device, as well as the positive controls.

For ectodermal differentiation, the cells were maintained in neurobasal media, supplemented with B27, N2, L-glutamine, and non-essential amino acids. The media was exchanged every 36 hours with the growth factors, 0.1 µM retinoic acid (Sigma-Aldrich, St. Louis, MO) and 2 µM dorsomorphin (Sigma-Aldrich), according to an established protocol for ectodermal differentiation [39]. The positive controls were treated on the same schedule.

Protein and gene expression of IPSC self-renewal and differentiation

Fixed cells of the positive control samples were stained for NANOG, a pluripotency marker, to confirm the maintenance of pluripotency during the culture; Goosecoid (GSC), a mesendodermal marker (R&D Systems), and Nestin, an ectodermal marker (DSHB, Iowa City, IA) to confirm for the presence of differentiated cells. 4',6-Diamidino-2-Phenylindole (DAPI, Vector Laboratories, Burlingame, CA) and Phalloidin (Life Technologies, Carlsbad, CA) staining were used to identify nuclei and actin structure, respectively.

Alternatively, the maintenance of pluripotency, or differentiation toward mesendodermal or ectodermal lineage was confirmed at the gene level by real-time PCR. Total RNA from the positive control samples was extracted using an RNeasy Micro Kit (Qiagen, Valencia, CA), and cDNA synthesis was performed using iScript cDNA Synthesis Kit (Bio-Rad, Hercules, CA) according to manufacturers' protocols. Real-time PCR was performed to determine the gene expression of pluripotency and various differentiation markers using the custom primers (Table S1). Data were analyzed by the comparative threshold cycle (C_T) method using GAPDH as an endogenous control [42].

Quantification of nucleus morphology

The shape descriptors feature from ImageJ was utilized to quantify the area, circularity, and aspect ratio of nuclei from immunofluorescent images [43]. A total of

450 cells from nine images taken from different areas of three biologically independent samples per condition were subjected to morphological characterization. Circularity is defined with $4\pi \times \frac{(Area)}{(Perimeter)^2}$ with a value of 1.0 indicating a perfect circle, and a value approaching 0 representing an elongated shape. The aspect ratio is calculated by $\frac{a}{b}$, where a and b are defined as the primary and secondary axis, respectively, of the best fitting ellipse.

Mass change and impedance measurements during cell culture

The QCM function of the system continuously monitored changes in cell mass throughout the cell culture period. EIS was set to measure impedance by applying an AC perturbation of 10 mV using a potentiostat (CH Instruments, Austin, TX) every 12 hours. The frequency sweep ranged between 10^{-1} to 10^{4} Hz with 12 measurements performed per decade. The resulting data provided impedance values (real, imaginary, and magnitude), and phase shift that corresponded to each frequency measurement.

Fitting and Simulation

EIS Analyser software was used to fit the experimental data with the proposed equivalent circuit model. The circuit model was modified from the previous study of Qiu et al. [23]. The Nelder-Mead algorithm was utilized to determine the fixed circuit values for the impedance of the extracellular components without cells. Once the fixed values

were determined, the same algorithm was used to determine the impedance of the cellular components.

Statistics

QCM and EIS measurements were repeated in triplicate with different batches of human IPSCs. The same batch of the cells were used for the positive controls with at least three samples per condition for morphological characterization. Data are presented as mean ± standard error of means (SEM). Student T-test was used to determine statistical significance of gene expression. Pearson's correlation coefficient was determined to reveal bivariate correlation between cellular characteristics (number, size and shape) and measured impedance (resistance and capacitance). Statistical significance among the experimental conditions (i.e., self-renewal to mesendodermal differentiation, self-renewal to ectodermal differentiation, and mesendodermal differentiation to ectodermal differentiation) for cell number, morphological features, the resistive and capacitive values from EIS measurements/model fitting was determined by ANOVA with Tukey's post-hog test. It was considered statistically significant when a '*p*' value was less than 0.05.

Acknowledgments

This study was supported by the UCR Initial Complement Fund and the UCR Stem Cell Core Facility, funded by CIRM.

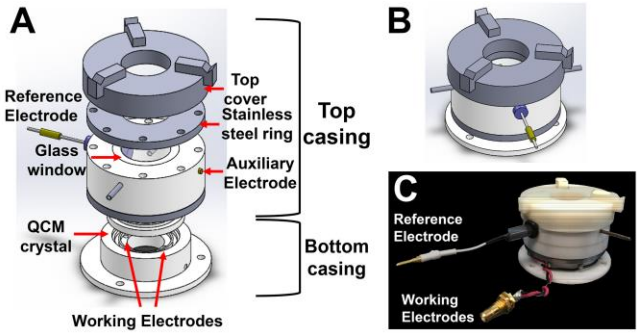

Figure C.1. A schematic of the multi-modal QCM-EIS device. (A) An assembly view of the device labeled for individual components. (B) An assembled view of the device. (C) A photograph of the prototype QCM-EIS device.

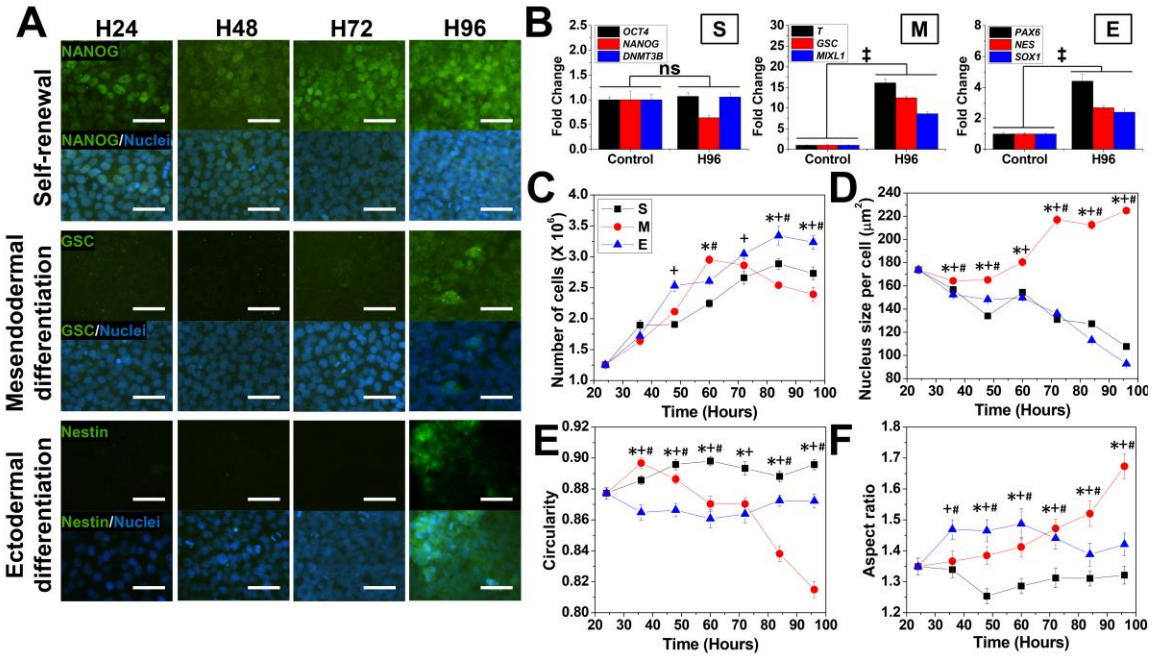

Figure C.2. Characterization of human induced pluripotent stem cells under self-renewal/differentiation conditions and immunofluorescence analyses of cell number and morphology. (A) Representative immunofluorescence images showing protein expression of pluripotency marker, NANOG, mesendodermal marker, GSC, and ectodermal marker, Nestin for self-renewal, mesendodermal and ectodermal differentiation conditions, respectively over 96 hours. (blue: nucleus, green: protein of interest, scale bar: 50 μm) (See also Figure S1, images reused in). (B) RT-PCR analysis of pluripotency (*OCT4, NANOG, DNMT3B*) and differentiation (mesendodermal: *T, GSC, MIXL1*; ectodermal: *PAX6, NES, SOX1*) markers after 96 hours of culture (S: self-renewal, M: mesendodermal differentiation, E: ectodermal differentiation. Data are represented as mean ± SEM of six independent samples. ‡ and ns denote $p < 0.01$ and not significant, respectively). Comparison of (C) cell number change and cell morphology

characterization ((D) nuclei coverage area, (E) circularity, and (F) aspect ratio) via nuclei analysis during IPSC self-renewal and differentiation from immunofluorescence images. (Data are represented as mean ± SEM (n = 450 cells from nine different areas of three biologically independent samples). *, + and # denote $p < 0.05$ between S and M, S and E, and M and E, respectively).

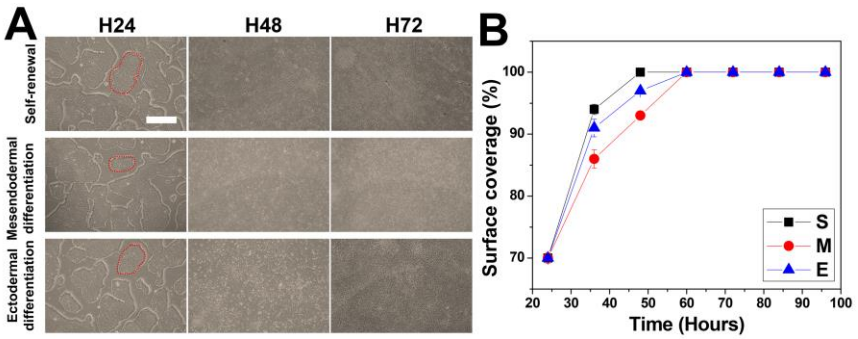

Figure C.3. Optical monitoring of IPSCs during self-renewal or differentiation in the QCM-EIS device. (A) Representative optical images taken every 24 hours during the course of cell culture up to 100% confluency (See also Figure S2, images reused in). Red dotted outlines represent a single cell colony within the culture (Scale bar, 1 mm). (B) Cell surface coverage during IPSC culture quantified from optical images. (S: self-renewal, M: mesendodermal differentiation, E: ectodermal differentiation. Data are represented by mean ± SEM (n = 9) of three independent experiments. *, + and # denote $p < 0.05$ between S and M, S and E, and M and E, respectively).

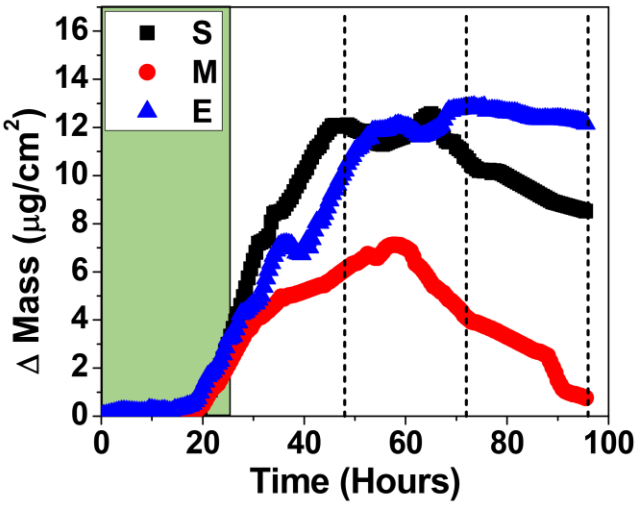

Figure C.4. Mass changes during IPSC self-renewal or differentiation by QCM. Representative data sets of cell mass change measured by QCM during IPSC culture. The shaded region indicates the initial self-renewal phase for all three conditions. Differentiation was induced at Hour 24 for either mesendodermal or ectodermal lineage. The broken lines indicate time points used for EIS analysis at Hours 48, 72, 96 (S: self-renewal, M: mesendodermal differentiation, E: ectodermal differentiation).

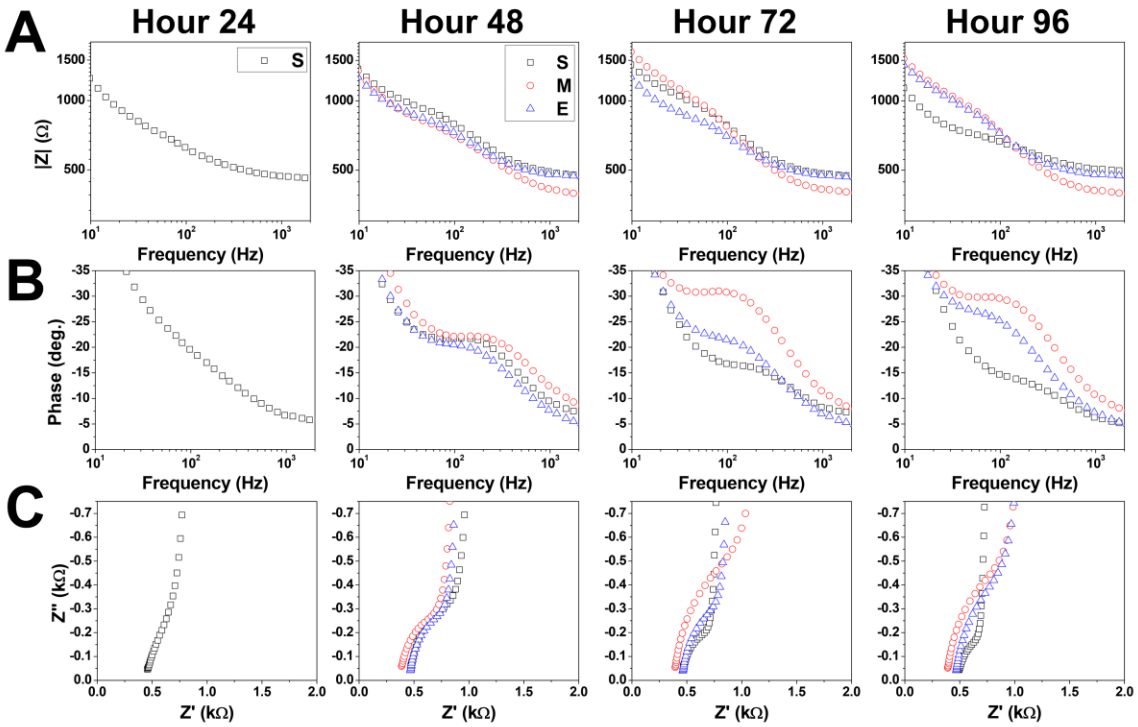

Figure C.5. Impedance measurements of IPSC self-renewal or differentiation by EIS. Representative (A) Bode magnitude, (B) Bode phase, and (C) Nyquist plots of EIS measurements at Hours 48, 72, and 96 for IPSCs subjected to self-renewal or differentiation (S: self-renewal, M: mesendodermal differentiation, E: ectodermal differentiation) (See also Figure S3).

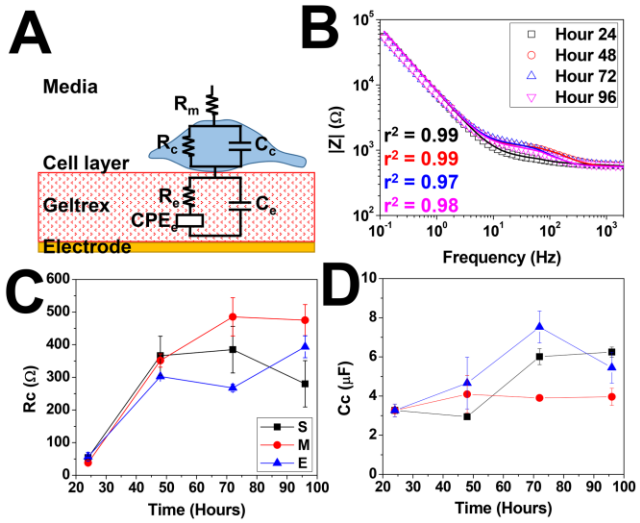

Figure C.6. Equivalent circuit modeling of IPSCs. (A) A schematic of an equivalent circuit model for Geltrex/electrode-IPSC-culture media interfaces consisted of resistance, capacitance, and CPE of the extracellular components (R_e, C_e, and CPE), resistance and capacitance of cellular components (R_c and C_c), and resistance of cell culture media solution (R_m). (B) Representative Bode magnitude curves fitted with the equivalent circuit model for self-renewal. (Scattered plot – experimental data, line plot – fitted data). (C) R_c and (D) C_c values derived from the equivalent circuit model over the course of cell culture period. (S: self-renewal, M: mesendodermal differentiation, E: ectodermal differentiation. Data are represented by mean ± SEM of three independent experiments. *, + and # denote $p < 0.05$ between S and M, S and E, and M and E, respectively) (See also Figure S4).

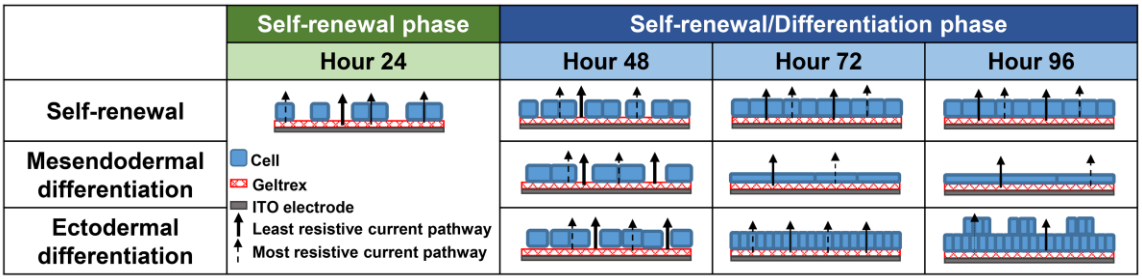

Figure C.7. Proposed mechanisms for cellular and electrochemical changes during stem cell self-renewal and differentiation.

References

1. Amabile, G. and A. Meissner, *Induced pluripotent stem cells: current progress and potential for regenerative medicine.* Trends Mol Med, 2009. **15**(2): p. 59-68.

2. Cyranoski, D. *Japanese woman is first recipient of next-generation stem cells*. 2014 September 12, 2014]; Available from: http://www.nature.com/news/japanese-woman-is-first-recipient-of-next-generation-stem-cells-1.15915.

3. Burkhardt, M.F., et al., *A cellular model for sporadic ALS using patient-derived induced pluripotent stem cells.* Molecular and Cellular Neuroscience, 2013. **56**: p. 355-364.

4. Chen, H., et al., *Modeling ALS with iPSCs reveals that mutant SOD1 misregulates neurofilament balance in motor neurons.* Cell stem cell, 2014. **14**(6): p. 796-809.

5. Egawa, N., et al., *Drug screening for ALS using patient-specific induced pluripotent stem cells.* Science translational medicine, 2012. **4**(145): p. 145ra104-145ra104.

6. Kim, C., *Disease modeling and cell based therapy with iPSC: future therapeutic option with fast and safe application.* Blood Res, 2014. **49**(1): p. 7-14.

7. Ebert, A.D., P. Liang, and J.C. Wu, *Induced pluripotent stem cells as a disease modeling and drug screening platform.* J Cardiovasc Pharmacol, 2012. **60**(4): p. 408-16.

8. Oldershaw, R.A., et al., *Directed differentiation of human embryonic stem cells toward chondrocytes.* Nat Biotechnol, 2010. **28**(11): p. 1187-94.

9. Hu, B.Y., et al., *Neural differentiation of human induced pluripotent stem cells follows developmental principles but with variable potency.* Proc Natl Acad Sci U S A, 2010. **107**(9): p. 4335-40.

10. Wang, S., et al., *Differentiation of human induced pluripotent stem cells to mature functional Purkinje neurons.* Sci Rep, 2015. **5**: p. 9232.

11. Chen, C., et al., *Role of astroglia in Down's syndrome revealed by patient-derived human-induced pluripotent stem cells.* Nat Commun, 2014. **5**: p. 4430.

12. Venkatanarayanan, A., T.E. Keyes, and R.J. Forster, *Label-free impedance detection of cancer cells.* Anal Chem, 2013. **85**(4): p. 2216-22.

13. Qiao, G., et al., *Bioimpedance analysis for the characterization of breast cancer cells in suspension.* IEEE Transactions on Biomedical Engineering, 2012. **59**(8): p. 2321-2329.

14. Morgan, H., et al., *Single cell dielectric spectroscopy.* Journal of Physics D: Applied Physics, 2007. **40**(1): p. 61-70.

15. Randviir, E.P. and C.E. Banks, *Electrochemical impedance spectroscopy: an overview of bioanalytical applications.* Analytical Methods, 2013. **5**(5): p. 1098-1115.

16. Bagnaninchi, P.O. and N. Drummond, *Real-time label-free monitoring of adipose-derived stem cell differentiation with electric cell-substrate impedance sensing.* Proceedings of the National Academy of Sciences, 2011. **108**(16): p. 6462-6467.

17. Angstmann, M., et al., *Monitoring human mesenchymal stromal cell differentiation by electrochemical impedance sensing.* Cytotherapy, 2011. **13**(9): p. 1074-1089.

18. Versaevel, M., T. Grevesse, and S. Gabriele, *Spatial coordination between cell and nuclear shape within micropatterned endothelial cells.* Nat Commun, 2012. **3**: p. 671.

19. Vishavkarma, R., et al., *Role of actin filaments in correlating nuclear shape and cell spreading.* PloS one, 2014. **9**(9): p. e107895.

20. Meissner, A., M. Wernig, and R. Jaenisch, *Direct reprogramming of genetically unmodified fibroblasts into pluripotent stem cells.* Nat Biotechnol, 2007. **25**(10): p. 1177-1181.

21. Yu, J., et al., *Induced pluripotent stem cell lines derived from human somatic cells.* Science, 2007. **318**(5858): p. 1917-1920.

22. Giaever, I. and C.R. Keese, *A morphological biosensor for mammalian cells.* Nature, 1993. **366**(6455): p. 591.

23. Qiu, Y., R. Liao, and X. Zhang, *Real-time monitoring primary cardiomyocyte adhesion based on electrochemical impedance spectroscopy and electrical cell-substrate impedance sensing.* Anal Chem, 2008. **80**(4): p. 990-996.

24. Neuhuber, B., et al., *Reevaluation of in vitro differentiation protocols for bone marrow stromal cells: Disruption of actin cytoskeleton induces rapid*

morphological changes and mimics neuronal phenotype. Journal of Neuroscience Research, 2004. **77**(2): p. 192-204.

25. Sullivan, G.J., et al., *Generation of functional human hepatic endoderm from human induced pluripotent stem cells.* Hepatology, 2010. **51**(1): p. 329-335.

26. Schulze, H.G., et al., *Assessing Differentiation Status of Human Embryonic Stem Cells Noninvasively Using Raman Microspectroscopy.* Anal Chem, 2010. **82**(12): p. 5020-5027.

27. Chan, J.W., et al., *Label-Free Separation of Human Embryonic Stem Cells and Their Cardiac Derivatives Using Raman Spectroscopy.* Anal Chem, 2009. **81**(4): p. 1324-1331.

28. Konorov, S.O., et al., *Process Analytical Utility of Raman Microspectroscopy in the Directed Differentiation of Human Pancreatic Insulin-Positive Cells.* Anal Chem, 2015. **87**(21): p. 10762-10769.

29. Keese, C.R. and I. Giaever, *A biosensor that monitors cell morphology with electrical fields.* IEEE Engineering in Medicine and Biology Magazine, 1994. **13**(3): p. 402-408.

30. Giaever, I. and C.R. Keese, *Use of electric fields to monitor the dynamical aspect of cell behavior in tissue culture.* IEEE Transactions on Biomedical Engineering, 1986(2): p. 242-247.

31. Wegener, J., C.R. Keese, and I. Giaever, *Electric cell–substrate impedance sensing (ECIS) as a noninvasive means to monitor the kinetics of cell spreading to artificial surfaces.* Experimental cell research, 2000. **259**(1): p. 158-166.

32. Warren, L., et al., *Highly Efficient Reprogramming to Pluripotency and Directed Differentiation of Human Cells with Synthetic Modified mRNA.* Cell stem cell, 2010. **7**(5): p. 618-630.

33. Elkabetz, Y., et al., *Human ES cell-derived neural rosettes reveal a functionally distinct early neural stem cell stage.* Genes & development, 2008. **22**(2): p. 152-165.

34. Hildebrandt, C., et al., *Detection of the osteogenic differentiation of mesenchymal stem cells in 2D and 3D cultures by electrochemical impedance spectroscopy.* Journal of biotechnology, 2010. **148**(1): p. 83-90.

35. Park, H.E., et al., *Real-time monitoring of neural differentiation of human mesenchymal stem cells by electric cell-substrate impedance sensing.* BioMed Research International, 2011. **2011**.

36. de Roos, A.D., E.J. van Zoelen, and A.P. Theuvenet, *Determination of gap junctional intercellular communication by capacitance measurements.* Pflügers Archiv, 1996. **431**(4): p. 556-563.

37. Benson, K., S. Cramer, and H.-J. Galla, *Impedance-based cell monitoring: barrier properties and beyond.* Fluids and Barriers of the CNS, 2013. **10**: p. 5-5.

38. Jo, D.H., et al., *Real-time estimation of paracellular permeability of cerebral endothelial cells by capacitance sensor array.* Sci Rep, 2015. **5**.

39. Maldonado, M., et al., *Enhanced Lineage-Specific Differentiation Efficiency of Human Induced Pluripotent Stem Cells by Engineering Colony Dimensionality Using Electrospun Scaffolds.* Advanced Healthcare Materials, 2016. **5**(12): p. 1408-1412.

40. Maldonado, M., et al., *The effects of electrospun substrate-mediated cell colony morphology on the self-renewal of human induced pluripotent stem cells.* Biomaterials, 2015. **50**: p. 10-19.

41. Maldonado, M., et al., *ROCK inhibitor primes human induced pluripotent stem cells to selectively differentiate towards mesendodermal lineage via epithelial-mesenchymal transition-like modulation.* Stem Cell Research, 2016. **17**(2): p. 222-227.

42. Livak, K.J. and T.D. Schmittgen, *Analysis of Relative Gene Expression Data Using Real-Time Quantitative PCR and the 2−ΔΔCT Method.* Methods, 2001. **25**(4): p. 402-408.

43. Rocca, A., et al., *Barium titanate nanoparticles and hypergravity stimulation improve differentiation of mesenchymal stem cells into osteoblasts.* Int J Nanomedicine, 2015. **10**: p. 433-45.